

**FABRICATION AND DYNAMIC TUNING OF PERIODIC STRUCTURES FROM
HOLOGRAPHIC LITHOGRAPHY**

Jie Li

A DISSERTATION

in

Material Science and Engineering

Presented to the Faculties of the University of Pennsylvania

in

Partial Fulfillment of the Requirements for the

Degree of Doctor of Philosophy

2013

Supervisor of Dissertation

Shu Yang, Professor of Material Science and Engineering

Graduate Group Chairperson

Shu Yang, Professor of Material Science and Engineering

Dissertation Committee

Russell J. Composto, Professor of Material Science and Engineering

Cherie R. Kagan, Professor of Material Science and Engineering

Daeyeon Lee, Associate Professor of Chemical and Biomolecular Engineering

ACKNOWLEDGEMENT

In the past five years, I have been fortunate enough to be associated with many people without whose valuable help and input this thesis would not have been possible. It is my great pleasure to humbly express my gratitude towards them in my acknowledgement.

Foremost, I sincerely thank my advisor, Prof. Shu Yang, for all her inspiration, guidance, support, encouragement and patience throughout the entire course of my research. I am very grateful to have been introduced to the fascinating research on holographic lithography, which is totally fresh and attractive to me. She helped me to grow to be a scientist in many ways, from critical thinking, experimental design to presentation and writing skills. I really appreciate that she devotes so much time, often during midnight, to exchange thoughts and writings with me. She was always patient and supportive, even at my worst times with poor results and depression. Her encouragement eventually helped me to build confidence in research, which led me here step by step.

I would like to thank my thesis committee members, Prof. Russell J. Composto, Prof. Cherie R. Kagan and Prof. Daeyeon Lee, for their time, attention, effort and feedback to me for the research proposal and all the annual progress reports. Their insightful comments and suggestions have helped me to make this thesis more thorough and their appreciation has encouraged me a lot.

I am grateful to all my collaborators from top institutes all over the world. I would thank Prof. Katia Bertoldi, Dr Jongmin Shim and Johannes T. B. Overvelde from Harvard University for the collaboration and simulation on 2D shape memory polymer study. I

acknowledge Prof. In-suk Choi and Dr. Yigil Cho (now at Penn) from Korea Institute of Science and Technology for the discussion on 2D SU-8 nanowaves mechanism and simulation support. I am also grateful to Prof. George Fytas and Dirk Schneider from Max Planck Institute with the collaboration on 1D hypersonic phononic crystal, and I am looking forward to more exciting results coming out.

Within University of Pennsylvania, I also need to acknowledge many people for all kinds of help. I thank Prof. Christopher Murray, Prof. Karen Winey and Prof. Jason Burdick for granting me access to FTIR, hot-press and IR laser, respectively. I am grateful to Penn Regional Nanotechnology Facility (PRNF) for access to SEM, FIB and EDX, especially to Dr. Douglas Yates, Dr. Lolita Rotkina and Dr. Jamie Ford with the training and support on these instruments. I acknowledge Wolf Nanofabrication Facility for access to various film deposition and etching tools, especially to Kyle Keenan for all his kind help with my experiments. I thank Nano- Bio Interface Center (NBIC) for access to AFM and Raman spectroscopy, especially to Dr. Matthew Brukman for all the training. I am also grateful to Steve Szewczyk, since he trained me on so many instruments in Materials department, such as DSC, UV-Vis, thermal evaporator, vacuum hot-press and tube furnace.

Besides, I would express my gratitude to the LRSM staff. Felice Mecara kindly helped me a lot with the sample photo shootings and the cover image design. I also thank Pat Overend, Irene Clements, Vicky Lee Truei, Fred Helmig, Enrique Vargas and Raymond Hsiao, for being so nice to me and offering me help whenever necessary.

I have been lucky to have met so many good colleagues and friends at Penn, and I would like to express my appreciation to all of them. I would thank my seniors from

MSE department, Dr. Yongan Xu, Dr. Xuelian Zhu and Dr. Wenqing Wang, for guiding me to the research and helping me through the qualify exam. I also appreciate the intriguing discussions and endless help on course work with my Ph.D classmates, Wenbin Li, Xi Chen and Soon-Ju Oh. In Yang's group, I benefited a lot by learning from my post-doc colleagues and visiting scientists, Dr. Guanquan Liang, Dr. Rong Dong, Dr. Lebo Xu, Dr. Yudi Rahmawan, Dr. Su-yeon Lee, Dr. Mohamed Amine Gharbi, Dr. Dengteng Ge, Prof. Liping Zhu, Prof. Lili Yang, Prof. Youfa Zhang and Prof. Hyunsik Yoon. I also thank my fellows, Dr. Apiradee Honglawan, Chi-Mon Chen, Yu Xia, Gaoxiang Wu, Elaine Lee, for working together and exchanging ideas. I would specially thank Yongwei Zheng, Justin Deng and Jerry Qi, who work with me on thermal and light responsive SMP periodic structures. Their trust and help is truly valuable for me. With all their input, my PhD journey was absolutely exciting and enjoyable.

I would express my heartfelt gratitude towards my husband, Xiang Yang, for his endless love and support. I truly appreciate that he sacrificed beach and sunshine from south California and transferred to Penn, to make my PhD life not lonely any more. I also benefited a lot during dinner chat with him on all kinds of scientific issues, and gained lots of motivation watching him diving so deeply in the research world. Besides, he was the one who stand by me all the time, listening to my complaining and giving me all the comfort and encouragement at my lowest moments.

Finally, I am deeply grateful to all my family members, especially my parents and grandparents. I could not have gone so far in the scientific road without your love and trust. I thank my mother, Qin Wang, to whom I dedicated my thesis, for developing my self-confidence and curiosity since childhood, encouraging me to fearlessly pursue

scientific career path, and for all her sacrifice to me and to the family.

ABSTRACT

FABRICATION AND DYNAMIC TUNING OF PERIODIC STRUCTURES FROM HOLOGRAPHIC LITHOGRAPHY

Jie Li

Shu Yang

In this dissertation, I fabricated one-dimensional (1D), two-dimensional (2D) and three-dimensional (3D) periodic structures through holographic lithography (HL) and backfilling conversion with different materials. Along the line, I investigated their intrinsic structure-property relationship, harness and utilize the mechanical instability, and explored novel applications as tunable periodic structures.

In order to mimic butterfly wings which show both structural color and superhydrophobicity, 3D diamond photonic crystals with controllable nano-roughness (≤ 120 nm) were fabricated from epoxy-functionalized cyclohexyl polyhedral oligomeric silsesquioxanes (epoxy-POSS). The nano-roughness was generated due to microphase separation of the polymer chain segments in nonsolvents during rinsing, which could be tuned by crosslinking density of the polymer and choice of solvents. Such structure offers opportunities to realize superhydrophobicity, enhanced dye adsorption in addition to the photon management in the 3D photonic crystal.

Most of current studies on tunable periodic structures show limited tunable optical property ranges, which is attractive to be expanded. 2D shape memory polymer (SMP) membranes consisting of a hexagonal array of micron-sized holes were fabricated by

converting from epoxy-POSS template. Reversible color switching from transparency to colorful state was achieved through thermal-mechanical deformation, utilizing shape memory effect and mechanical instability induced pattern transformation. Continuum mechanical analyses corroborated well with experimental observations. Potential applications as displays were demonstrated via two different approaches.

It is challenging to directly fabricate high aspect-ratio (AR) 1D nano-scale structures, due to depth-of-focus (DOF) limitation, pattern collapse from capillary force and distortion during solvent swelling. With HL and supercritical drying, high AR 1D nano-scale structures were fabricated with epoxy-POSS and SU-8, which avoid DOF limitation and pattern collapse. Due to enhanced thermal and mechanical stability of epoxy-POSS, 1D nanogratings (AR up to 10) with controllable periodicity, filling fraction and surface roughness, were achieved, which could be directly converted to silica-like through calcination. By exploiting swelling-induced buckling of 1D SU-8 nanowalls with nanofibers formed in-between, long-range ordered 2D nanowaves with weaker reflecting color were achieved, where degree of lateral undulation could be controlled by tuning AR and exposure dosage. Using double-exposure through photomasks, patterns with both nanowaves and nanowalls for optical display were created.

TABLE OF CONTENTS

Acknowledgment.....	ii
Abstract.....	vi
List of Tables.....	xii
List of Figures.....	xiii
CHAPTER 1: Fabrication and dynamic tuning of periodic structures from holographic lithography	1
1.1 Introduction.....	1
1.2 Approaches to fabricate periodic structures	3
1.2.1 Photolithography.....	3
1.2.2 Scanning beam lithography.....	5
1.2.3 Colloidal assembly.....	5
1.2.4 Block copolymer self-assembly	6
1.2.5 Holographic lithography	7
1.3 Material aspects of periodic structures.....	9
1.3.1 Photoresists	9
1.3.1.1 SU-8.....	9
1.3.1.2 POSS.....	10
1.3.2 High refractive index materials.....	11
1.3.3 Functional organic materials.....	13
1.4 Tunable periodic structures	15
1.4.1 Thermal responsive periodic structures.....	15
1.4.2 Chemical responsive periodic structures.....	16
1.4.3 Mechanical responsive periodic structures.....	16
1.4.4 Light responsive periodic structures	17

1.4.5 Electrically responsive periodic structures	18
1.4.6 Magnetic responsive periodic structures	19
1.5 Current issues and thesis outline	20
1.6 Reference	22
CHAPTER 2: Exploiting nano-roughness on holographically patterned three-dimensional photonic crystals.....	30
2.1 Introduction	30
2.2 Experimental methods	32
2.2.1 Holographic lithography	32
2.2.2 Surface hydrophobization	32
2.2.3 Dye adsorption	33
2.2.3.1 Hydrophilic surfaces	33
2.2.3.2 Hydrophobic surfaces	33
2.2.4 Characterization	33
2.3 Results and discussion.....	33
2.3.1 3D microfabrication and formation of nano-roughness on 3D structures	33
2.3.2 Mechanism of nano-roughness formation	37
2.3.3 Photonic band gap properties	41
2.3.4 Tunable wetting behaviors	42
2.3.5 Enhanced small molecule adsorption.....	44
2.4 Conclusions	46
2.5 Reference	47
CHAPTER 3: Switching periodic membranes via pattern transformation and shape memory effect	51
3.1 Introduction	51
3.2 Experimental Methods	53
3.2.1 Fabrication of the hexagonal pillar array	53

3.2.2 Replica molding SMP periodic membrane.....	54
3.2.3 Hot pressing of SMP membranes	55
3.2.4 Fabrication of SMP membrane with embedded “Penn” letter.....	55
3.2.5 Calculation/modelling	56
3.3 Results and discussion.....	56
3.3.1 Color/ Transparency switching in SMP periodic membrane.....	57
3.3.2 Finite element analysis.....	61
3.3.3 Color displays with SMP periodic membranes	65
3.4 Conclusions	67
3.5 Reference	68
CHAPTER 4: Fabrication of high-aspect-ratio one-dimensional organic/inorganic hybrid nanogratings via holographic lithography	71
4.1 Introcuton.....	71
4.2 Experimental methods.....	73
4.2.1 Fabricaton	73
4.2.2 Characterization	74
4.3 Results and discussion.....	74
4.4 Conclusions	81
4.5 Reference	82
CHAPTER 5: Transforming one-dimensional nanowalls to long-range ordered two-dimensional nanowaves – exploiting buckling instability and nanofibers effect in holographic lithography	85
5.1 Introduction.....	85
5.2 Experimental methods.....	85
5.2.1 Holographic lithography	86
5.2.2 Fiber removal and re-swelling	87
5.2.3 Double exposure	87

5.2.4 Characterization	88
5.2.5 Finite-element analysis	88
5.3 Results and discussion.....	88
5.4 Conclusions	100
5.5 Reference	101
CHAPTER 6: Summary and outlook	105
6.1 Summary	105
6.2 Outlook.....	109
6.3 Reference	110

LIST OF TABLES

Table 1.1 Different approaches for fabrication of periodic structures.....	3
Table 1.2 Important material refractive indexes and their conversion methods.....	12
Table 2.1 Summary of the heights of surface nano-features measured from line profile analysis in Figure 2.2.	36
Table 2.2 Summary of observed surface roughness on 3D diamond structures from different solvents used in development, rinsing and critical point drying process.	37
Table 2.3 Hansen solubility parameters of epoxy-POSS and different organic solvents.	39
Table 3.1 Material constants for SMP used in the mechanical models.	62
Table 4.1 Theoretical periodicities of two-beam interference lithography from variable incident beam half angles.....	76
Table 4.2 EDX element analysis data of the original and calcinated samples.	81

LIST OF FIGURES

Figure 1.1 Schematic illustration of the 1D, 2D and 3D periodic structures fabricated by holographic lithography in negative-tone photoresists. 8

Figure 1.2 Chemical structures of SU-8 and epoxy-functionalized polyhedral oligomeric silsesquioxane (epoxy-POSS). 10

Figure 1.3 Examples of periodic structures directly fabricated with HL in epoxy-POSS and the converted SMP structures. (a) 1D nanogratings, (b) 2D hexagonal pillar array, (c) 3D diamond-like structure, (d) 3D diamond structure, (e) 2D SMP membrane converted from (b), and (f) 3D SMP inversed diamond-like structure converted from (d). Scale bar: 2 μm 14

Figure 2.1 Diamond photonic crystals of variable degrees of nano-roughness from epoxy-POSS. (a) Top-view SEM image. (b-c) Schematics of photoresist chains swollen in a good solvent (b) or collapsed in a nonsolvent (c) within a mesh. (d) Chemical structure of epoxy-POSS. (e-f) Cross-sectional SEM images of the diamond structures developed in PGMEA and rinsed in (e) IA and (f) ethanol, respectively, followed by critical point drying in the same solvent. (g-h) Cross-sectional SEM images of the diamond structures developed in GBL and rinsed in (g) IA and (h) ethanol, respectively, followed by critical point drying in the same solvent. (i) Cross-sectional SEM image of the diamond structure developed in GBL, rinsed in DI water and dried in air. Scale bar: 2 μm 35

Figure 2.2 AFM characterization of the surface topography of diamond structures developed in GBL, followed by rinsing in ethanol and CPD. a). Height profile of the rough sample, same as sample in Figure 2.1 h. b). Line profile analysis of Figure a. The height and width of the surface features are measured from the three line profiles. Note that there was 300 nm offset in Y scale between each lines for the purpose of illustration. The large valleys in the profiles (> 200 nm) were attributed to 3D microstructure. 36

Figure 2.3 Surface roughness on epoxy-POSS diamond structures as a function of chain crosslinking density. The samples were developed in GBL and rinsed in ethanol, followed by critical point drying. (a-b) Schematics of the collapsed polymer chains in a poor solvent at a low (a) and high (b) crosslinked density. (c) Photoacid generator concentration [PAG] = 0.3 wt%, exposure time of 0.6s. (d-f) [PAG] = 1.0 wt%, exposure time: (d) 0.25s, (e) 0.30, and (f) 0.35s. 41

Figure 2.4 (a) Structural color observed from epoxy-POSS diamond structure (1 cm diameter) with nano-roughness. The film was developed in GBL, rinsed and critical point dried in ethanol. (b) FTIR reflection and transmission spectra of diamond structures with smooth (developed in PGMEA, rinsed and dried in IA) and rough (developed in GBL,

rinsed and dried in ethanol) surfaces. The shaded area represents the calculated PBGs.. 42

Figure 2.5 Wetting behaviors of fluorosilane treated epoxy-POSS diamond structures. (a-c) Samples with smooth surfaces. (e-g) Samples with rough surfaces. Inset: static water contact angles. (d) Photo of a water droplet on sample (c). (h) Photo of a water droplet on sample (e). The smooth samples (a-d) were developed in PGMEA, rinsed in IA for 1 h, and critical-point dried. The rough samples (e-h) were developed in GBL, rinsed in ethanol overnight, and critical-point dried. All samples were then treated with oxygen plasma for 15 min, followed by fluorosilane vapor deposition. 43

Figure 2.6 Comparison of rhodamine B adsorption on smooth and rough diamond structures. The smooth samples were developed in PGMEA, rinsed in IA for 1 h, and critical-point dried. The rough samples were developed in GBL, rinsed in ethanol overnight, and critical-point dried. (a) Absorbance of dye released from the diamond structures in water at 554 nm over time. The samples were treated with oxygen plasma for 15 min, followed by soaking in rhodamine B aqueous solutions for 30 min. Inset: optical images of dye adsorbed films from rhodamine B aqueous solution. (b) Optical images of water droplets sitting on fluorosilane treated diamond structures followed by adsorption of rhodamine B ethanol solution for 5 min. Left, smooth surface. Right, rough surface. 45

Figure 3.1 Schematic illustration of fabrication and deformation/recovery of a 2D SMP membrane. (a) Fabrication of 2D pillar array by holographic lithography. (b) Fabrication of SMP membrane with periodic holes by replica molding, followed by etching in HF aqueous solution. (c) Hot-pressing of SMP membrane in the vertical direction above T_g . The temporary shape could be fixed by cooling down to room temperature under the load. The original shape could be recovered upon reheating above T_g 54

Figure 3.2 Pattern transformation and recovery in a 2D SMP membrane. (a-e) Optical images of the (a) original, (b-c) partially deformed, $\varepsilon \sim 13 \pm 2\%$ (b) and $\varepsilon \sim 20 \pm 2\%$ (c), (d) completely deformed, $\varepsilon \sim 30 \pm 2\%$, and (e) recovered SMP membranes. (f-j) Corresponding SEM images of the SMP membranes shown in (a-e). (k-o) Higher magnification SEM images of (f-j). 59

Figure 3.3 Display of “Penn” logos underneath 2D SMP membranes. a. Schematic illustration of transparency comparison between the deformed and the original SMP membranes. b. Optical images of the deformed and original SMP membranes on top of the “Penn” logo. The “Penn” underneath the original membrane is hardly legible but clearly visible in the deformed sample. c. UV-Vis spectra of different 2D SMP membranes (A-D) using bulk SMP film as reference. A. Original. B. Deformed at $\varepsilon \sim 13 \pm 2\%$. C. Deformed at $\varepsilon \sim 30 \pm 2\%$. D. Recovered one. 61

Figure 3.4 Numerical results for the SMP thermo-mechanical cycle. Snapshots of the

hexagonal lattice during Step 1, hot-pressing at different strain levels (a-d), and at the end of Steps 2, cooling down (e), 3, un-loading (f) and 4, reheating (g). The color gives indications of the maximum principal strain distribution. 62

Figure 3.5 Display of “PENN” embedded in a 2D SMP membrane. (a) Schematic illustration of the fabrication of template. (b-d) SEM images of the photoresist template before replication to the SMP membrane. (b) A low magnification SEM image of the “P” character in the template. (c) SEM image of the structure outside “P” character, yellow square, showing tall pillars. (d) SEM image of the structure inside the “P” character, red circle, showing nearly flat film with shallow voids. e-g. Optical images of the original (e), deformed (f) and recovered (g) SMP films. 66

Figure 3.6 Indentation display on the SMP membrane. Schematic illustrations of (a) indentation of a stamp with a letter “P” into a heated SMP membrane, (b) the display of letter “P” in the SMP membrane in the deformed region and (c) structural recovery upon reheating. (d-e). Corresponding optical images of the indented “Penn” in the colored SMP membrane (d) and its erase after reheating the SMP membrane to 90 °C (e). 67

Figure 4.1 Holographic lithography (HL) process to fabricate 1D high AR structures. (a) Schematics of HL fabrication process. (b) Chemical Structure of epoxy polyhedral oligomeric silsesquoxane (epoxy-POSS). (c) Two-beam interference intensity profile. 1D periodic structure is formed in the regions, where the light intensity is higher than the threshold. (d) Top-view and cross-sectional view (inset) SEM images of the 1D grating with 300 nm line width, 600 nm pitch and AR= 10. 74

Figure 4.2 Top-view SEM images of 1D structures fabricated with different incident beam half angles, $\theta = 7.5^\circ$ and 26° , respectively. Inset: schematics showing the beam position. (a) Line width 500 nm, pitch 2 μm , height 2 μm , and AR =4. (b) Line width 250 nm, pitch 600 nm, height 2 μm , and AR=8. 76

Figure 4.3 Top-view SEM images of 1D structures with exposure duration of 3 s, 4 s and 5 s, respectively. (a) Line width 200 nm, AR=10. (b) Line width 230 nm, AR= 8.7. (c) Line width 260 nm, AR= 7.7. 78

Figure 4.4 Side-view SEM images of the 1D structures fabricated by HL, showing smooth and rough surfaces. (a) Very rough surface fabricated with 3 s exposure duration. (b) Relatively smooth surface fabricated with 6 s exposure duration. Other Fabrication parameters were kept the same. 79

Figure 4.5 Energy-dispersive X-ray spectra and top-view SEM images (inset) for high AR 1D structures before and after calcination. (a) Original POSS structure, showing C, O and Si peaks. (2) After the calcinations at 500 °C in O₂ for 2 h, the carbon peak

disappeared. Line width 200 nm, pitch 600 nm, height 2 μm , and AR=10. Scale bar: 1 μm 81

Figure 5.1 Fabrication of 1D nanowalls and 2D nanowaves via two-beam holographic lithography. (a) Schematics of the holographic lithography process. (b-c) Top-view SEM images and schematics of (b) 1D nanowalls (width 300 nm, pitch 600 nm, AR ~2) and (c) 2D nanowaves (width 300 nm, pitch 600 nm, AR ~6). (d) Higher magnification SEM image of (c) with indication of the amplitude and wavelength of the nanowaves. Amplitude (yellow arrow) is indicated as the distance between center of the original wall to that of the maximum buckled position. Wavelength (green arrow) is the longitudinal periodicity of the nanowaves 87

Figure 5.2 (a) Chemical structure of the negative-tone photoresist, SU-8. (b) Top-view SEM image of large area of long-range ordered nanowaves with a few anti-phase boundaries. (c) Cross-sectional SEM image of the nanowaves showing high aspect ratio (AR = 6).. 90

Figure 5.3 Optical image of the developed film immersed in the rinsing solvent, IPA.
..... 91

Figure 5.4 Effect of exposure dosage on the degree of buckling of the 1D nanowalls. (a-b) Top-view SEM images and schematics (insets) of nanowaves obtained from HL with exposure time of (a) 16 s and (b) 17 s, resulting in line width of 250 nm and 350 nm, respectively, and different degree of buckling. The later has significant amount of fibers formed between the walls. (c-d) Schematics of two-beam interference intensity profile at different exposure dosages. Regions exposed with intensity higher than the threshold are more crosslinked and remained on the substrate after developing in a good solvent. 93

Figure 5.5 Finite element model and buckling prediction, assuming perfect adhesion between the wall and the rigid substrate. (a). Dimension of the wall on the rigid substrate was set according to experiments (pitch 600 nm, width 250-350 nm, height 600-1800 nm, undulation period 2-3 μm). The periodic boundary condition (PBC) was applied on the front (indicated with yellow box in the figure) and rear side of the wall. (b) The predicted buckling mode under swelling. Due to the imposed PBC, the apparent length of the wall (distance between the front and rear side or simply undulation period in the figure) does not change although the actual length of the wall increases during swelling. 94

Figure 5.6 Finite-element simulation of the buckling behaviors of 1D nanowalls. (a-c) Changes in the maximum distance (\bigcirc), minimum distance between walls (\square), and the undulation amplitude (\star) of the same wall width (300 nm) but different aspect ratios, (a) AR=2. (b) AR= 4. (c) AR=6 as a function of the swelling ratio. (d) The corresponding 3D images of the predicted buckling behaviors of 1D walls of different aspect ratios with swelling ratio of 1.1. (e) Top-view simulated images of the wall distance evolution during

buckling. (f) Illustration of nanofibers (yellow) formed mainly in the regions where wall distances are smaller than 200 nm. 95

Figure 5.7 The predicted buckled shape. (a) Top, (b) side, (c) front, (d) overall, and (e, f) cross-sectional views of the buckled walls. The cross-sectional view in (e) indicates slight undulations along y-axis (wall height direction) as well as the obvious undulations along x-axis in (a). 96

Figure 5.8 Effect of nanofibers in between nanowaves (AR=6) to maintain the buckled structure during swelling. (a) Cross-sectional SEM images of nanowaves with a large quantity of interconnecting nanofibers. (b) Top-view SEM image of the nanowaves shown in (a) after 15 min oxygen plasma treatment, showing nearly no nanofibers left. (c-d) Corresponding top-view SEM images of the nanowaves shown in (a) and (b) after re-swelling in PGMEA and drying. 98

Figure 5.9 Comparison of the optical properties between straight 1D nanowalls, 2D nanowaves with long-range ordering, and randomly collapsed nanowaves. (a) UV-Vis transmittance spectra. (b-d) Photos and corresponding top-view SEM images of various nanostructures. Scale bar: 2 μm 99

Figure 5.10 Double exposures to pattern nanowaves together with nanowalls. (a) Schematic illustration of the double exposure process, including HL at visible light first, followed by UV exposure through a photomask. (b-c) SEM images of the hierarchical structure, consisting of nanowaves and nanowalls (width 300 nm, pitch 600 nm, AR ~6) in a microscaled 1D grating (width 10 μm , pitch 20 μm). (c) Double exposed regions showing straight lines with higher filling fraction, while the single exposed regions showing typical nanowaves. (d) Photo of a film double exposed with photomask of letter "N". Inset: optical image of the photomask. The double exposed region appeared more transparent than the surrounding due to higher filling fraction. The latter appeared orange due to reflection from the nanowaves. 100

Chapter 1

Fabrication and dynamic tuning of periodic structures from holographic lithography

1.1 Introduction

Periodic structures, including one-dimensional (1D), two-dimensional (2D) and three-dimensional (3D) ones, offer unique optical, mechanical and surface properties. For example, the shiny colors displayed on butterfly wings and opals have been attributed to the reflection from 3D periodic structures.^[1] Inspired by nature, scientists have developed different techniques and materials to create and tailor periodic structures. The concept of photonic crystals (PCs) was first proposed in the late 1990's,^[2-3] where certain frequency of light can be totally reflected from a crystalline material with periodic undulation of refractive index at a length scale comparable to the light wavelength, creating so-called photonic bandgaps (PBGs).^[4] More recently, it has been suggested that analogy can be drawn to phononic crystals, where mechanical waves are modulated, leading to phononic bandgaps.^[5] Meanwhile, the topography exhibited in the periodic structures are of interest to exploit surface wetting, adhesion, and bioadhesion properties.^[6]

A number of bottom-up and top-down techniques have been developed to fabricate periodic structures of different symmetries, size and materiality, including colloidal assembly,^[7] layer by layer assembly,^[8] two-photon polymerization,^[9] direct laser writing,^[10] and holographic lithography (HL).^[11-13] Among them, HL is highly efficient and versatile, which records laser interference patterns in a photoresist film over a large

area,^[14] creating a wide range of 1D, 2D and 3D structures, including 1D line pattern, 2D hexagonal pillar array,^[15] face center cubic,^[14] simple cubic,^[12] diamond^[13, 16] and diamond-like.^[17-18]

One unique aspect of bioorganisms is that they are not static: they adapt to the surrounding environment. Therefore, it will be interesting to dynamically tune the periodic structures, including lattice constant, spatial symmetry, and/or the refractive index of the building blocks,^[19] in response to an external stimulus, such as temperature,^[20-23] chemicals,^[24-25] mechanical force,^[26-27] light,^[28-29] electrical force,^[30] magnetic force.^[31] In turn, it will change respective photonic, phononic or surface properties. While there have been much effort in creating responsive structures, most of which are templated from colloidal assemblies and the tuning is often achieved by swelling the 2D and 3D structures using a selective solvent, thus, changing the lattice constant, or by changing the refractive index of the surrounding medium. The resulting change of PBG position ranges from several to a few hundreds of nanometers. Nevertheless, the switching of the physical properties remains limited by the aforementioned methods, and the use of liquid or solvent may not be favorable for many practical applications.

Here, we summarize the recent advances in the fabrication of periodic structures, various material choices for fabrication and application, and different dynamic tuning approaches. An overview of the fabrication approaches is given in section 1.2. Typical photoresists for holographic lithography and materials for applications are discussed in section 1.3. In section 1.4, we discuss different types of tunable periodic structures. The

current issues and thesis outline are given in section 1.6.

1.2 Approaches to fabricate periodic structures

There are various top-down and bottom-up approaches for fabrication 1D, 2D and 3D periodic structures with different size, symmetry and materiality. Here, we categorized the mainly studied fabrication techniques into 1D, 2D and 3D capability, as summarized in Table 1.1.

Table 1.1 Different approaches for fabrication of periodic structures

Techniques	One-dimensional	Two-dimensional	Three-dimensional
Photolithography	✓	✓	
Scanning beam lithography	✓	✓	
Soft lithography	✓	✓	
Wrinkle formation	✓	✓	
Colloidal assembly		✓	✓
Block copolymer self assembly	✓	✓	✓
Holographic lithography	✓	✓	✓
Two-photon lithography	✓	✓	✓
Phase mask interference lithography	✓	✓	✓

1.2.1 Photolithography

Photolithography is widely used in microelectronics manufacturing. Briefly, the photolithographic systems project light through a photomask (e.g. a quartz plate with a patterned chromium coating) onto a photoresist at the focal plane. A photoresist is

typically a polymeric material that switches solubility upon exposure to high energy light, e.g. UV light. By definition, positive-tone photoresists switch from insoluble to soluble in a solvent (also called developer) after light exposure, while negative-tone photoresists typically crosslink, thus becoming insoluble in the developer.^[32-34] Photolithography is a parallel process to generate arbitrary patterns on a plane. In current semiconductor nanofabrication, patterns with 14-nm wide features have been achieved with 193-nm immersion lithography, where imaging resolution could be improved by adding high refractive index (n) immersion fluid (e.g. water, $n = 1.47$) between the lens and imaging plane.^[35]

Due to the nature of photolithography, it is capable of direct fabrication of 1D and 2D periodic structures, ranging from nano- to micro- scale with various photoresists. However, the structure aspect ratio (AR= height/feature size) is usually limited, especially when the feature size shrinks to the nanoscale. For example, AR is typically less than 3 in 193 nm lithography.^[36] This could be explained by depth of focus (DOF) and the critical dimension (CD, also the minimum feature size), which are determined by^[37]

$$CD = k_1 \frac{\lambda}{NA} \quad (1.1)$$

$$DOF = k_2 \frac{\lambda}{NA^2} \quad (1.2)$$

where λ is the wavelength of light, NA is the numerical aperture of the lens, and k_1 and k_2 are processing related constants. Decreasing λ and increasing NA could decrease CD . However, DOF is reduced more rapidly. Therefore, multi-step hard mask etching steps

are necessary to create high AR structures for certain inorganic materials, which add complexity and cost to the fabrication.

In addition, high AR structures tend to be distorted due to solvent swelling during developing, as the material modulus decreases, and pattern collapse due to the capillary force upon solvent drying.^[38-40] To address this problem, high AR structures are typically dried using supercritical CO₂ dryer to minimize surface tension effect.

1.2.2 Scanning beam lithography

Scanning beam lithography (also referred as maskless lithography) is a slower and more expensive fabrication method compared with photolithography, due to its serial writing nature. It is mostly used for producing photomasks or for research purpose rather than large scale manufacturing. There are three main types of scanning beam lithography: (i) scanned laser beams, (ii) focused electron beams^[41] and (iii) focused ion beam (FIB)^[42] systems. Among them, e-beam lithography offers pitch size as small as 9 nm.^[41] However, the tools are expensive and the fabrication process is very time-consuming, which limits the practical applications.

1.2.3 Colloidal assembly

Colloidal assembly is a simple and low-cost process to directly fabricate 2D and 3D periodic structures. Mono-dispersed particles could close-packed into hexagonal closest-packed (HCP) structures or face centered cubic (FCC) structures onto a substrate during the slow evaporation of solvent, as a result of attractive capillary forces among the colloidal spheres and the convective particle flux during solvent evaporation. The lattice

constant of the periodic structures are simply controlled by the particle sizes. Colloids are typically made of silica,^[43-45] polystyrene (PS)^[46-47] and poly(methyl methacrylate) (PMMA)^[48-49]. Several different techniques have been studied for colloidal assembly, including dip-coating, spin-coating, sedimentation and epitaxial growing on patterned substrate.^[50-53] Among them, sedimentation is most commonly employed, however, it has very little control over the morphology of top surface and number of layers, which also takes relatively long periods of time (days to months).^[54] The size distribution of particles is very important to quality of the colloidal assembly. If the standard deviation of particle sizes is above 4%, no ordered close-packing could be formed.^[55] Also, controlling the volatility and dielectric constant of the solvent^[56] could help to achieve high quality structures.

The advantages of colloidal assembly are low-cost and large area capability (up to several centimeters square). However, there are also disadvantages: (i) the colloidal crystals are typically poly-crystalline with random defects, and (ii) the structure symmetry is typically limited to FCC and HCP structures.

1.2.4 Block copolymer self-assembly

Block copolymers (BCPs) are macromolecules with two or more segments containing chemically distinct repeating units. They microphase separate into different morphologies to achieve minimum energy configurations. For diblock copolymers, four common morphologies could be formed, including lamellar, cylindrical, spherical and gyroid structures.^[57] The equilibrium morphology is mainly determined by the degree of polymerization (N), volume fraction of each block (f) and segment-segment (Flory-

Huggins) interaction parameter (χ). The domain size is typically around 10-100 nm, which makes BCP self-assembly attractive to create 1D, 2D and even 3D periodic structures that is not possible or costly using top-down approaches.^[58]

One concern about BCP self-assembly is the difficulty in fabricating large-scale defect-free structures. Recently, directed assembly using lithographically or chemically patterned surfaces^[59] has made great progress to create defect-free nanostructures over 100 μm x 100 μm , with minimum feature size as small as 10 nm.^[60] This approach is a combination of top-down and bottom-up approaches, which offers the advantages from both systems. Nevertheless, it remains questionable to fabricate high AR structures with long-range ordering using BCP self-assembly.

1.2.5 Holographic lithography

Holographic lithography (HL), or multi-beam interference lithography, records the interference pattern from multiple coherent beams onto photoresists.^[12, 14] Depending on the number and alignment of the incident beams, the interference pattern varies from 1D to 3D with different symmetries.^[12-13, 15-16, 61] The intensity profile generated by the interference of N monochromatic plane waves of wave vectors \mathbf{k}_i , polarization vectors $\boldsymbol{\varepsilon}_i$, phase θ_i and real amplitudes E_i , is given by

$$I(\mathbf{r}) = \sum_{l=0}^{N-1} \sum_{m=0}^{N-1} E_l E_m |\boldsymbol{\varepsilon}_l^* \cdot \boldsymbol{\varepsilon}_m| \exp[i(\mathbf{k}_l - \mathbf{k}_m) \cdot \mathbf{r} + \theta_l - \theta_m + \varphi_{lm}] \quad (1.3)$$

where $\varphi_{lm} = \arg(\boldsymbol{\varepsilon}_l \cdot \boldsymbol{\varepsilon}_m)$. Therefore, the structure symmetry and lattice constants are controlled by the wave vectors, phase, intensity, wavelength and polarizations of the incident beams.

The fabrication process is similar to conventional photolithography, except that HL is maskless. Briefly, a chemical amplified photoresist solution (containing photoacid generators (PAGs)) is spin-coated on a clean substrate, soft baked to allow solvent evaporation, exposed under interference light to generate photoacids, followed by post-exposure bake (PEB) above the glass transition temperature (T_g) to allow photoacid diffusion and catalyze crosslinking (for negative-tone photoresist) or decomposition (for positive-tone photoresist) reactions. The film is then developed in a good solvent to dissolve the unexposed or weakly exposed regions in the case of negative-tone resists, followed by drying, typically by supercritical drying due to the highly porous nature, to generate periodic structures. Figure 1.1 shows the schematics of the HL to create 1D, 2D and 3D structures, respectively.

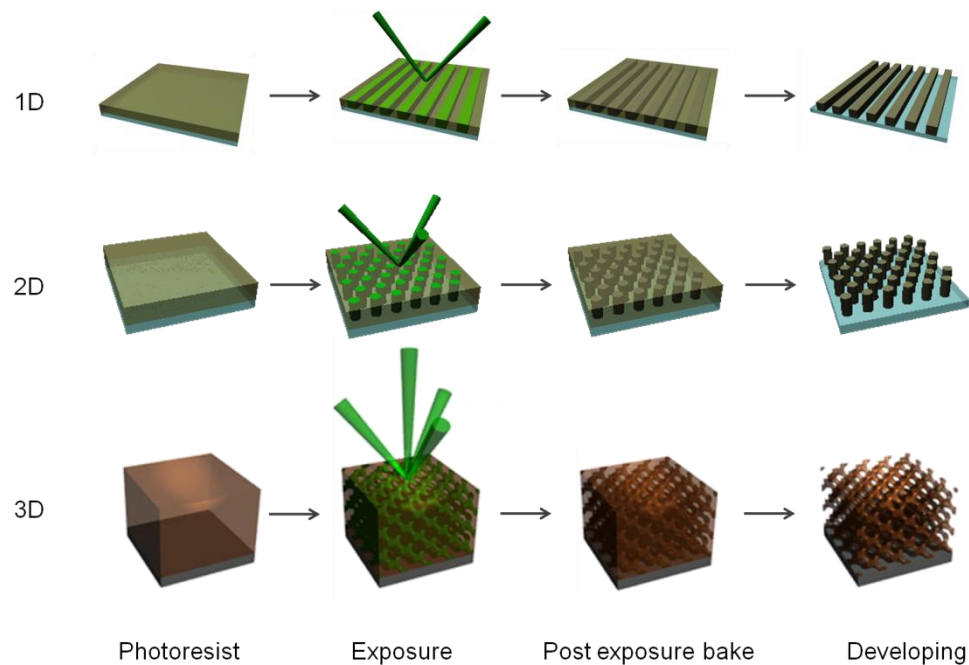


Figure 1.1 Schematic illustration of the 1D, 2D and 3D periodic structures fabricated by holographic lithography in negative-tone photoresists.

HL offers several advantages compared with other fabrication techniques: (i) it is capable of fabricating large-area defect-free structures, (ii) high AR structures are possible using HL since it is not limited by *DOF* as in photolithography, and (iii) it is versatile to fabricate various periodic structures with variable feature sizes by varying the incident beam angles and polarization, including 1D line pattern,^[61-62] 2D hexagonal array,^[15, 63] quasi-crystals,^[64-65] 3D simple cubic (sc),^[12] face-centered cubic (fcc),^[66] body-centered cubic (bcc),^[67] diamond-like^[17] and diamond structures.^[13, 16]

1.3 Material aspects of periodic structures

In recent years there has been considerable effort to develop methods for fabricating periodic structures with different sizes and symmetries. On the other hand, due to the requirement of practical applications, the material aspects of periodic structures became critical. Here we first discuss two main types of photoresists, which are frequently used in this thesis work, and then some important material choices for back-filling or conversion from the photoresist structures.

1.3.1 Photoresists

1.3.1.1 SU-8

SU-8 is a multifunctional epoxy derivative of a bisphenol-A novolac resin with an average of eight epoxy groups per monomer (Figure 1.2). It is the most commonly used negative-tone photoresist in HL, because it is highly transparent in the near-UV and visible regions and capable of preparation of ultra-thick films (up to 2 mm). Upon exposure, SU-8 becomes crosslinked and exhibits high mechanical (Young's modulus up

to 5.0 GPa) and thermal ($T_g > 200$ °C) strength. Thus it has been widely used in micro-electro-mechanical systems (MEMS) devices, high AR structures and 3D periodic structures fabrication.^[17, 68]

It is worth mentioned that typically the modulus of crosslinked SU-8 in holographic lithography is not as high as in photolithography due to lower crosslinking density. During developing, the organic solvent could swell the crosslinked film, which could lead to distortion and volume shrinkage in 3D structures^[69] and buckling in 1D structures. Shrinkage and distortion are undesired features for 3D periodic structures, e.g. as photonic crystals, because they could reduce the optical quality. However, understanding and controlling the mechanical instability could be attractive for both research and applications, such as in the 1D structures, which will be discussed in details in Chapter 5.

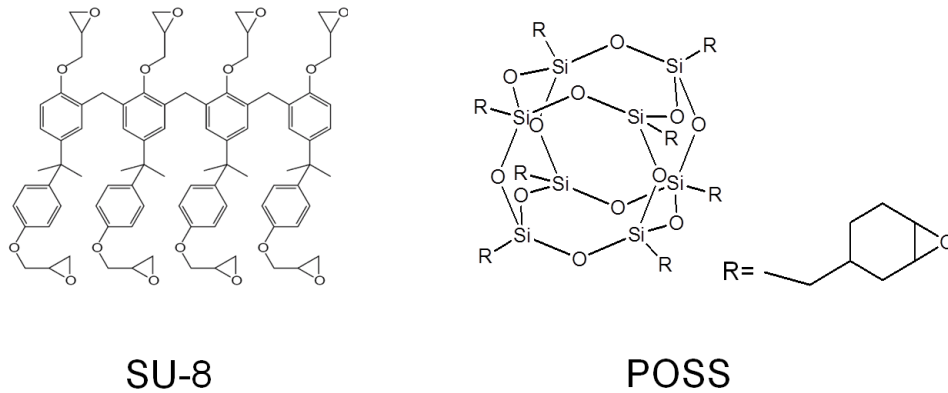


Figure 1.2 Chemical structures of SU-8 and epoxy-functionalized polyhedral oligomeric silsesquioxane (epoxy-POSS).

1.3.1.2 POSS

HL patterned periodic structures are often used as templates to convert the structures into other materials, such as inorganic materials with higher refractive indexes for

photonic applications, and functional organic materials. The conversion of the high refractive index materials are usually conducted at temperature above 350 °C.^[70] for typical organic negative-tone photoresists, e.g. SU-8, they start to degrade above 400 °C and the structures will collapse. They will also swell in an organic solvent, thus, it is not possible to use dissolution method to remove the template at room temperature.

Inorganic-organic hybrid photoresists, such as epoxy-functionalized polyhedral oligomeric silsesquioxane (epoxy-POSS) (Figure 1.2), have been investigated in our group to address the aforementioned problems.^[16, 63, 71-73] Similar to SU-8, photocrosslinking of epoxy-POSS is also based on ring-opening reactions of the epoxy functional groups catalyzed by photoacids. Therefore, it is also a negative-tone photoresist. We have fabricated 1D, 2D and 3D periodic structures with POSS via HL.^[16, 63, 72] The advantages of using POSS are that (i) it offers higher thermal and mechanical strength due to the Si-O skeleton, (ii) it shows little volume shrinkage up to 400 °C,^[74] (iii) it could be converted to silica-like material by direct calcination at 500 °C in an oxygen atmosphere,^[71, 73] (iv) it is dissolvable in hydrofluoric acid (HF) aqueous solution, which made conversion to other organic materials at room temperature possible,^[18, 63] and (v) it is possible to control and tune the surface roughness using different solvents, which could bring in new applications.^[75] More discussions about the surface roughness tuning, the conversion to functional organic materials, and their applications will be presented in Chapter 2, 3, and 4.

1.3.2 High refractive index materials

As mentioned above, periodic structures offer unique optical properties, and they

have been widely investigated for application as photonic crystals (PCs), especially for 3D PCs. However, a complete PBG requires high refractive index (n) contrast between two materials, e.g. 1.9 for diamond structure (the most robust structure symmetry as PC).^[76] However, the refractive indexes of typical organic materials, or specifically photoresists, are not that high. The refractive indexes for SU-8 and POSS are 1.67 and 1.54, respectively. Thus the contrast between these photoresists and air are smaller than 1. As a result, the as-fabricated periodic structures have to be converted to high refractive index materials, such as silicon (Si), germanium (Ge), cadmium selenide (CdSe) and titania (TiO₂), though back-infiltration and template removal. Their refractive indexes and typical conversion methods are summarized in Table 1.2.

Table 1.2 Important material refractive indexes and their conversion methods

Material	Refractive index (n)	Conversion method
Air	1	/
Water	1.33	/
SU-8	1.67	/
Epoxy-POSS	1.52	/
Silicon (Si)	3.45- 4.20	CVD, ^[77] chemical reduction ^[78]
Germanium (Ge)	4.0	CVD ^[79]
Cadmium selenide (CdSe)	2.50-2.75	ECD ^[80]
Silica (SiO ₂)	1.46-1.55	sol-gel, ^[81] ALD, calcination ^[71]
Titania (TiO ₂)	2.2-3.0	sol-gel, ^[82] ALD, ^[83] ECD ^[84]

Many techniques have been investigated to convert the periodic structure templates into the materials on demand, including chemical vapor deposition (CVD) for

semiconducting materials,^[77, 79] atomic layer deposition (ALD) for metal oxide and nitride materials,^[83] sol-gel reaction for metal oxides,^[81-82] electro-chemical deposition (ECD),^[80, 84] direct calcinations to silica^[71] and chemical reduction for silicon.^[78] Among them, CVD and chemical reduction are high temperature processes, which require a double template method by first converting the organic template to silica. Silica template is more thermally and mechanically stable, which could be removed later by HF etching. Therefore, direct calcinations from POSS structures to silica-like ones could be very beneficial for these conversion techniques, since it greatly reduced the steps for achieving final material conversion.

1.3.3 Functional organic materials

In addition to the applications in photonics, periodic structures are of interests for a wide range of applications, including phononic crystals, optical displays and sensors, which are responsive to external stimuli. For the latter purpose, it is necessary to convert the structure from photoresist template to different kinds of functional organic materials, including elastomers, hydrogels, shape memory polymers (SMPs) and liquid crystal elastomers (LCEs).

Elastomeric 1D and 2D structures, such as from polydimethylsiloxane (PDMS), could be converted from the photoresist templates via soft lithography (or replica molding).^[85] For hydrogels, SMPs and LCEs structures, typically they are fabricated via a double replicating method using PDMS as a mold.

For 3D structures, however, it is not possible to use conventional soft lithography approaches. If the template is made of positive-tone photoresist, it will be selectively

dissolved by choosing a proper solvent. For organic negative-tone photoresists, e.g. SU-8, the crosslinked network could only swell but not be dissolved, therefore, thermal degradation above 500°C is typically applied to remove the template. Thus, it is not possible to template polymeric functional structures using negative-tone templates. Using hybrid photoresist, e.g. epoxy-POSS (see chemical structure in Fig. 1.2), We demonstrated that 3D PDMS^[18] and 3D SMP could be fabricated by back-infiltration PDMS and SMP precursors into the epoxy-POSS templates, followed by HF etching. The image of latter is shown in Figure 1.3, which summaries the epoxy-POSS and SMP structures I fabricated with HL in this thesis. More discussion about SMPs conversion will be presented in Chapter 3.

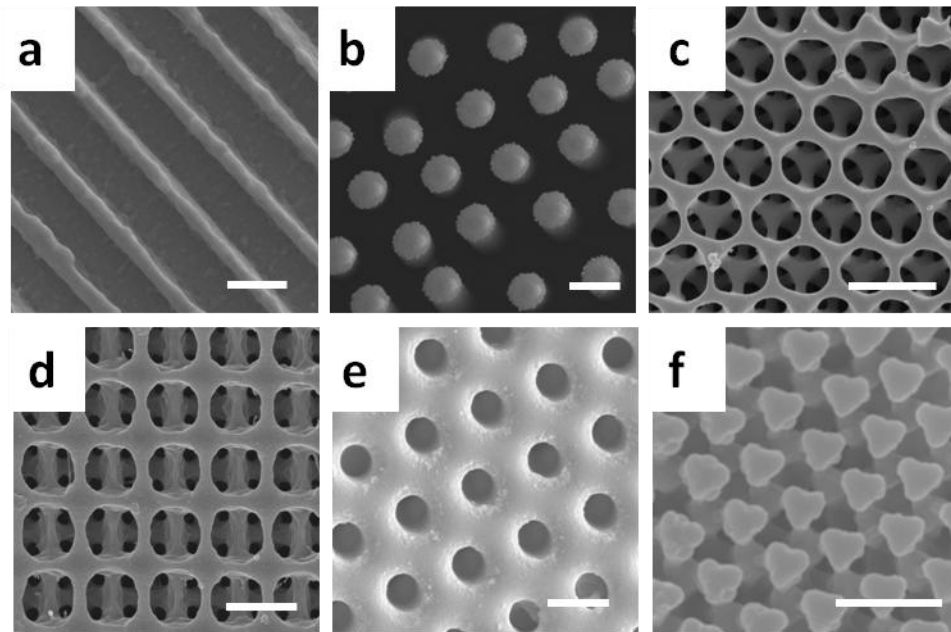


Figure 1.3 Examples of periodic structures directly fabricated with HL in epoxy-POSS and the converted SMP structures. (a) 1D nanogratings, (b) 2D hexagonal pillar array, (c) 3D diamond-like structure, (d) 3D diamond structure, (e) 2D SMP membrane converted from (b), and (f) 3D SMP inversed diamond-like structure converted from (d). Scale bar: 2 μm .

1.4 Tunable periodic structures

As we mentioned earlier, it is attractive to dynamically tune the periodic structures, including 1D, 2D and 3D. In response to an external stimulus, such as temperature,^[20-23] chemicals,^[24-25] mechanical force,^[26-27] light,^[28-29] electrical force^[30] and magnetic force,^[31] the lattice constant, refractive index contrast, ordering and/or spatial symmetry of the periodic structures could be altered, leading to change of photonic, phononic or surface properties. There have been much effort in creating tunable structures, most of which are templated from colloidal assemblies and the tuning is often achieved by swelling the 2D and 3D structures using a selective solvent, thus, changing the lattice constant, or the refractive index of the surrounding medium. Here, we category the tunable periodic structures by types of external stimuli.

1.4.1 Thermal responsive periodic structures

Thermal responsive periodic structures, by definition, change their properties according to temperature change. It could be achieved in organic materials or inorganic materials, by either changing the lattice constant or the refractive index.

The first type is made by incorporating thermal responsive hydrogels, such as poly(N-isopropylacrylamide) (PNIPAAm), into the colloidal assembly. PNIPAAm is a temperature-sensitive polymer, which undergoes a reversible volume phase transition between a hydrated state and a dehydrated state around the lower critical solution temperature (LCST, 32 °C) in water. Asher *et al.*^[20] pioneered in this type of research, by embedding non-close-packed 3D colloidal crystal into the PNIPAAm network. When the temperature increases, the polymer expels water and shrinks so that the inter-particle

distance decreases, leading to a blue shift in the diffraction.

The second type is made of inorganic materials, which have phase transition according to temperature change, resulting in significant change in the refractive index of the building blocks. Xia *et al.* fabricated 3D periodic structures by assembling core-shell particles comprising α -Se cores and Ag₂Se shells.^[23] Ag₂Se has a phase transition between semiconductive β type and conductive α type around 133 °C, which results in the refractive index change from 2.98 to 2.86 (at 2 μ m wavelength). Therefore, the diffraction peak had a red-shift from 1392 nm to 1497 nm as the temperature rose from 110 °C to 150 °C.

1.4.2 Chemical responsive periodic structures

Chemical responsive periodic structures include those hydrogel structures responsive to solvent, vapor, pH and ionic strength changes, which lead to lattice constants change. When hydrogels are chemically attached with a molecular-recognition group, e.g. crown ether, which could selectively bind with metal ions, such as Pb²⁺, Ba²⁺, and K⁺, the periodic structure lattice constant could be changed according to the osmotic pressure variation.^[24, 86-87] Similarly, pH responsive periodic structures were made by incorporating poly (acrylic acid) (PAA) into the system, which swells more at high pH values. The disadvantage of using hydrogel is the relatively long switching time, which usually takes several to tens of minutes.

1.4.3 Mechanical responsive periodic structures

Investigations on mechanical responsive periodic structures were mainly focused on

colloid – hydrogel / elastomer composite films, which can be stretched or compressed to change the lattice constant or symmetry.^[26-27] In comparison with thermal and chemical triggers, mechanical force is more straightforward and large. However, it requires materials with high mechanical robustness to withstand long switching cycles and aging effect.

Recently, we and several other groups have reported pattern transformation in periodically porous membranes from PDMS elastomers,^[88] pH / thermal responsive hydrogels,^[89] and shape memory polymers.^[63] For instance, under mechanical compression by swelling induced osmotic pressure, a PDMS membrane consisting of micron-sized circular holes in a square array buckles to ellipsics, where the neighboring units are arranged perpendicular to each other.^[88, 90-91] It is found that both PGB properties and mechanical behaviors could be significantly altered by the symmetry change during pattern transformation.^[90, 92-93] The symmetry-changing periodic structures are promising, since it could lead to much larger change in the optical properties, compared with lattice constant or refractive index changes in the above mentioned approaches, such as from transparency to colorful state. More discussions about mechanical instability triggered symmetry change in 1D and 2D periodic structure will be presented in Chapter 3 and 5.

1.4.4 Light responsive periodic structures

Since light offers better spatial control and energy efficiency compared with thermal, mechanical or chemical triggers, there have been many efforts to explore light responsiveness in periodic structures. Most of the studies are based on colloidal assembly,

where the colloids could be functionalized with photo-sensitive chemicals. These studies include a malachite green carbinol base (MG)-infiltrated silica colloidal crystal,^[28] a spirobenzopyran chromophore-covalently attached polymer/crystal composite,^[94] and a photochromic liquid crystal-infiltrated silica inverse opal.^[29] The structure is tuned by changing the surface charges of the particles, or refractive index between aggregated and disaggregated states or near the nematic-isotropic phase transition.

Recently, light responsive periodic structures have also been made from functional organic materials, such as liquid crystal elastomers (LCEs), crowned spirobenzopyran incorporated polymers and gold nanorods (Au NRs) incorporated SMPs. LCEs containing azobenzene groups undergo *trans to cis* conformational change upon exposure to UV light or vice versa via visible light. It has been widely studied as actuators that can convert light input at the molecular level to macroscopic volume change, leading to reversible contraction and expansion.^[95-97] Similarly, vinyl polymers carrying crowned spirobenzopyran moieties, show photochromism in the presence of alkali metal ions, due to photoisomerization effect.^[98] Au NRs are known to have photothermal effect in the visible and near IR regions, which convert the absorbed light energy to thermal energy. By incorporating Au NRs into the SMPs, the structure tuning mechanism could be altered from temperature-mechanical to light-mechanical force.^[99]

1.4.5 Electrically responsive periodic structures

Electrically responsive periodic structures are very attractive for both research and applications, since they usually offer fast switching speed, good spatial control, energy efficiency and compatibility to the electronic devices in our daily life. There are several

types of electrically responsive periodic structures. The first type is by infiltration liquid crystals (LCs) into the voids of the assembled colloids. Upon voltage change, the LC molecules go through a reorientation along the electric field, thereby changing their refractive index.^[100-102]

The second type is electrochemical responsive periodic structures. Ozin *et al.*^[30] constructed such a structure using colloidal assembly and a crosslinked metallopolymer network (polyferrocenylsilane (PFS) derivatives with pendant C=C bonds) with a continuously variable degree of oxidation. Their previous study have shown that such composite film have redox induced solvent swelling. That is, when alternating the electric field, the structure swells or deswells according to different redox states. The switching is usually done within seconds.

The third type is polyelectrolyte hydrogels. For instance, a porous poly (N-isopropylacrylamide-*co*-methacrylic acid) inverse opal exhibited electrochemically triggered switching between two colors, because of the spatial-temporal change in pH value that leads to osmotic pressure change, which in turn changes the swelling behavior.^[103]

1.4.6 Magnetic responsive periodic structures

The magnetic responsive periodic structures are based on pre-assembled colloids, which contain magnetic nanoparticles. For example, superparamagnetic polystyrene (PS) colloids, which contain 17 wt% iron oxide nanoparticles, could self-assemble into non-close-packed crystalline in deionized water in a confined volume.^[31] Applying the magnetic field could alter the lattice constant of the 3D colloidal assembly. However, due

to the small spacing between pre-assembled colloids, the change in spacing is rather limited, so is the tuning range. On the other hand, many of the above mentioned tunable periodic structures have solvent involved, which might not be desired for many practical applications.

1.5 Current issues and thesis outline

While there has been much effort to fabricate static and tunable periodic structures with different symmetries and materials by various approaches, it remains challenging to address several issues, such as the degree of tunability and mechanical instability. In this thesis, I aim to investigate the intrinsic structure-property relationship in the periodic structures fabricated by HL, harness the mechanical instability to create highly ordered structures and utilize large deformation for pattern transformation, which in turn allowing me to explore novel applications of tunable periodic structures.

While many of the current studies of periodic structures have focused on their unique optical and mechanical properties, we are interested in multi-functionality of these materials. For instance, surface property of periodic structures is also interesting due to the intrinsic topography, which is closely related to wetting, adhesion and adsorption behaviors. It is known that *Morpho* butterfly wings are not only colorful but also superhydrophobic.^[104] Gecko feet hairs show strong dry adhesion and superhydrophobicity due to the hierarchical structure consisting of hundreds of submicron-sized spatula structures within each micron-sized setae.^[105] To mimic them while not interfering the optical/mechanical effects of the periodic structures, it is important to control surface roughness. In Chapter 2, I will show exploitation of

nanoroughness on the surface of 3D diamond structures fabricated by HL, for wetting and adsorption of small molecules.

As I mentioned in the tunable periodic structures section, most of the current approaches to tune the photonic properties are based on changing lattice constant or refractive index, resulting in change of PBG position up to a few hundreds of nanometers. It will be attractive if we could expand this tunable range, for example, from transparency to colorful states. In Chapter 3, we explored the pattern transformation and symmetry change by compressing 2D SMP membrane with pores arranged in a hexagonal array to realize the reconfigurable switching between transparency and colorful states according to thermal-mechanical stimulus.

Direct fabricating of high AR periodic structures by top-down lithographic approaches, especially in the nano-scale, is still challenging, due to limitations of *DOF* in photolithography, pattern collapse from capillary force and distortion due to solvent swelling. In Chapter 4 and 5, I discuss the fabrication of nano-scale 1D periodic structures via HL from different photoresists, i.e. POSS and SU-8. The 1D structures are of interests for gratings,^[106] plasma etching masks^[107-108] and photonic / phononic crystal applications.^[109] Using HL and supercritical drying, we could avoid the problems of *DOF* and pattern collapse when fabricating high AR 1D structures. However, solvent swelling induced instability could induce buckling of the 1D structures. As shown in Chapter 4, high AR (up to 10) straight line patterns were fabricated using epoxy POSS as photoresists, which have high thermal and mechanical strength. In Chapter 5, I utilized the buckling instability and formation of nanofibers in HL above the exposure threshold

to transform the 1D nanowalls to long-range ordered 2D nanowaves. In each chapter, we study the pattern formation and deformation mechanisms.

In Chapter 6, I summarize the studies in this thesis and suggest future directions.

1.6 References

- [1] P. Vukusic; J. R. Sambles, *Nature* **2003**, *424*, 852-855.
- [2] E. Yablonovitch, *Physical Review Letters* **1987**, *58*, 2059.
- [3] S. John, *Physical Review Letters* **1987**, *58*, 2486.
- [4] J. D. Joannopoulos; S. G. Johnson; J. N. Winn; R. D. Meade, *Photonic Crystals: Molding the Flow of Light*. 2nd ed.; Princeton University Press: Princeton, NJ, 2008.
- [5] S. X. Yang; J. H. Page; Z. Y. Liu; M. L. Cowan; C. T. Chan; P. Sheng, *Physical Review Letters* **2004**, *93*.
- [6] F. A. Denis; P. Hanarp; D. S. Sutherland; J. Gold; C. Mustin; P. G. Rouxhet; Y. F. Dufrêne, *Langmuir* **2002**, *18*, 819-828.
- [7] G. Subramanian; V. N. Manoharan; J. D. Thorne; D. J. Pine, *Advanced Materials* **1999**, *11*, 1261-1265.
- [8] S. Y. Lin; J. G. Fleming; D. L. Hetherington; B. K. Smith; R. Biswas; K. M. Ho; M. M. Sigalas; W. Zubrzycki; S. R. Kurtz; J. Bur, *Nature* **1998**, *394*, 251-253.
- [9] S. Kawata; H. B. Sun; T. Tanaka; K. Takada, *Nature* **2001**, *412*, 697-698.
- [10] M. Deubel; G. Von Freymann; M. Wegener; S. Pereira; K. Busch; C. M. Soukoulis, *Nature materials* **2004**, *3*, 444-447.
- [11] M. Campbell; D. Sharp; M. Harrison; R. Denning; A. Turberfield, *Nature* **2000**,

404, 53-56.

- [12] C. K. Ullal; M. Maldovan; E. L. Thomas; G. Chen; Y. J. Han; S. Yang, *Applied physics letters* **2004**, *84*, 5434.
- [13] M. Maldovan; E. L. Thomas, *Nature materials* **2004**, *3*, 593-600.
- [14] M. Campbell; D. N. Sharp; M. T. Harrison; R. G. Denning; A. J. Turberfield, *Nature* **2000**, *404*, 53-56.
- [15] J. H. Moon; A. J. Kim; J. C. Crocker; S. Yang, *Adv. Mater.* **2007**, *19*, 2508-2512.
- [16] G. Q. Liang; X. L. Zhu; Y. G. Xu; J. Li; S. Yang, *Adv. Mater.* **2010**, *22*, 4524-4529.
- [17] J. H. Moon; J. Ford; S. Yang, *Polym. Adv. Tech.* **2006**, *17*, 83-93.
- [18] Y. Xu; X. Zhu; S. Yang, *ACS nano* **2009**, *3*, 3251-3259.
- [19] J. Ge; Y. Yin, *Angewandte Chemie International Edition* **2011**, *50*, 1492-1522.
- [20] J. M. Weissman; H. B. Sunkara; A. S. Tse; S. A. Asher, *Science* **1996**, *274*, 959.
- [21] M. Kumoda; M. Watanabe; Y. Takeoka, *Langmuir* **2006**, *22*, 4403-4407.
- [22] J. H. Kang; J. H. Moon; S. K. Lee; S. G. Park; S. G. Jang; S. Yang; S. M. Yang, *Advanced Materials* **2008**, *20*, 3061-3065.
- [23] U. Jeong; Y. Xia, *Angewandte Chemie* **2005**, *117*, 3159-3163.
- [24] J. H. Holtz; S. A. Asher, *Nature* **1997**, *389*, 829-832.
- [25] C. Blanford; R. Schrodin; M. Al Daous; A. Stein, *Advanced Materials* **2001**, *13*, 26-29.
- [26] S. A. Asher; J. Holtz; L. Liu; Z. Wu, *Journal of the American Chemical Society* **1994**, *116*, 4997-4998.
- [27] K. Sumioka; H. Kayashima; T. Tsutsui, *Advanced Materials* **2002**, *14*, 1284-1286.

- [28] Z. Z. Gu; A. Fujishima; O. Sato, *Journal of the American Chemical Society* **2000**, *122*, 12387-12388.
- [29] S. Kubo; Z. Z. Gu; K. Takahashi; Y. Ohko; O. Sato; A. Fujishima, *Journal of the American Chemical Society* **2002**, *124*, 10950-10951.
- [30] A. C. Arsenault; D. P. Puzzo; I. Manners; G. A. Ozin, *Nature Photonics* **2007**, *1*, 468-472.
- [31] X. Xu; G. Friedman; K. D. Humfeld; S. A. Majetich; S. A. Asher, *Chemistry of Materials* **2002**, *14*, 1249-1256.
- [32] M. D. Stewart; K. Patterson; M. H. Somervell; C. G. Willson, *J. Phys. Org. Chem.* **2000**, *13*, 767-774.
- [33] C. G. Willson; B. C. Trinque, *J. Photopolym Sci. Technol.* **2003**, *16*, 621-627.
- [34] H. Ito, *J. Polym. Sci. Pol. Chem.* **2003**, *41*, 3863-3870.
- [35] D. P. Sanders, *Chem. Rev.* **2010**, *110*, 321-360.
- [36] *International Technology Roadmap for Semiconductors.*
- [37] S. Okazaki, *J. Vac. Sci. Technol. B* **1991**, *9*, 2829-2833.
- [38] T. Tanaka; M. Morigami; H. Oizumi; T. Ogawa, *Jpn. J. Appl. Phys. Part 1 - Regul. Pap. Short Notes Rev. Pap.* **1993**, *32*, 5813-5814.
- [39] M. P. Stoykovich; H. B. Cao; K. Yoshimoto; L. E. Ocola; P. F. Nealey, *Adv. Mater.* **2003**, *15*, 1180-1184.
- [40] D. Chandra; S. Yang, *Langmuir* **2009**, *25*, 10430-10434.
- [41] J. K. W. Yang; B. Cord; H. G. Duan; K. K. Berggren; J. Klingfus; S. W. Nam; K. B. Kim; M. J. Rooks, *J. Vac. Sci. Technol. B* **2009**, *27*, 2622-2627.
- [42] D. Winston; V. R. Manfrinato; S. M. Nicaise; L. L. Cheong; H. Duan; D. Ferranti;

- J. Marshman; S. McVey; L. Stern; J. Notte; K. K. Berggren, *Nano Lett.* **2011**, *11*, 4343-4347.
- [43] P. Masse; R. A. L. Vallee; J. F. Dechezelles; J. Rosselgong; E. Cloutet; H. Cramail; X. S. Zhao; S. Ravaine, *J. Phys. Chem. C* **2009**, *113*, 14487-14492.
- [44] J. P. Ge; H. Lee; L. He; J. Kim; Z. D. Lu; H. Kim; J. Goebel; S. Kwon; Y. D. Yin, *J. Am. Chem. Soc.* **2009**, *131*, 15687-15694.
- [45] F. Piret; Y. U. Kwon; B. L. Su, *Chem. Phys. Lett.* **2009**, *472*, 207-211.
- [46] C. E. Reese; C. D. Guerrero; J. M. Weissman; K. Lee; S. A. Asher, *J. Colloid Interface Sci.* **2000**, *232*, 76-80.
- [47] Z. F. Liu; T. Ding; G. Zhang; K. Song; K. Clays; C. H. Tung, *Langmuir* **2008**, *24*, 10519-10523.
- [48] R. C. Schroden; M. Al-Daous; C. F. Blanford; A. Stein, *Chem. Mat.* **2002**, *14*, 3305-3315.
- [49] J. G. Deng; X. M. Tao; P. Li; P. Xue; Y. H. Zhang; X. H. Sun; K. C. Kwan, *J. Colloid Interface Sci.* **2005**, *286*, 573-578.
- [50] N. D. Denkov; O. D. Velev; P. A. Kralchevsky; I. B. Ivanov; H. Yoshimura; K. Nagayama, *Nature* **1993**, *361*, 26-26.
- [51] P. V. Braun; R. W. Zehner; C. A. White; M. K. Weldon; C. Kloc; S. S. Patel; P. Wiltzius, *Adv. Mater.* **2001**, *13*, 721-724.
- [52] J. H. Moon; G. R. Yi; S. M. Yang, *J. Colloid Interface Sci.* **2005**, *287*, 173-177.
- [53] T. Okubo, *Colloid Polym. Sci.* **2008**, *286*, 1307-1315.
- [54] Y. N. Xia; B. Gates; Y. D. Yin; Y. Lu, *Adv. Mater.* **2000**, *12*, 693-713.
- [55] M. Allard; E. H. Sargent, *Appl. Phys. Lett.* **2004**, *85*, 5887-5889.

- [56] A. Mihi; M. Ocana; H. Miguez, *Adv. Mater.* **2006**, *18*, 2244-2249.
- [57] F. S. Bates; G. H. Fredrickson, *Annu. Rev. Phys. Chem.* **1990**, *41*, 525-557.
- [58] A. M. Urbas; M. Maldovan; P. DeRege; E. L. Thomas, *Adv. Mater.* **2002**, *14*, 1850-1853.
- [59] S. B. Darling, *Prog. Polym. Sci.* **2007**, *32*, 1152-1204.
- [60] C. C. Liu; A. Ramirez-Hernandez; E. Han; G. S. W. Craig; Y. Tada; H. Yoshida; H. M. Kang; S. X. Ji; P. Gopalan; J. J. de Pablo; P. F. Nealey, *Macromolecules* **2013**, *46*, 1415-1424.
- [61] A. Yen; E. H. Anderson; R. A. Ghanbari; M. L. Schattenburg; H. I. Smith, *Appl. Optics* **1992**, *31*, 4540-4545.
- [62] J. M. Carter; D. B. Olster; M. L. Schattenburg; A. Yen; H. I. Smith, *J. Vac. Sci. Technol. B* **1992**, *10*, 2909-2911.
- [63] J. Li; J. Shim; J. Deng; J. T. B. Overvelde; X. Zhu; K. Bertoldi; S. Yang, *Soft Matter* **2012**, *8*, 10322-10328.
- [64] W. D. Mao; G. Q. Liang; H. Zou; R. Zhang; H. Z. Wang; Z. H. Zeng, *J. Opt. Soc. Am. B-Opt. Phys.* **2006**, *23*, 2046-2050.
- [65] X. Wang; C. Y. Ng; W. Y. Tam; C. T. Chan; P. Sheng, *Adv. Mater.* **2003**, *15*, 1526-1528.
- [66] Y. V. Miklyaev; D. C. Meisel; A. Blanco; G. von Freymann; K. Busch; W. Koch; C. Enkrich; M. Deubel; M. Wegener, *Appl. Phys. Lett.* **2003**, *82*, 1284-1286.
- [67] Y. K. Lin; P. R. Herman, *J. Appl. Phys.* **2005**, *98*.
- [68] A. del Campo; C. Greiner, *J. Micromech. Microeng.* **2007**, *17*, R81-R95.
- [69] X. L. Zhu; Y. G. Xu; S. Yang, *Opt. Express* **2007**, *15*, 16546-16560.

- [70] H. Miguez; N. Tetreault; B. Hatton; S. M. Yang; D. Perovic; G. A. Ozin, *Chem. Commun.* **2002**, 2736-2737.
- [71] J. H. Moon; J. S. Seo; Y. G. Xu; S. Yang, *J. Mater. Chem.* **2009**, *19*, 4687-4691.
- [72] Y. A. Xu; X. L. Zhu; S. Yang, *ACS Nano* **2009**, *3*, 3251-3259.
- [73] Y. A. Xu; M. Guron; X. L. Zhu; L. G. Sneddon; S. Yang, *Chem. Mat.* **2010**, *22*, 5957-5963.
- [74] J. H. Moon; S. Yang, *Chem. Rev.* **2009**, *110*, 547-574.
- [75] J. Li; G. Q. Liang; X. L. Zhu; S. Yang, *Adv. Funct. Mater.* **2012**, *22*, 2980-2986.
- [76] M. Maldovan; A. M. Urbas; N. Yufa; W. C. Carter; E. L. Thomas, *Phys. Rev. B* **2002**, *65*, 165123.
- [77] W. T. Dong; H. Bongard; B. Tesche; F. Marlow, *Adv. Mater.* **2002**, *14*, 1457-1460.
- [78] Z. H. Bao; M. R. Weatherspoon; S. Shian; Y. Cai; P. D. Graham; S. M. Allan; G. Ahmad; M. B. Dickerson; B. C. Church; Z. T. Kang; H. W. Abernathy; C. J. Summers; M. L. Liu; K. H. Sandhage, *Nature* **2007**, *446*, 172-175.
- [79] H. Miguez; E. Chomski; F. Garcia-Santamaria; M. Ibisate; S. John; C. Lopez; F. Meseguer; J. P. Mondia; G. A. Ozin; O. Toader; H. M. van Driel, *Adv. Mater.* **2001**, *13*, 1634-1637.
- [80] P. V. Braun; P. Wiltzius, *Nature* **1999**, *402*, 603-604.
- [81] B. T. Holland; C. F. Blanford; T. Do; A. Stein, *Chem. Mat.* **1999**, *11*, 795-805.
- [82] D. Y. Wang; R. A. Caruso; F. Caruso, *Chem. Mat.* **2001**, *13*, 364-371.
- [83] E. Graugnard; J. S. King; D. P. Gaillot; C. J. Summers, *Adv. Funct. Mater.* **2006**, *16*, 1187-1196.
- [84] Y. Xu; X. Zhu; Y. Dan; J. H. Moon; V. W. Chen; A. T. Johnson; J. W. Perry; S.

Yang, *Chemistry of Materials* **2008**, *20*, 1816-1823.

- [85] Y. N. Xia; G. M. Whitesides, *Annu. Rev. Mater. Sci.* **1998**, *28*, 153-184.
- [86] C. E. Reese; S. A. Asher, *Anal. Chem.* **2003**, *75*, 3915-3918.
- [87] J. H. Holtz; J. S. W. Holtz; C. H. Munro; S. A. Asher, *Anal. Chem.* **1998**, *70*, 780-791.
- [88] Y. Zhang; E. A. Matsumoto; A. Peter; P. C. Lin; R. D. Kamien; S. Yang, *Nano Lett.* **2008**, *8*, 1192-1196.
- [89] X. L. Zhu; G. X. Wu; R. Dong; C. M. Chen; S. Yang, *Soft Matter* **2012**, *8*, 8088-8093.
- [90] J. H. Jang; C. Y. Koh; K. Bertoldi; M. C. Boyce; E. L. Thomas, *Nano Lett.* **2009**, *9*, 2113-2119.
- [91] T. Mullin; S. Deschanel; K. Bertoldi; M. C. Boyce, *Physical Review Letters* **2007**, *99*, 084301.
- [92] X. L. Zhu; Y. Zhang; D. Chandra; S. C. Cheng; J. M. Kikkawa; S. Yang, *Appl. Phys. Lett.* **2008**, *93*, 161911.
- [93] K. Bertoldi; P. M. Reis; S. Willshaw; T. Mullin, *Advanced Materials* **2010**, *22*, 361-366.
- [94] M. K. Maurer; I. K. Lednev; S. A. Asher, *Adv. Funct. Mater.* **2005**, *15*, 1401-1406.
- [95] M. Warner; E. M. Terentjev, in *Liquid Crystal Elastomers*. Oxford University Press: New York, **2007**.
- [96] H. Yang; A. Buguin; J. M. Taulemesse; K. Kaneko; S. Me ry; A. Bergeret; P. Keller, *Journal of the American Chemical Society* **2009**, *131*, 15000-15004.
- [97] Z. Yang; A. George; S. M. Clarke; A. R. Tajbakhsh; E. M. Terentjev; W. T. S.

- Huck, *Journal of the American Chemical Society* **2006**, *128*, 1074-1075.
- [98] K. Kimura; H. Sakamoto; R. M. Uda, *Macromolecules* **2004**, *37*, 1871-1876.
- [99] K. C. Hribar; R. B. Metter; J. L. Ifkovits; T. Troxler; J. A. Burdick, *Small* **2009**, *5*, 1830-1834.
- [100] K. Yoshino; S. Satoh; Y. Shimoda; Y. Kawagishi; K. Nakayama; M. Ozaki, *Jpn. J. Appl. Phys. Part 2 - Lett.* **1999**, *38*, L961-L963.
- [101] Y. Shimoda; M. Ozaki; K. Yoshino, *Appl. Phys. Lett.* **2001**, *79*, 3627-3629.
- [102] M. Ozaki; Y. Shimoda; M. Kasano; K. Yoshino, *Adv. Mater.* **2002**, *14*, 514-518.
- [103] K. Ueno; K. Matsubara; M. Watanabe; Y. Takeoka, *Adv. Mater.* **2007**, *19*, 2807-2812.
- [104] Z.-Z. Gu; H. Uetsuka; K. Takahashi; R. Nakajima; H. Onishi; A. Fujishima; O. Sato, *Angewandte Chemie International Edition* **2003**, *42*, 894-897.
- [105] K. Autumn; Y. A. Liang; S. T. Hsieh; W. Zesch; W. P. Chan; T. W. Kenny; R. Fearing; R. J. Full, *Nature* **2000**, *405*, 681-685.
- [106] M. Ahn; R. K. Heilmann; M. L. Schattenburg, *J. Vac. Sci. Technol. B* **2007**, *25*, 2593-2597.
- [107] Y. C. Tseng; A. U. Mane; J. W. Elam; S. B. Darling, *Adv. Mater.* **2012**, *24*, 2608-2613.
- [108] M. K. Hooda; M. Wadhwa; S. Verma; M. M. Nayak; P. J. George; A. K. Paul, *Vacuum* **2010**, *84*, 1142-1148.
- [109] K. Hosomi; T. Fukamachi; H. Yamada; T. Katsuyama; Y. Arakawa, *Photonics Nanostruct.* **2006**, *4*, 30-34.

Chapter 2

Exploiting Nano-roughness on Holographically Patterned Three-Dimensional Photonic Crystals

2.1 Introduction

The colorful display exhibited in butterfly wings, beetle scales, and opals,^[1-6] due to the structural coloration has attracted significant attention in research. Structural color is typically caused by the interference, diffraction, or scattering of light by arrays of transparent materials, such as multiple thin layers, grating, and particles of a size comparable with the wavelength of light. Light is strongly reflected by constructive interference between reflections from the different interfaces of a stack of thin films of alternately high and low refractive index. When the periodic modulation of refractive index is arranged in three dimensions (3D), interference of the light waves leads to complete stop bands or photonic band gaps (PBG), where the light of a particular wavelength is totally reflected in a photonic crystal.^[7-8] Photonic crystals are of interest for a wide range of applications, including ultra-high-bandwidth integrated optical circuits, lasing, sensing, spectroscopy, and pulse shaping. Besides photonic crystals, 3D periodic microstructures are of interest as phononic crystals,^[9-10] solar cell electrodes,^[11-13] and catalyst support.^[14]

In Nature, bioorganisms often possess hierarchical architecture with multiple functions. For example, it is discovered that *Morpho* butterfly wings, which are known for their brilliant blue color as a result of quasi-multilayer interference, are also superhydrophobic due to the nano-roughness appeared on top of the multilayers.^[15] Dual-

scale roughness has been found essential to the superhydrophobic, self-cleaning natural surfaces, such as lotus leaves,^[16] gecko feet hairs^[17] and water strider legs.^[18] It is suggested that nano-roughness enhances the non-wettability, especially when the feature size of the microstructures is large and the asperity is small.^[19-23] Along with the nano-roughness is the enlarged surface area, which is highly desirable to improve the absorption of functional nanomaterials (e.g. dye molecules, nanoparticles, quantum dots, and biomolecules) for potential applications, including solar cells, batteries and catalyst support, bio-imaging, and chemical, gas and biosensors.^[12-14, 24-26]

Several functional, multi-scaled periodic structures have been reported, including dual-scale colloidal assembly as superhydrophobic synthetic opals,^[15] 3D periodic microstructures with internal nanopatterns generated by truncated multi-prism arrays for biosensing,^[27] and surface functionalized diatoms as gas sensors,^[25, 28] and hierarchical TiO₂ electrode templated from colloidal assembly on a holographically patterned 3D microstructures for dye sensitized solar cells (DSSCs).^[13] These methods, however, often require sophisticated chemical reactions and nano- and microfabrication processes to introduce nano-roughness onto the microstructures. Here, we exploit microphase separation of crosslinked polymer chains from nonsolvents to generate nano-roughness (\leq 120 nm) on holographically patterned diamond photonic crystals. The degree of nano-roughness can be controlled by tuning the crosslinking density of the polymer network via changing the loading of photoacid generators and exposure dosage, and the choice of solvent. The nano-roughness does not alter the photonic bandgap position in the infrared region. We show that the combination of periodic microstructure and nano-roughness could offer new opportunities to realize superhydrophobicity and enhanced dye

adsorption on the 3D photonic crystals.

2.2 Experimental methods

2.2.1 Holographic lithography

The diamond photonic crystal was fabricated by holographic lithography (HL) using dual-beam quadruple exposure method ^[29]. In brief, the photoresist film was prepared from 70 wt% epoxy-functionalized cyclohexyl polyhedral oligomeric silsesquioxane (epoxy-POSS, EP0408 from Hybrid Plastics) and 0.3-1.0 wt% (relative to the mass of epoxy-POSS) Irgacure 261 (visible photoacid generator, Ciba Specialty Chemicals) in γ -butyrolactone (GBL, Sigma-Aldrich), which was spin coated on a pre-cleaned cover glasses, followed by soft bake at 50 °C for 40 min and 95 °C for 2 min, respectively. The film was exposed to a diode-pumped Nd:YVO₄ laser ($\lambda = 532$ nm, Verdi-6, Coherent) with 1.0 W laser input for 0.25 s to 1.1 s each time, and was rotated 90° after each exposure using a motorized rotation stage (PRM1-Z7E, Thorlabs). After exposure, the film was post-exposure baked (PEB) at 50 °C for 20 min to crosslink the exposed regions, followed by development in propylene glycol monomethyl ether acetate (PGMEA, Sigma-Aldrich) or GBL for 1 h. Before drying in CO₂ supercritical point dryer (SAMDRI®-PVT-3D, Tousimis®), the wet samples were rinsed in isoamyl acetate (IA, Sigma - Aldrich) for 1h or in ethanol (Fisher Scientific) overnight.

2.2.2 Surface hydrophobization

Diamond structures were treated by oxygen plasma (Harrick Plasma Cleaner PDC-001) for 15 min to generate hydroxyl groups on surface, followed by vapor deposition of (tridecafluoro-1,1,2,2-tetrahydrooctyl) trichlorosilane (fluorosilane, 0.1 mL, Gelest. Inc) in a vacuum desiccator for 1 h.

2.2.3 Dye adsorption

2.2.3.1 Hydrophilic surfaces

Samples with various surface roughness were treated with oxygen plasma for 15 min, then soaked in 0.005wt% rhodamine B (Sigma Aldrich) aqueous solution for 30 min and air dried. Then these two samples were placed into separate cuvettes containing of 3.5 mL DI water to release the absorbed dye, which was monitored by UV-vis-NIR Spectrophotometer (Varian Cary 5000).

2.2.3.2 Hydrophobic surfaces

Oxygen plasma treated samples were passivated with fluorosilane, followed by soaking in 0.005wt% rhodamine B ethanol solution for 5 min.

2.2.4 Characterization

SEM images were taken from FEI Strata DB235 Focused Ion Beam (FIB) system and the cross-sectional images were taken from samples milled by the Gallium ion beam. The reflection and transmission spectra were acquired by FT-IR spectrometer (Nicolet 8700, equipped with Nicolet continuum infrared microscope) in the [001] direction at the same location of the sample. The reflection spectra were measured using an Au mirror as reference. The aperture size was $60\ \mu\text{m} \times 60\ \mu\text{m}$. Static water contact angles were measured by ramé-hart standard automated goniometer (Model 200). The static contact angle was measured from a $3.0\ \mu\text{L}$ water droplet averaged over three different spots on each sample.

2.3 Results and discussion

2.3.1 3D microfabrication and formation of nano-roughness on 3D structures.

The diamond photonic crystal (see Figure 2.1a) was fabricated by holographic

lithography (HL) using dual-beam quadruple exposure method described before.^[29] The fabrication steps involved spin-coating, pre-exposure bake, exposure, post-exposure bake (PEB), development, solvent rinsing and critical-point drying (CPD). In our study, we used epoxy functionalized cyclohexyl polyhedral oligomeric silsesquioxane (epoxy-POSS) as the negative-tone photoresist (Figure 1d), which crosslinked in the light exposed regions after PEB.^[30] The film was then immersed in a developer to remove the uncrosslinked and lightly crosslinked regions, leaving a 3D microporous structure. The microporosity is determined by the solvency of the developer and the crosslinking density of the exposed regions. Organic solvents, including PGMEA and GBL have been widely used as developers for negative-tone epoxy resists. However, they are not very miscible with liquid CO₂ in the CPD process, which is commonly used to prevent pattern collapse of highly porous 3D microstructures. Therefore, the freshly developed samples were transferred to a liquid CO₂ compatible solvent, IA or ethanol, as the rinsing solvent before CPD.

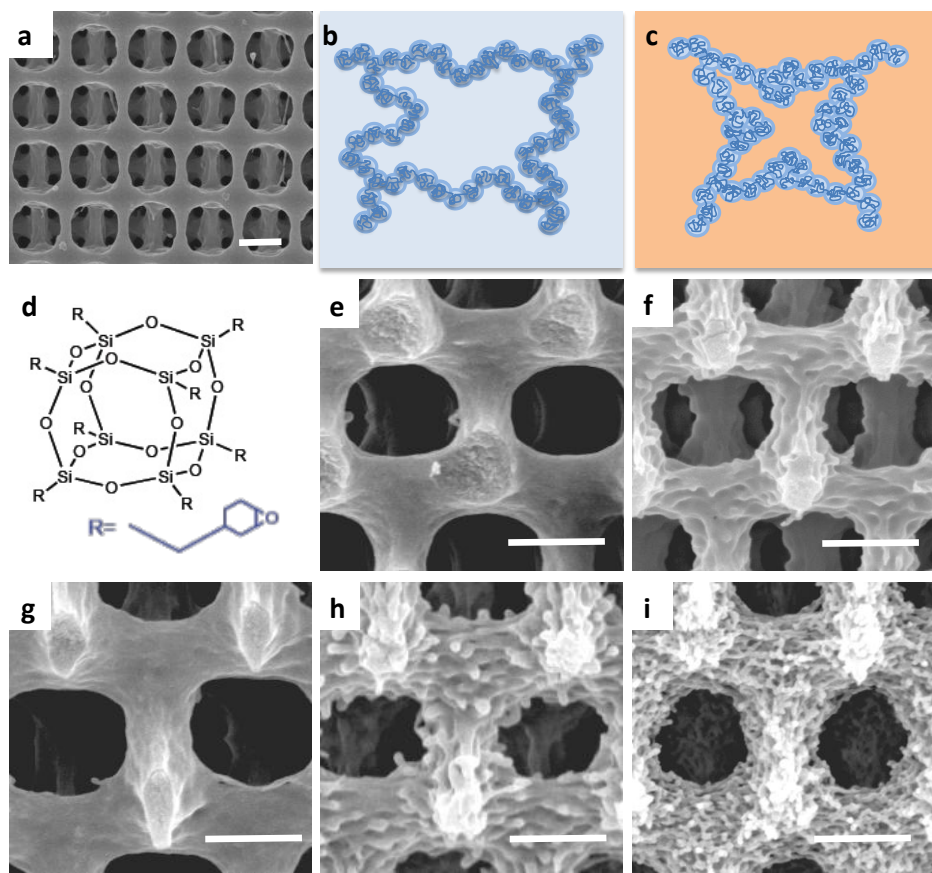


Figure 2.1 Diamond photonic crystals of variable degrees of nano-roughness from epoxy-POSS. (a) Top-view SEM image. (b-c) Schematics of photoresist chains swollen in a good solvent (b) or collapsed in a nonsolvent (c) within a mesh. (d) Chemical structure of epoxy-POSS. (e-f) Cross-sectional SEM images of the diamond structures developed in PGMEA and rinsed in (e) IA and (f) ethanol, respectively, followed by critical point drying in the same solvent. (g-h) Cross-sectional SEM images of the diamond structures developed in GBL and rinsed in (g) IA and (h) ethanol, respectively, followed by critical point drying in the same solvent. (i) Cross-sectional SEM image of the diamond structure developed in GBL, rinsed in DI water and dried in air. Scale bar: 2µm.

A closer look of the samples showed that while the surface of the diamond crystals rinsed in IA were generally smooth regardless of the developer (see Figure 2.1e and 2.1g), those rinsed in ethanol had spongy nano-roughness appeared on the skeletons (Figure 2.1f and 2.1h). The nano-roughness size ranged from 40- 120 nm as measured by AFM (see Figure 2.2 and Table 2.1). The highest degree of porosity, although the nano-feature

size appeared smaller, was observed when the 3D structure was developed in GBL, followed by rinsing in water and dried in air (Figure 2.1i). The relationship between the degree of nano-roughness and the combination of developer and rinsing solvent was summarized in Table 2.1.

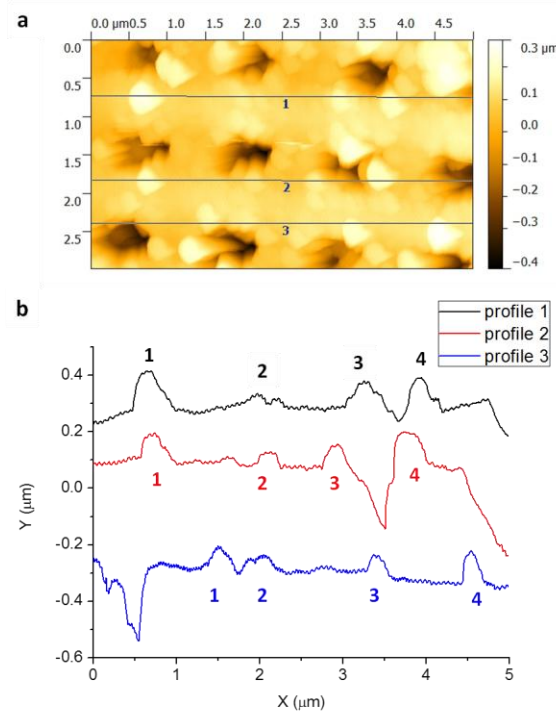


Figure 2.2 AFM characterization of the surface topography of diamond structures developed in GBL, followed by rinsing in ethanol and CPD. a). Height profile of the rough sample, same as sample in Figure 2.1 h. b). Line profile analysis of Figure a. The height and width of the surface features are measured from the three line profiles. Note that there was 300 nm offset in Y scale between each lines for the purpose of illustration. The large valleys in the profiles (> 200 nm) were attributed to 3D microstructure.

Table 2.1 Summary of the heights of surface nano-features measured from line profile analysis in Figure 2.2.

	Height of surface bumps (nm)			
	1 st	2 nd	3 rd	4 th
Profile 1	120	40	100	110
Profile 2	80	50	70	100

Profile 3	60	50	60	100
Roughness range	40-120			
Average roughness size	78 \pm 3			

Table 2.2 Summary of observed surface roughness on 3D diamond structures from different solvents used in development, rinsing and critical point drying process.

Developer	Rinsing solvent	Critical point drying	Observed surface roughness	Corresponding SEM image in Figure 2.1
PGMEA	IA	Yes	Smooth	(e)
PGMEA	Ethanol	Yes	Rough	(f)
GBL	IA	Yes	Smooth	(g)
GBL	Ethanol	Yes	Rough	(h)
GBL	Water	No	Very rough	(i)

2.3.2 Mechanism of nano-roughness formation

These results clearly indicate that the processing conditions, specifically, the rinsing solvent, plays an important role to the nano-morphology appeared on the 3D microstructures. It is expected that in a good solvent, polymer chains swell with an extended chain conformation (see schematics in Figure 2.1b) but phase separate in a nonsolvent. If polymer chains are crosslinked, the mesh size, which is proportional to the molecular weight between crosslink points, M_c , that determines the network swellability or phase separation domain size in a nonsolvent. At a given crosslinking density, the M_c is fixed. Thus, in a nonsolvent the polymer chain segments between crosslink points can only locally aggregate within a mesh to minimize the interaction with the nonsolvent (Figure 2.1c), leading to the formation of nanoporous structures instead of collapsing the whole network. We believe that this explains why the 3D microstructure is maintained

even at a very high degree of nanoporosity when rinsed in water and dried in air. Previously, similar strategies have been reported to create highly porous superhydrophobic coatings, for example, by evaporation a hot solution of isotactic polypropylene dissolved a mixture of good solvent and nonsolvent,^[31] and by freezing electrospun polymer fibers in a liquid nitrogen bath, inducing a phase separation between the polymer and the solvent.^[32]

In our system, the epoxy-POSS is soluble in both PGMEA and GBL. Therefore, the rinsing solvent should be mainly responsible for the appearance of nano-roughness on 3D microstructure. When the swollen polymer network after development was transferred to a good solvent, such as IA, for rinsing, polymer chains maintained their extended chain conformation, resulting in smooth surface after CPD. In contrast, if the rising solvent was a nonsolvent, such as ethanol or water, the swollen polymer chains rapidly microphase separated from the nonsolvent. From nano-roughness data (see Figure 2.1h vs. 2.1i), it is clear that water is a much poorer solvent than ethanol.

To support our reasoning on the solvency effect, we estimated the polymer-solvent interactions using the Hansen solubility parameters^[33] (see Table 2.3). The Flory-Huggins polymer-solvent interaction parameter (χ) can be expressed as,

$$\chi = \frac{V(\delta_1 - \delta_2)^2}{RT} \quad (2.1)$$

where V is the molar volume of the solvent, δ is the solubility parameter, R is the gas constant, T is the absolute temperature. The difference between the two solubility parameters can be further written as

$$(\delta_1 - \delta_2)^2 = (\delta_{d2} - \delta_{d1})^2 + (\delta_{p2} - \delta_{p1})^2 + (\delta_{h2} - \delta_{h1})^2 \quad (2.2)$$

where δ_d is the energy from dispersion bonds between molecules, δ_p is the energy from polar bonds between molecules, and δ_h is the energy from hydrogen bonds between molecules. The larger the value of $(\delta_1 - \delta_2)^2$, the less compatible between the polymer and solvent. The epoxy POSS is an organic-inorganic hybrid material. Here we calculated the solubility parameter from the organic component of the epoxy POSS, which is mainly responsible to the interaction with an organic solvent, to approximate the whole molecule using group contribution method.^[34]

Table 2.3 Hansen solubility parameters of epoxy-POSS and different organic solvents.^a

	δ_d (MPa ^{1/2})	δ_p (MPa ^{1/2})	δ_h (MPa ^{1/2})	δ (MPa ^{1/2})
Epoxy-POSS ^[a]	17.7	-	-	19.2
PGMEA	15.6	5.6	9.8	19.3
GBL	19.0	16.6	7.4	26.2
IA	15.3	3.1	7.0	17.2
Ethanol	15.8	8.8	19.4	26.6
Water	15.5	16.0	42.4	47.9

^a Solubility parameters of solvents were obtained from Reference [33], that of epoxy-POSS was calculated from the organic component to approximate the whole molecule using group contribution method ^[34].

As seen in Table 2.3, PGMEA (19.3 MPa^{1/2}) and IA (17.2 MPa^{1/2}) have similar solubility parameters as that of the epoxy-POSS (19.2 MPa^{1/2}), while GBL (26.2 MPa^{1/2}) and ethanol (26.6 MPa^{1/2}) have much larger solubility parameters, suggesting that GBL and ethanol are relatively poor solvents of epoxy-POSS. However, in experiments we observed that GBL could dissolve the epoxy-POSS rather well. We note that the δ_h value, the energy term from hydrogen bonding, of GBL is much smaller than that of ethanol, 7.4 vs. 19.4 MPa^{1/2}, but close to that of PGMEA and ethanol, which may contribute to the affinity of epoxy POSS in GBL. Nevertheless, GBL was not as good solvent as PGMEA.

Further supporting this is the observed larger nano-roughness from the sample developed in GBL (Figure 2.1h) vs. PGMEA (Figure 2.1f) using the same rinsing solvent, ethanol. As for water, the solubility parameter ($47.9 \text{ MPa}^{1/2}$) is far larger than that of the epoxy-POSS, making it a very poor solvent, in agreement with the observed highest degree of nanoporosity in 3D skeletons. Further supporting the solvency effect is that when we re-soaked the rough samples (see Figure 2.1f and 2.1h) in the respective developer, PGMEA or GBL, overnight, followed by CPD drying, the rough surface became smooth, presumably that the collapsed chains were restored within the crosslinked network.

Since surface roughness is the result of chain collapse between crosslinks, the crosslinking density of the polymer network should also influence the degree of roughness. As seen in Figure 2.3, when increasing the photoacid generator concentration, [PAG], and exposure time, the surface of the diamond structures became smoother. This again can be explained by the polymer chain morphology between crosslinks. As [PAG] increases or exposure time increases, the number of photoacids generated is increased, thus, the crosslinking density is increased and the M_c or mesh size is decreased (see Figure 2.3a and 2.3b). In a nonsolvent, the available chain segments for collapsing out of solvent are dramatically decreased. When the crosslinking density was sufficiently high, the surface of the 3D microstructure became smooth (Figure 2.3f).

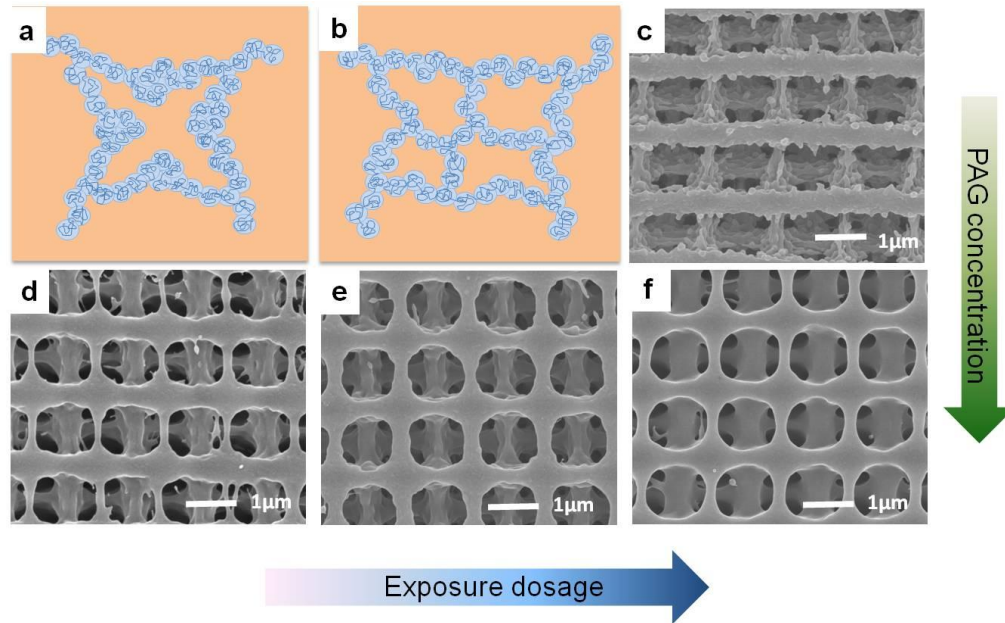


Figure 2.3 Surface roughness on epoxy-POSS diamond structures as a function of chain crosslinking density. The samples were developed in GBL and rinsed in ethanol, followed by critical point drying. (a-b) Schematics of the collapsed polymer chains in a poor solvent at a low (a) and high (b) crosslinked density. (c) Photoacid generator concentration [PAG] = 0.3 wt%, exposure time of 0.6s. (d-f) [PAG] = 1.0 wt%, exposure time: (d) 0.25s, (e) 0.30, and (f) 0.35s.

2.3.3 Photonic band gap properties

Because the nano-roughness generated here (≤ 120 nm) is much smaller than the wavelength of light and the lattice constant of the diamond structure (~ 2 μm), the angle-dependent structural color and the photonic bandgap position in the infrared region are not strongly affected by the introduction of nano-roughness (Figure 2.4). As shown in the FTIR reflection and transmission spectra (Figure 2.4b), both the smooth and rough diamond crystals have the same reflection peak at ~ 2.1 μm , which is from the first partial bandgap in the [001] direction of the diamond photonic crystal.^[29] This is reasonable since the photonic bandgap position and width is determined mainly by the microscopic structure, including structural symmetry, lattice period, volume filling fraction, refractive

index contrast between the high and low index materials, most of which remain the same except the small change in volume filling fraction. We note that the reflectivity, however, does decrease when the nano-roughness is increased.

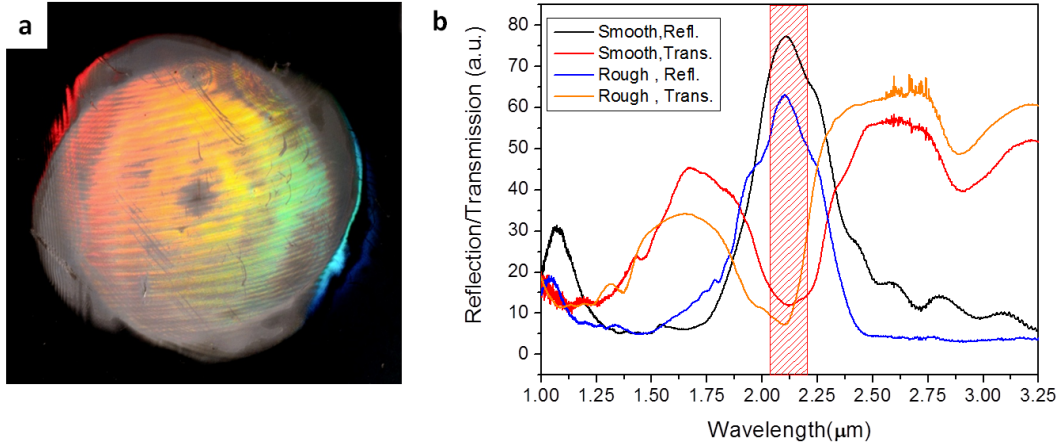


Figure 2.4 (a) Structural color observed from epoxy-POSS diamond structure (1 cm diameter) with nano-roughness. The film was developed in GBL, rinsed and critical point dried in ethanol. (b) FTIR reflection and transmission spectra of diamond structures with smooth (developed in PGMEA, rinsed and dried in IA) and rough (developed in GBL, rinsed and dried in ethanol) surfaces. The shaded area represents the calculated PBGs.

2.3.4 Tunable wetting behaviors

It is known that surface roughness amplifies hydrophilicity (if the Young's contact angle, θ is less than 90°) or hydrophobicity (if θ is greater than 90°),^[35] as manifested in many natural surfaces.^[16-18] When the diamond structure was treated with oxygen plasma, thus, generating hydroxyl groups on the surface, it became superhydrophilic, with an apparent static water contact angle, θ_{stat} , smaller than 10° , regardless of the surface roughness. After vapor deposition of a thin layer of low surface energy material, tridecafluoro-1,1,2,2-tetrahydrooctyl) trichlorosilane (fluorosilane), on the sample, the structure became highly hydrophobic to superhydrophobic depending on the degree of

nano-roughness (Figure 2.5). θ_{stat} was $\sim 120^\circ$ - 130° on a smooth diamond structure, decreasing with increasing exposure dosage (Figure 2.5a-d). On a rough structure, θ_{stat} was typically 140° or higher (Figure 2.5e-h). Highly mobile, superhydrophobic surface (Figure 2.5e), where the water droplet easily rolled off, was achieved from the samples patterned at the lowest exposure time (0.7 s), developed in GBL and rinsed by ethanol. Although higher porosity and roughness, thus, superhydrophobicity could be obtained by rinsing the samples in water, water is not compatible with CPD process. 3D structures in samples that are water rinsed and air-dried tend to collapse. Therefore, we did not use those samples for systematic wetting studies.

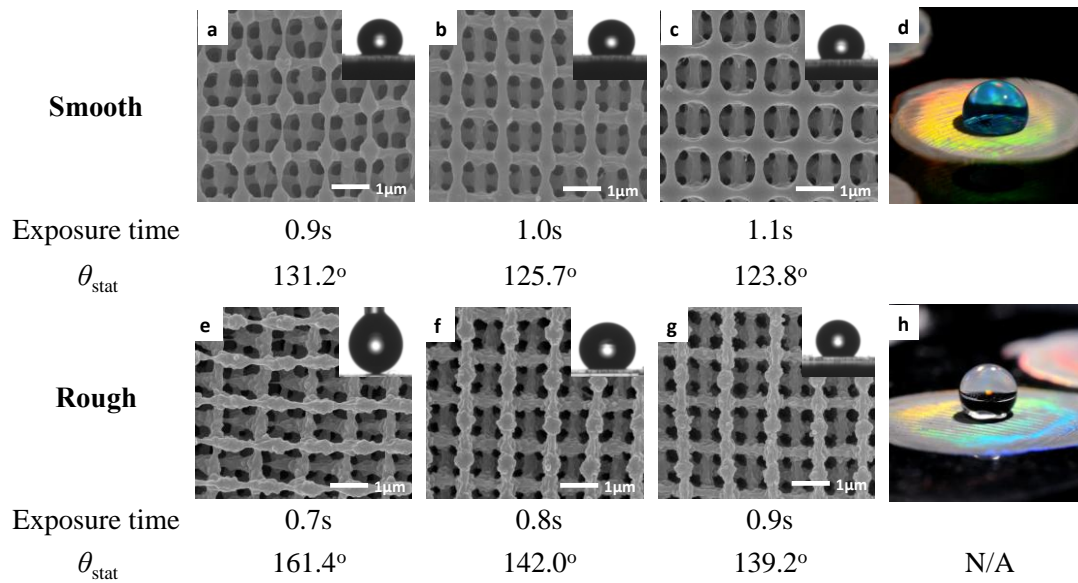


Figure 2.5 Wetting behaviors of fluorosilane treated epoxy-POSS diamond structures. (a-c) Samples with smooth surfaces. (e-g) Samples with rough surfaces. Inset: static water contact angles. (d) Photo of a water droplet on sample (c). (h) Photo of a water droplet on sample (e). The smooth samples (a-d) were developed in PGMEA, rinsed in IA for 1 h, and critical-point dried. The rough samples (e-h) were developed in GBL, rinsed in ethanol overnight, and critical-point dried. All samples were then treated with oxygen plasma for 15 min, followed by fluorosilane vapor deposition.

Porous structures are not new; they have been prepared by many methods to achieve

superhydrophobicity.^[36] Here we demonstrate combined structural color and self-cleaning property, mimicking the multi-functions of butterfly wings, through introduction of random nanoporosity on diamond photonic structures simply by varying the solvents used in 3D microfabrication steps.

2.3.5 Enhanced small molecule adsorption

Another distinct advantage from the dual-scale porous photonic crystal is the enlarged surface area, which is attractive to enhance adsorption and release of dye molecules, nanoparticles, quantum dots, drugs, and proteins. In DSSCs and quantum dots solar cells (QDSCs), the efficiency of electron transport is highly dependent on the dye or QD adsorption on the electrode. Meanwhile, microstructures with minimal-surface interfacial morphologies, such as the triply periodic bicontinuous structures that can be fabricated by HL, have been suggested to offer enhance thermal and electrical transport.^[37] Moon *et al.* recently have created hierarchically porous TiO₂ electrodes templated from HL patterned microscopic structures.^[13] Their results suggest that synergistic effects of strong scattering from the surface of photonic structure and long charge recombination time lead to the efficiency of the solar cell comparable to that of traditional DSSC.

Previously, we^[38-39] and others^[40] have created TiO₂ 3D photonic crystals using silica templates fabricated by HL and colloidal crystals, respectively. We also shown that epoxy-POSS 3D photonic crystals can be converted to silica photonic crystals.^[41] Therefore, it is possible to create TiO₂ electrodes with large surface area for DSSCs using the above fabricated epoxy-POSS diamond structures. We note that change of porosity of the 3D microstructure will also affect the surface area. Here, we focus on the effect of

nanoroughness in dye adsorption and release. We fabricated the diamond photonic crystals with both smooth and rough surfaces under the same lithographic conditions but using different developing and rinsing solvents for adsorption of rhodamine B dyes. After oxygen plasma treatment, the samples were soaked in a rhodamine B aqueous solution for 30 min, followed by air-drying. SEM images (data not shown) revealed that the dye was uniformly and conformally coated on the 3D structure. As seen in the inset of Figure 2.6, the rough sample has a much deeper magenta color compared to the light pink color from the smooth one. To quantify the dye absorption on the photonic crystals, we monitored dye release in water using UV-vis-NIR spectrophotometer. The dye absorbance peak at 554 nm as a function of time is shown in Figure 2.6a. It took ~ 300 min to release all the dyes absorbed on the smooth sample vs. ~ 600 min from the rough one. More importantly, the total dye released from the rough sample was more than 6 times of that from the smooth one.

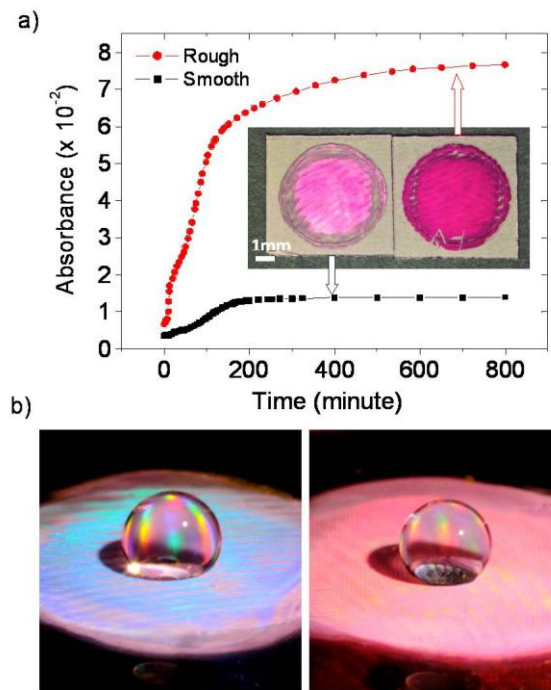


Figure 2.6 Comparison of rhodamine B adsorption on smooth and rough diamond structures. The smooth samples were developed in PGMEA, rinsed in IA for 1 h, and critical-point dried. The rough samples were developed in GBL, rinsed in ethanol overnight, and critical-point dried. (a) Absorbance of dye released from the diamond structures in water at 554 nm over time. The samples were treated with oxygen plasma for 15 min, followed by soaking in rhodamine B aqueous solutions for 30 min. Inset: optical images of dye adsorbed films from rhodamine B aqueous solution. (b) Optical images of water droplets sitting on fluorosilane treated diamond structures followed by adsorption of rhodamine B ethanol solution for 5 min. Left, smooth surface. Right, rough surface.

Lastly, we show that it is possible to combine the high dye adsorption and superhydrophobicity on the surface of the diamond photonic crystal. In this regard, we immersed the fluorosilane treated samples (both smooth and rough) in a dye/ethanol solution. Ethanol is chosen here because it has a lower surface tension (22.1 mN m^{-1}) compared to that of water, 72.8 mN m^{-1} at room temperature. Therefore, ethanol can wet the photonic crystal surface even when it repels water. As seen in Figure 2.6b, the wettability of the photonic crystals was not affected by the dye adsorption: the rough sample with a high degree of dye adsorption remained superhydrophobic. However, in contrast to angle-dependent, highly reflected structural color from the crystal with smooth surface, the rough sample in magenta color appeared rather dull. The combined action of light reflection and light adsorption is similar to the observation in various species of *Morpho* butterflies,^[5] where the pigment at the bottom of the butterfly scale provides change of hue of the structural color without varying the microstructure.

2.4 Conclusions

In summary, we have created 3D diamond photonic crystals with controllable nano-roughness by exploiting microphase separation of the swollen, crosslinked polymer chains from a nonsolvent during the rinsing step in the holographic lithography process.

The degree of roughness can be tuned by varying the crosslinking density of the polymer network and the solvent affinity to the polymer chains. The dual-scale roughness (periodic microstructure and nanopores) offers new opportunities previously unstudied, that is to combine actions on a 3D photonic crystal, including light interference, light absorption and self-cleaning without cross-talk. Further, we demonstrate ~ 6 times of dye adsorption enhancement on rough diamond crystals compared to those with smooth surface. We believe that 3D photonic structure with controllable nano-roughness will open the door for many other applications, such as DSSCs and QDSCs, fuel cells, catalysis, and protein/drug delivery.

2.5 Reference

- [1] M. Srinivasarao, *Chem. Rev.* **1999**, *99*, 1935.
- [2] A. R. Parker, *J. Opt. A* **2000**, *2*, R15.
- [3] A. R. Parker; V. L. Welch; D. Driver; N. Martini, *Nature* **2003**, *426*, 786.
- [4] P. Vukusic; J. R. Sambles, *Nature* **2003**, *424*, 852.
- [5] S. Kinoshita; S. Yoshioka, *ChemPhysChem* **2005**, *6*, 1442.
- [6] F. Marlow; Muldarisnur; P. Sharifi; R. Brinkmann; C. Mendive, *Angew. Chem. Int. Ed.* **2009**, *48*, 6212.
- [7] E. Yablonovitch, *Phys. Rev. Lett.* **1987**, *58*, 2059.
- [8] S. John, *Phys. Rev. Lett.* **1987**, *58*, 2486.
- [9] S. X. Yang; J. H. Page; Z. Y. Liu; M. L. Cowan; C. T. Chan; P. Sheng, *Phys. Rev. Lett.* **2004**, *93*.
- [10] T. Gorishnyy; C. K. Ullal; M. Maldovan; G. Fytas; E. L. Thomas, *Phys. Rev. Lett.*

2005, 94, 4.

- [11] W. M. Jin; J. H. Shin; C. Y. Cho; J. H. Kang; J. H. Park; J. H. Moon, *ACS Appl. Mater. Interfaces* **2010**, 2, 2970.
- [12] E. S. Kwak; W. Lee; N. G. Park; J. Kim; H. Lee, *Adv. Funct. Mater.* **2009**, 19, 1093.
- [13] C. Y. Cho; J. H. Moon, *Adv. Mater.* **2011**, 23, 2971.
- [14] K. Keizer; H. Verweij, *Chemtech* **1996**, 26, 37.
- [15] Z. Z. Gu; H. Uetsuka; K. Takahashi; R. Nakajima; H. Onishi; A. Fujishima; O. Sato, *Angew. Chem. Int. Ed.* **2003**, 42, 894.
- [16] W. Barthlott; C. Neinhuis, *Planta* **1997**, 202, 1.
- [17] K. Autumn; Y. A. Liang; S. T. Hsieh; W. Zesch; W. P. Chan; T. W. Kenny; R. Fearing; R. J. Full, *Nature* **2000**, 405, 681.
- [18] X. F. Gao; L. Jiang, *Nature* **2004**, 432, 36.
- [19] T. Onda; S. Shibuichi; N. Satoh; K. Tsujii, *Langmuir* **1996**, 12, 2125.
- [20] D. Öner; T. J. McCarthy, *Langmuir* **2000**, 16, 7777.
- [21] L. C. Gao; T. J. McCarthy, *Langmuir* **2006**, 22, 2966.
- [22] H. E. Jeong; S. H. Lee; J. K. Kim; K. Y. Suh, *Langmuir* **2006**, 22, 1640.
- [23] R. G. Karunakaran; C. H. Lu; Z. H. Zhang; S. Yang, *Langmuir* **2011**, 27, 4594.
- [24] T. Lebeau; J. M. Robert, *Appl. Microbiol. Biotechnol.* **2003**, 60, 624.
- [25] Z. H. Bao; M. R. Weatherspoon; S. Shian; Y. Cai; P. D. Graham; S. M. Allan; G. Ahmad; M. B. Dickerson; B. C. Church; Z. T. Kang; H. W. Abernathy Iii; C. J. Summers; M. L. Liu; K. H. Sandhage, *Nature* **2007**, 446, 172.
- [26] A. Setaro; S. Lettieri; P. Maddalena; L. De Stefano, *Appl. Phys. Lett.* **2007**, 91,

051921.

[27] S. K. Lee; H. S. Park; G. R. Yi; J. H. Moon; S. M. Yang, *Angew. Chem. Int. Ed.* **2009**, *48*, 7000.

[28] H. E. Townley; K. L. Woon; F. P. Payne; H. White-Cooper; A. R. Parker, *Nanotechnology* **2007**, *18*.

[29] G. Q. Liang; X. L. Zhu; Y. G. Xu; J. Li; S. Yang, *Adv. Mater.* **2010**, *22*, 4524.

[30] J. H. Moon; J. S. Seo; Y. G. Xu; S. Yang, *J. Mater. Chem.* **2009**, *19*, 4687.

[31] H. Y. Erbil; A. L. Demirel; Y. Avcı; O. Mert, *Science* **2003**, *299*, 1377.

[32] J. T. McCann; M. Marquez; Y. Xia, *J. Am. Chem. Soc.* **2006**, *128*, 1436.

[33] C. M. Hansen, *Hansen Solubility Parameters: A User's Handbook*. CRC Press: Boca Raton, FL, **2000**.

[34] D.W. van Krevelen; P.H. Hoftyzer, *Properties of Polymers. Correlations with Chemical Structures*. Elsevier: New York, **1972**.

[35] R. N. Wenzel, *Ind. Eng. Chem.* **1936**, *28*, 988.

[36] X. Chen; L. H. Wang; Y. Q. Wen; Y. Q. Zhang; J. X. Wang; Y. L. Song; L. Jiang; D. B. Zhu, *J. Mater. Chem.* **2008**, *18*, 2262.

[37] H. Y. Chen; Y. Kwon; K. Thornton, *Scr. Mater.* **2009**, *61*, 52.

[38] J. H. Moon; Y. G. Xu; Y. P. Dan; S. M. Yang; A. T. Johnson; S. Yang, *Adv. Mater.* **2007**, *19*, 1510.

[39] Y. Xu; X. Zhu; Y. Dan; J. H. Moon; V. W. Chen; A. T. Johnson; J. W. Perry; S. Yang, *Chem. Mat.* **2008**, *20*, 1816.

[40] B. Hatton; L. Mishchenko; S. Davis; K. H. Sandhage; J. Aizenberg, *Proc. Natl. Acad. Sci. U. S. A.* **2010**, *107*, 10354.

[41] Y. A. Xu; X. L. Zhu; S. Yang, *ACS Nano* **2009**, *3*, 3251.

Chapter 3

Switching Periodic Membranes via Pattern Transformation and Shape Memory Effect

3.1 Introduction

Shape memory polymers (SMPs) are polymeric smart materials of interest for a variety of applications, including deployable space structures, artificial muscles, biomedical devices, sensors, smart dry adhesives, and fasteners.^[1-2] They form a “permanent” shape by chemical or physical crosslinking (e.g. crystallization or chain entanglement). Above a thermal phase transition temperature, either a glass transition temperature (T_g) or a melting temperature (T_m), SMPs can be deformed to different temporary shapes, which can be fixed by cooling the sample. Upon exposure to an external stimulus, such as heat, light, and solvent, the temporary shapes can return to their original (or the permanent) shape. There has been much effort to develop new chemistry for improved shape fixity and shape recovery efficiency, responsiveness to new environmental triggers, achieving multi-shape memory effect, and applications to biomedical devices.^[1, 3-9] Nevertheless, most of the study focuses on shape memory effect in bulk SMPs. A few groups have created micropatterns in SMPs, such as microprotrusions^[10] and microwrinkles^[8, 11] by taking advantage of the large modulus change near the phase transition temperature. None of them, however, have reported the recovery to the original shape from the micropatterns. During the shape recovery process, the entropic energy stored in the deformed state is released. It remains to be seen whether the deformed shape can be completely recovered as surface energy becomes increasingly dominant when the size shrinks to micro- and nanoscale.

Recently, we and several other groups have demonstrated pattern transformation in elastic membranes with periodic hole arrays by mechanical compression,^[12-13] solvent swelling,^[14-15] polymerization,^[16] and capillary force.^[17] For example, when swollen by an organic solvent, a poly(dimethylsiloxane) (PDMS) membrane consisting of micron-sized circular holes in a square array buckles to a diamond plate pattern of elliptic slits with the neighboring units perpendicular to each other.^[14] As a result, the physical properties (e.g. photonic^{18, 19} and phononic^[15] band gap^[18-19] and mechanical behaviors^[20-21]) could be significantly altered due to change of lattice symmetry, pore size, shape and volume filling fraction. One question rises whether it is possible to switch a colorful film to transparent one via pattern transformation. The latter state will allow for seeing through or mingling with the surroundings. Therefore, the dramatic visual contrast between colored and transparent states is of interest for applications such as display, privacy window, and camouflage. In nature, invisibility is an important strategy for many sea creatures to hide from predators in water. For example, bobtail squids are invisible in sand during the day with chromatophores in the skin concentrated into small, barely visible dots; when the muscle fibers stretch out the skin, thereby enlarging the chromatophores, the color becomes visible for signaling or escape from predators.^[22]

Here we report switching a SMP membrane with diffraction color to a transparent film via harnessing the mechanical instability and shape memory effect. When hot-pressed, the SMP membrane consisting of a hexagonal array of circular holes (1.2 μm in diameter, 2.5 μm in pitch, and 5.0 μm in depth) underwent pattern transformation to an array of elliptical slits to featureless on surface with increasing applied strain, leading to the dramatic change of the hole size and shape, and diffraction color, which could be

fixed at room temperature, and later recovered to the original pattern (and color) upon reheating. Using continuum mechanical analyses, we modeled, for the first time, an out-of-plane compression of SMP membrane. We observed the hot-press induced deformation and pattern transformation of the membrane at different strains, the structure fixation at the cooling step, and the complete recovery of the microstructure, in agreement with experiments. We also find that the elastic energy stored in the membrane is roughly 2-orders of magnitude larger than the surface energy, leading to autonomous recovery of the structural color upon reheating. Further, we demonstrated two possible applications of color and transparency change in our SMP periodic membranes, including 1) temporary erasing the pre-fabricated "Penn" logo in the film, and 2) a temporary display of "Penn" logo by hot-pressing the film against a stamp.

3.2 Experimental methods

Unless specifically noted, all chemicals were obtained from Sigma-Aldrich (St. Louis, MO, USA) and used as received.

3.2.1 Fabrication of the hexagonal pillar array

The SMP periodic membrane was replica molded from a 2D hexagonal pillar array (1.2 μm in diameter, 2.5 μm in pitch, and 5 μm in height), which was fabricated by 3-beam holographic lithography (HL)^[23-24] from epoxycyclohexyl POSS® cage mixture (EP0408, Hybrid Plastics®) (epoxy POSS) mixed with 0.9 wt % photoinitiator, Irgacure 261 (Ciba Specialty Chemicals). In a typical HL experiment, the epoxy POSS photoresist was spin-coated on a glass substrate, prebaked at 50 °C for 40 min, followed by 95 °C for 2 min. The film was then exposed to three interfering laser beams ($\lambda = 532$ nm, power of beam source ~ 1.0 W), followed by post-exposure bake (PEB) at 50 °C for 30 s (Figure

3.1a). The pillar structures were obtained after development in propylene glycol methyl ether acetate (PGMEA), rinsing in isopropanol (IPA), followed by drying in critical point dryer (SAMDRI[®]-PVT-3D, tousimis) from ethanol to prevent pillar collapse. The sample area was defined by the laser beam size, typically ~1 cm in diameter. By varying the dosage of laser exposure and the PEB time and temperature, we obtained holes size ranging from hundreds of nanometers to a few microns.

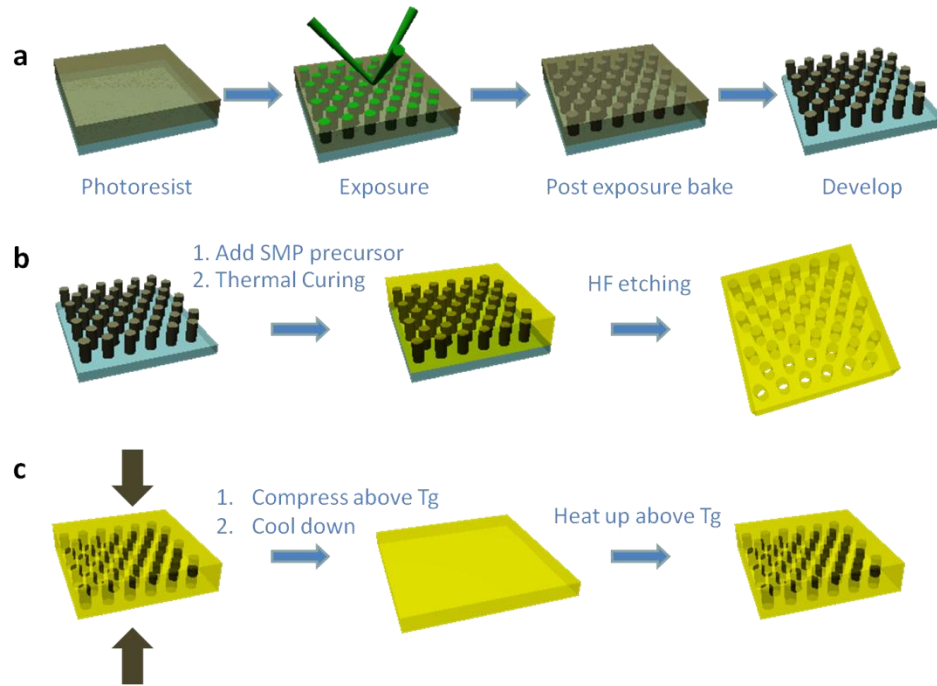


Figure 3.1 Schematic illustration of fabrication and deformation/recovery of a 2D SMP membrane. (a) Fabrication of 2D pillar array by holographic lithography. (b) Fabrication of SMP membrane with periodic holes by replica molding, followed by etching in HF aqueous solution. (c) Hot-pressing of SMP membrane in the vertical direction above T_g . The temporary shape could be fixed by cooling down to room temperature under the load. The original shape could be recovered upon reheating above T_g .

3.2.2 Replica molding SMP periodic membrane

The SMP precursor, a mixture with molar ratio 5:1:3 of melted diglycidyl ether of bisphenol A epoxy (EPON 826), poly(propylene glycol)bis(2-aminopropyl)ether

(Jaffamine D-230) and decylamine (DA), was infiltrate into the template via capillarity at 50 °C followed by thermal curing at 100 °C for 1.5 h and 150 °C for 1 h, respectively. The T_g can be tuned from 40 °C to 90 °C by varying the ratio of difunctional D230 and monofunctional DA.^[25] Here, the SMP was formulated to have a T_g of 70 °C. After crosslinking EPON 826, the epoxy POSS template and the glass substrate were etched away by aqueous HF solution (48% wt.), resulting in a free-standing SMP membrane of a hexagonal array of holes on a ~500 μm thick bulk film.

3.2.3 Hot pressing of SMP membranes

The SMP membrane was compressed in the vertical direction using a manual bench top heated hydraulic press (CARVER 4122, Carver, Inc). The sample (> 0.4 mm thick) was placed inside of a Teflon sample holder (0.4 mm thick), which was then pressed between two Teflon sheets with heated platens. The platens were pre-heated to 100 °C for 10 min to reach equilibrium. Then a pressure of 1000 psi was applied to the sample and kept for 15 min before cooling down to room temperature, followed by release of the pressure to lock the temporary shape. The strain was calculated by comparing the final film thickness with the original one.

3.2.4 Fabrication of SMP membrane with embedded “Penn” letter

The membrane was fabricated by replica molding in the way similar to that from the hexagonal POSS pillar array. One added step was UV exposure ($\lambda=365$ nm, 400 mJ/cm^2 , 97435 Oriel Flood Exposure Source, Newport) through a “Penn” logo photomask conducted after prebaking and before the three-beam laser exposure. After PEB, the “Penn” region was highly crosslinked and appeared nearly flat or with shallow features depending on the dosage, while the surrounding areas formed pillar structures.

3.2.5 Calculation/modelling

Numerical simulations of stability of the structure were conducted using the nonlinear finite element code ABAQUS/Standard (version 6.8-2) while the thermo-mechanical loading history of the structures was investigated utilizing the nonlinear finite element code ABAQUS/Explicit (version 6.8-2). Each mesh was constructed of 8-node, linear, 3D elements (ABAQUS element type C3D8R). In the hexagonal array the voids have a radius $R = 1 \mu\text{m}$ and a unit cell spanned by the lattice vectors $A_1 = [2 \ 0 \ 0] \mu\text{m}$ and $A_2 = [1 \ 1.732 \ 0] \mu\text{m}$ and $A_3 = [0 \ 0 \ 0.1] \mu\text{m}$ is used. RVE consisting of $1 \times 2 \times 1$ unit cells is considered in the simulations of the thermo-mechanical loading cycle and an imperfection in the form of the most critical eigenmode is introduced into the mesh to capture the instability upon hot-pressing, the subsequent freezing-in of the transformed pattern and then the shape recovery behavior. The stress-strain behavior of the SMP is captured using the material parameters reported in Table 3.1 in Results and discussion section.

3.3 Results and discussion

The ability to simultaneously change the lattice symmetry, pore size and shape, and volume filling fraction through pattern transformation offers an attractive approach to drastically alter the materials properties. Most deformation methods reported so far involves the use of solvent, either through swelling or drying processes. In comparison, application of mechanical force will allow us to independently control the amount, direction (uniaxial or biaxial both in-plane and out-of-plane), and timing of strain applied to the periodic structures. In the case of in-plane compression, however, additional care has to be taken to eliminate the out-of-plane buckling, e.g. by sandwiching the film

between two rigid sheets.^[12] In most applications, a direct out-of-plane compression is easy to implement and desirable, and was thus performed in our experiments.

3.3.1 Color / Transparency Switching in SMP periodic membranes

The SMP periodic membrane (1.2 μm in diameter, 2.5 μm in pitch, and 5 μm in depth) was prepared by replica-molding from a 2D hexagonal pillar array, which was fabricated by 3-beam holographic lithography^[23-24] (see Figure 3.1a-b and details in Experimental section). The negative-tone photoresist, epoxy-cyclohexyl POSS[®] cage mixture (epoxy POSS) was chosen here to fabricate the pillar array since it could be readily removed by hydrofluoric acid (HF) solution at room temperature^[23] after templating the SMP membrane. When the latter was heated to 10-30 $^{\circ}\text{C}$ above its T_g (70 $^{\circ}\text{C}$), it became softened and was compressed vertically by a hot-press to a temporary shape (Figure 3.1c). The load was carefully controlled to deform the membrane at different strain levels, here referring to engineering strain, $\varepsilon = \text{change of film thickness/original thickness}$. The temporary shape was fixed when cooled down to room temperature while keeping the loading force constant. Upon reheating to 90 $^{\circ}\text{C}$, the hexagonal shape was recovered. During the pattern deformation and recovery,^[23] we observed reversible switching of color and transparency.

Although the bulk SMP film is transparent, the SMP membrane is colorful due to the diffraction grating effect (Figure 3.2a, f, k). Because of the Gaussian distribution of the laser beam in holographic lithography and possible small misalignment of optics, there was gradient laser intensity from center to the edge, resulting in pore size distribution and color variation across the sample size. This can be improved using a beam shaper or patterning the film by conventional photolithography through a

photomask. When the applied strain, ε , was $\sim 13 \pm 2\%$, the circular holes of $p6mm$ symmetry were deformed to elliptical slits (width of major axis, $1.25 \mu\text{m}$, minor axis, 500 nm) with $p2gg$ symmetry (Figure 3.2g, l), in agreement with the observation from the swelling-induced instability in SU-8 membranes with a hexagonal array of pores.^[15] When the SMP membrane was compressed in the vertical direction, it expanded in-plane due to positive Poisson's ratio, hence generating an equivalent in-plane compressive stress to the circular holes. The initial diffraction color diminished significantly after compression although it was not completely lost at this strain level (Figure 3. 2b). This could be attributed to the smaller pore size and porosity. The width of the minor axes of the ellipse further decreased, from hundreds of nanometers to a few nanometers, as the strain was increased. When ε was increased to $\sim 20 \pm 2\%$, the holes were almost closed into lines (see Figure 3.2c, h and m) and the SMP membrane became quite transparent, much like the bulk film. At $\varepsilon \sim 30 \pm 2\%$, the holes were closed-up and the surface became nearly featureless (Figure 3.2d, i and n). No further change of transparency was observed. When any of the above deformed SMP membranes were reheated to $90 \text{ }^\circ\text{C}$, the original periodic structure was restored nearly to completion (97.6% of the original hole size), as evident by the SEM images and the regeneration of strong diffraction color (Figure 3.2e, j and o). Surprisingly, even the one with completely closed pores was restored, suggesting that the adhesive energy between the pore surfaces was much smaller than the elastic recovery energy. The different color displayed in Figure 3.2a (the original film) and 3.2e (the recovered one) could be caused by a small misalignment of incident light during photo shooting could lead to appearance of a different color. When ε was greater than 50%, the 2D grating with air holes and its color could no longer be completely recovered due to the

permanent deformation of the polymer network.

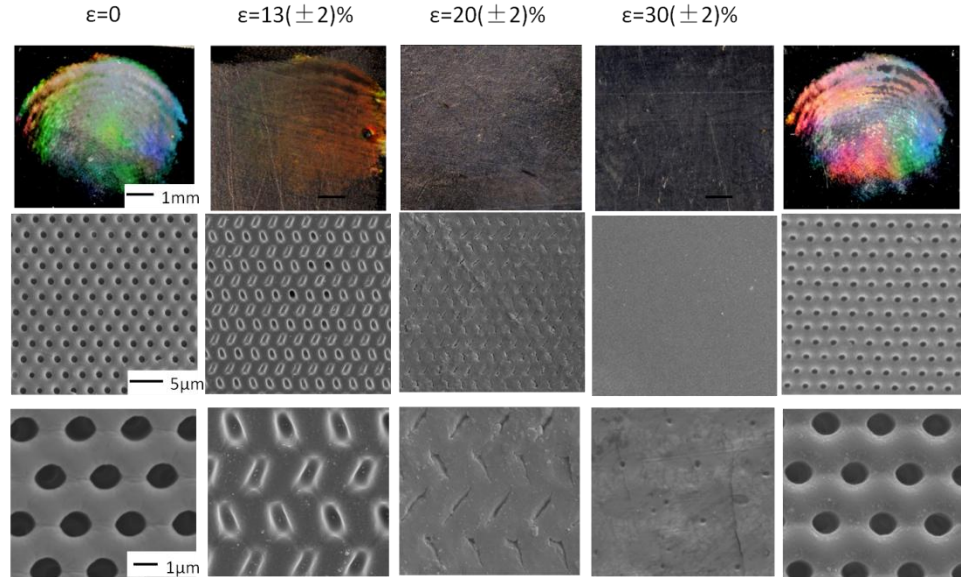


Figure 3.2 Pattern transformation and recovery in a 2D SMP membrane. (a-e) Optical images of the (a) original, (b-c) partially deformed, $\varepsilon \sim 13 \pm 2\%$ (b) and $\varepsilon \sim 20 \pm 2\%$ (c), (d) completely deformed, $\varepsilon \sim 30 \pm 2\%$, and (e) recovered SMP membranes. (f-j) Corresponding SEM images of the SMP membranes shown in (a-e). (k-o) Higher magnification SEM images of (f-j).

The reversible switching between the colorful displays to transparency was repeated successfully for more than 10 cycles with $\varepsilon < 50\%$, and the recovery of diffraction color occurred within a few seconds. According to SEM images, the hole size of the recovered films decreased slightly to 94.4% and 89.7% of the original one after three and ten cycles, respectively. The diffraction color displayed at any of the temporary state could be reprogrammed *on demand* by precise control of the applied strain level and temperature/load of deformation. Hence, it is possible to build a color spectrum by carefully tuning the mechanical deformation. Further, we may achieve full-color display by combining the instability and design of the original microstructures with variable structural parameters.

During the pattern transformation and recovery process, the air holes were squeezed out and restored, respectively, which would result in a dramatic transparency change. As a proof-of-concept, we placed two SMP membranes on a paper printed with “Penn” logos: one was hot-pressed at $\varepsilon \sim 30 \pm 2\%$ (the left one), and the other was the original, non-deformed one (the right one, see illustration in Figure 3.3a). Due to diffraction from the surface of the original membrane with pores in hexagonal array, the “Penn” letters beneath it could not be clearly viewed, in sharp contrast to that beneath the deformed membrane (see Figure 3.3b). The transparency change was further investigated by UV-Vis spectroscopy at different thermal and mechanical treatments (Figure 3.3c) using bulk SMP film as a reference. As expected, the original sample (A) has the lowest transmittance (e.g. 28.1% at $\lambda = 600$ nm). For the hot-pressed samples, sample (B) that was deformed at $\varepsilon \sim 13 \pm 2\%$ shows improved transmittance, 46.9% at 600 nm, and the sample (C), which was deformed at $\varepsilon \sim 30 \pm 2\%$ with closed voids, has the highest transmittance, 88.8% at 600 nm, in comparison with the bulk SMP film. The slightly lowered transparency may be attributed to the surface roughness of the SMP membrane introduced by the Teflon sheets and dust particles trapped on the sample surface during hot-pressing and press release. Finally, the recovered sample (D) shows low transmittance (32.5% at 600 nm), very close to that of the original membrane in the UV-visible region.

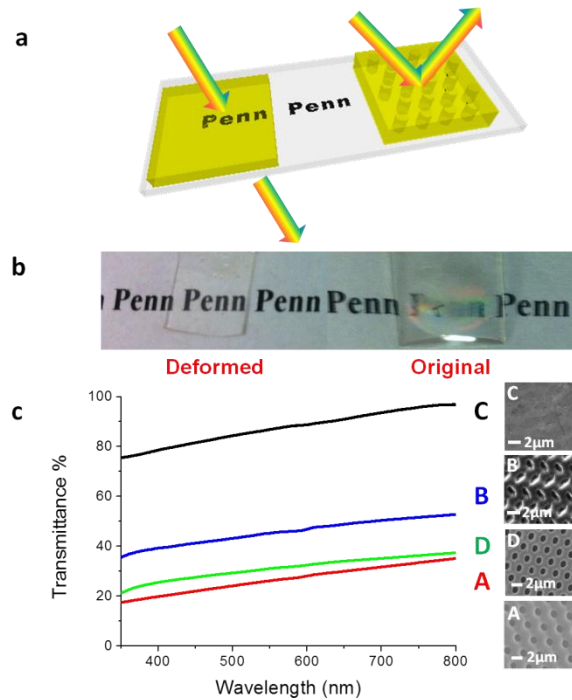


Figure 3.3 Display of “Penn” logos underneath 2D SMP membranes. a. Schematic illustration of transparency comparison between the deformed and the original SMP membranes. b. Optical images of the deformed and original SMP membranes on top of the “Penn” logo. The “Penn” underneath the original membrane is hardly legible but clearly visible in the deformed sample. c. UV-Vis spectra of different 2D SMP membranes (A-D) using bulk SMP film as reference. A. Original. B. Deformed at $\varepsilon \sim 13 \pm 2\%$. C. Deformed at $\varepsilon \sim 30 \pm 2\%$. D. Recovered one.

3.3.2 Finite Element Analysis

Since the deformation results presented here are the first demonstration of instabilities induced by loading in the direction perpendicular to the voids, we built a 3D mechanical model to quantitatively investigate the buckling and post-buckling behaviors. The structure is modeled as an infinite array of infinitely long voids in the x_1 - x_2 plane. 3D analyses are conducted and the constraining effect given by the substrate is accounted for by setting the lateral expansion equal to zero. A periodic representative volume element (RVE), as shown in Figure 3.4a, is considered and a series of constraint equations are

applied to the boundaries of the model providing general periodic boundary conditions.

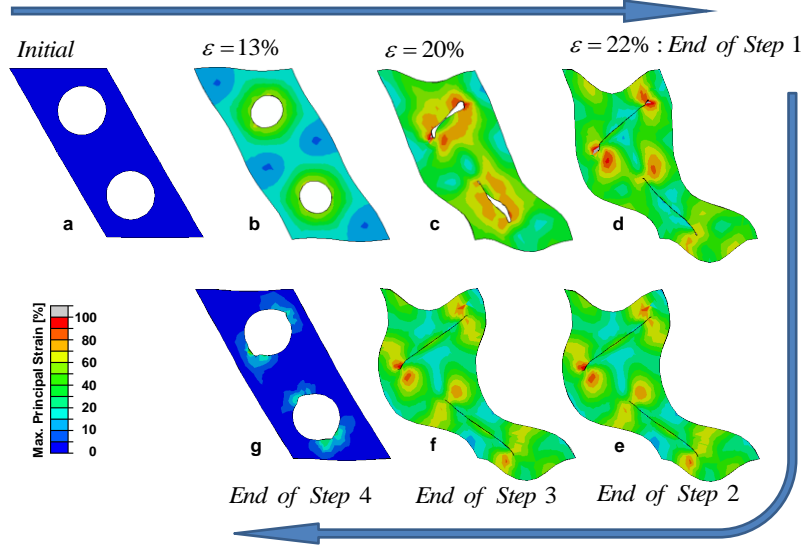


Figure 3.4 Numerical results for the SMP thermo-mechanical cycle. Snapshots of the hexagonal lattice during Step 1, hot-pressing at different strain levels (a-d), and at the end of Steps 2, cooling down (e), 3, un-loading (f) and 4, reheating (g). The color gives indications of the maximum principal strain distribution.

The stress-strain behavior of the SMP is captured using a two-mechanism constitutive model.^[15] The stress response is decomposed into two contributions: the resistance due to stretching and orientation of the molecular network (σ_N), mechanism N , and the resistance due to intermolecular interactions (σ_V), mechanism V . At the applied temperature T , the total stress acting on the material is given by

$$\boldsymbol{\sigma} = \boldsymbol{\sigma}_N + V_V \boldsymbol{\sigma}_V \quad (3.1)$$

where $V_V = 1 - \frac{1}{1 + \exp\left[-\frac{T - T_g + A_1}{A_2}\right]}$ with A_1 and A_2 as material parameters defining the position and width of the zone where mechanism V becomes significant.

The shape memory behavior is taken into account by having σ_V depend on $(T - T_g)$. When $T > T_g$ the material is characterized by a rubbery behavior; as T decreases toward

T_g , the material becomes increasingly glassy and locked into the deformation. The constitutive model is implemented into a user-defined subroutine (VUMAT) of the commercial finite element code ABAQUS, and numerical simulations of the whole thermo-mechanical loading history of the structures are performed in four steps (see Figure 3.4) using the model parameters summarized in Table 3.1.

Table 3.1 Material constants for SMP used in the mechanical models.

Rubbery Phase (Mechanism N)	Glassy Phase (Mechanism V)	Temperature Related Constants
	$E = 1500MPa$	
	$\nu = 0.45$	
$\mu = 1.72MPa$	$\dot{\gamma}_0 = 52 \times 10^6/sec$	$T_g = 343K$
$N = 4.33$	$\Delta G = 92 \times 10^{-21}J$	$A_1 = 20K$
$K = 16.7MPa$	$S_0 = 56MPa$	$A_2 = 5K$
	$S_{ss} = 28MPa$	
	$h = 400MPa$	

μ is the elastic shear modulus, N is the parameter relating to the limiting chain extensibility, K is the bulk modulus, E is the Young's modulus, ν is Poisson's ratio, $\dot{\gamma}_0$ is pre-exponential shear strain rate factor, ΔG is activation energy, s_0 is the initial athermal deformation resistance, s_{ss} is the athermal deformation resistance value at the steady state, h is the softening slope (the slope of the yield drop with respect to plastic strain).

Step 1) *Hot-pressing*. T increases above T_g , so σ_v vanishes and the material exhibits rubber-like behavior. The stability of the structure is investigated by conducting a Bloch wave analysis.^[26] At an applied strain, $\varepsilon = 11\%$, a critical instability is detected, leading to the same pattern previously observed under constrained swelling,^[15] which is characterized by sheared voids where the shear direction alternates back and forth from row to row (see Figure 3.4a-c). Further compression leads to complete closure of the voids at $\varepsilon = 22\%$ (Figure 3.4d), in agreement with experimental observation (Figure 3.2h). In the simulations, further compression was avoided to prevent too much mesh

distortion.

Step 2) *Cooling down.* T decreases to 20 °C, and σ_v increases, making the material much stiffer and preserving the pattern (Figure 3.4e);

Step 3) *Unloading.* The press is removed, but the holes remain completely closed (Figure 3.4f), and the elastic energy is stored in the material;

Step 4) *Reheating up.* T increases above T_g so that the structure again exhibits a rubbery behavior (σ_v vanishes again) and the initial shape and pattern are elastically recovered (see Figure 3.4g).

As seen in Figure 3.4, the numerical analysis nicely captured the deformation, pattern transformation and recovery of the SMP structures. Moreover, the analysis revealed a strong dependency of the onset of instability on the porosity of the structure. Thus the discrepancy between experiments and simulations observed close to the onset of instability at $\varepsilon = 13\%$ (Figure 3.2g and 3.4b) may be attributed to a small difference in porosity between the model and the tested sample. Additionally, we find that for the considered structures with voids of 1 μm in diameter the surface energy (22.8 mJ/m² measured by goniometer) is roughly two orders magnitude smaller than the elastic recovery energy, making the recovery autonomous upon reheating. Since the strain energy is proportional to L^3 (with L denoting the characteristic material dimension), while the surface energy is proportional L^2 , a decrease of the voids diameter will increase the contribution of the surface energy. An approximate analysis suggests that the surface energy will play an important role for voids 10 times smaller than those considered in this study.

3.3.3 Color displays with SMP periodic membranes

To demonstrate the flexibility of color and transparency change in our SMP periodic membranes and their potential applications, we exploited two possible renderings of the SMP membranes. First, a “Penn” logo was pre-fabricated within the 2D membrane (Figure 3.5a, b). The template for replica molding was fabricated by exposing the negative-tone photoresist, epoxy POSS, to UV light through a photomask with “Penn” logo, followed by 3-beam holographic lithography to create hexagonal array of pillars in the surrounding area (Figure 3.5c). Since the region with “Penn” was mostly crosslinked in the first step, the second exposure did not produce any pillar in this region but shallow voids (Figure 3.5d). After replica-molding the template to SMP membrane, there was no or little color diffracted from this region in sharp contrast to the bright color from the surrounding area (Figure 3.5e, g). When the SMP membrane was hot-pressed above T_g , “Penn” logo disappeared as the film became transparent (Figure 3.5f). When reheated, the “Penn” logo reappeared together with its colorful background, confirming the success of shape recovery. Here, the logo was pre-fabricated in the permanent shape, which could be temporarily erased upon deformation.

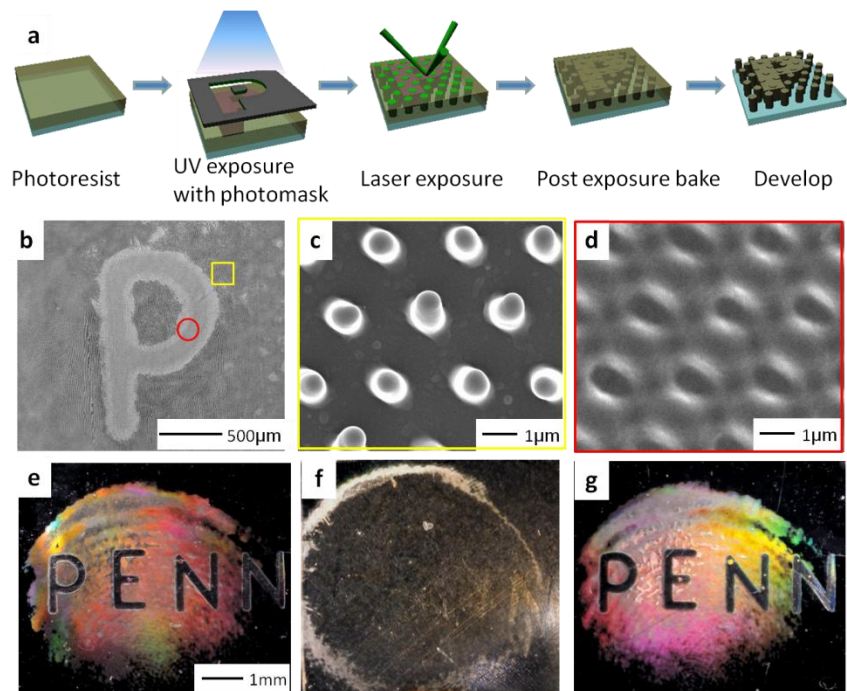


Figure 3.5 Display of “PENNN” embedded in a 2D SMP membrane. (a) Schematic illustration of the fabrication of template. (b-d) SEM images of the photoresist template before replication to the SMP membrane. (b) A low magnification SEM image of the “P” character in the template. (c) SEM image of the structure outside “P” character, yellow square, showing tall pillars. (d) SEM image of the structure inside the “P” character, red circle, showing nearly flat film with shallow voids. e-g. Optical images of the original (e), deformed (f) and recovered (g) SMP films.

In a second approach, the “Penn” logo was introduced as a temporary shape by a rubber stamp indented into the SMP membrane during heating (Figure 3.6a) at 90 °C. The stamp was released after the film was cooled down to room temperature. As seen in Figure 3.6b and 3.6d, the indented region was transparent, especially at the sharp corners of the letters, presumably receiving higher stress, while the background remained colorful. When reheated, the “Penn” logo was erased (Figure 3.6c, e). In this way, different letters or patterns could be “finger-printed” and reprogrammed into the same SMP membrane repeatedly, which could be extremely useful as a user-friendly touch screen display or

fingerprinting by tailoring the SMP T_g near the body temperature. It should be noted that all the displays presented here require no extra energy to maintain the displayed state.

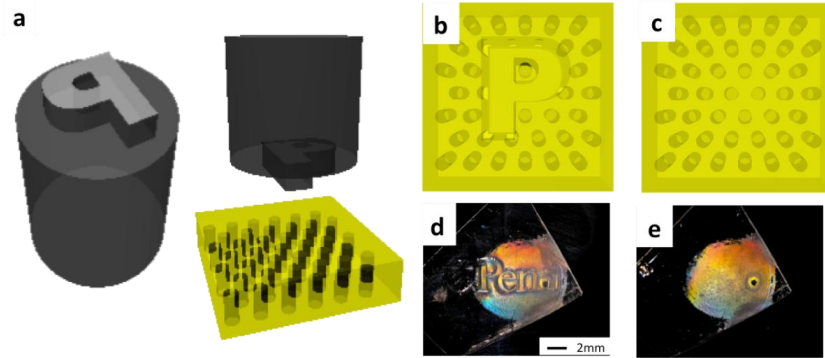


Figure 3.6 Indentation display on the SMP membrane. Schematic illustrations of (a) indentation of a stamp with a letter “P” into a heated SMP membrane, (b) the display of letter “P” in the SMP membrane in the deformed region and (c) structural recovery upon reheating. (d-e). Corresponding optical images of the indented “Penn” in the colored SMP membrane (d) and its erase after reheating the SMP membrane to 90 °C (e).

3.4 Conclusions

We prepared 2D periodic membrane in SMPs, and studied the mechanical instability and shape memory effect. When hot-pressed, the membrane underwent pattern transformation from a $p6mm$ hexagonal lattice of circular holes (1 μm diameter) to a $p2gg$ pattern of elliptical slits (width varied from a few hundreds of nm to a few nm), and eventually the holes were completely closed. The original film is colorful because of the diffraction from the periodic micropattern and can be reversibly switched to a transparent state by mechanical deformation above the material’s T_g . Upon reheating, the deformed patterns were able to recover, hence, restoring the diffraction color. The combination of pattern transformation and shape memory effect in a 2D periodic membrane offers several distinctive characteristics. 1) It is the first demonstration of instabilities induced by loading in the direction perpendicular to the voids in microstructured SMPs, which is

more desirable in practical applications than approaches such as solvent swelling and in-plane compression. 2) The temporarily deformed structure and the resulting color can be fixed without the need for continuous input of external trigger; they can also be programmed continuously by varying the mechanical strain level. 3) The continuum mechanical analyses have faithfully captured the buckling and post-buckling behaviors of the SMP membrane observed experimentally. Importantly, the model suggests that the surface energy plays a negligible role comparing with elastic energy when the void dimension is comparable to the wavelength of light, leading to autonomous and fast shape recovery of the microstructure.

We emphasize that while the diffraction color change is demonstrated in temperature responsive SMPs here, there are a broad range of stimuli responsive material systems in the literature, allowing for fine-tuning the transition temperature, switching speed, degree of responsiveness, number of temporary states, and the type of stimulus. For example, the T_g of the epoxy SMP used in our system could be lowered (e.g. to 30 °C) by increasing the concentration of more flexible crosslinker, decylamine.^[25] SMPs that can store up to three different shapes in temporary states have been reported.^[7, 27] We expect that the study of tuning periodic structures via combined pattern transformation and shape memory effect will shed new light in harnessing the mechanical response of soft materials and advancing a wide range of technologies, including color displays, sensors, camouflage, and energy efficient building components (e.g. smart windows and responsive façade).

3.5 Reference

- [1] A. Lendlein; R. Langer, *Science* **2002**, *296*, 1673-1676.
- [2] C. Liu; H. Qin; P. T. Mather, *J. Mater. Chem.* **2007**, *17*, 1543-1558.
- [3] A. Lendlein; H. Y. Jiang; O. Junger; R. Langer, *Nature* **2005**, *434*, 879-882.
- [4] J. M. Ortega; W. Small; T. S. Wilson; W. J. Benett; J. M. Loge; D. J. Maitland, *IEEE Trans. Biomed. Eng.* **2007**, *54*, 1722-1724.
- [5] C. M. Yakacki; R. Shandas; D. Safranski; A. M. Ortega; K. Sassaman; K. Gall, *Adv. Funct. Mater.* **2008**, *18*, 2428-2435.
- [6] T. Chung; A. Rorno-Uribe; P. T. Mather, *Macromolecules* **2008**, *41*, 184-192.
- [7] T. Xie, *Nature* **2010**, *464*, 267-270.
- [8] T. Xie; X. C. Xiao; J. J. Li; R. M. Wang, *Adv. Mater.* **2010**, *22*, 4390-+.
- [9] L. Sun; W. M. Huang, *Soft Matter* **2010**, *6*, 4403-4406.
- [10] N. Liu; Q. Xie; W. M. Huang; S. J. Phee; N. Q. Guo, *J. Micromech. Microeng.* **2008**, *18*.
- [11] Y. Zhao; W. M. Huang; Y. Q. Fu, *J. Micromech. Microeng.* **2011**, *21*.
- [12] T. Mullin; S. Deschanel; K. Bertoldi; M. C. Boyce, *Physical Review Letters* **2007**, *99*, 084301.
- [13] S. Willshaw; T. Mullin, *Soft Matter* **2012**, *8*, 1747-1750.
- [14] Y. Zhang; E. A. Matsumoto; A. Peter; P. C. Lin; R. D. Kamien; S. Yang, *Nano Lett.* **2008**, *8*, 1192-1196.
- [15] J. H. Jang; C. Y. Koh; K. Bertoldi; M. C. Boyce; E. L. Thomas, *Nano Lett.* **2009**, *9*, 2113-2119.
- [16] S. Singamaneni; K. Bertoldi; S. Chang; J. H. Jang; E. L. Thomas; M. C. Boyce; V. V. Tsukruk, *ACS Appl. Mater. Interfaces* **2009**, *1*, 42-47.

- [17] X. Zhu; G. Wu; R. Dong; C.-M. Chen; S. Yang, *Soft Matter* **2012**, 8, 8088-8093.
- [18] X. L. Zhu; Y. Zhang; D. Chandra; S. C. Cheng; J. M. Kikkawa; S. Yang, *Appl. Phys. Lett.* **2008**, 93, 161911.
- [19] D. Krishnan; H. T. Johnson, *J. Mech. Phys. Solids* **2009**, 57, 1500-1513.
- [20] S. Singamaneni; K. Bertoldi; S. Chang; J. H. Jang; S. L. Young; E. L. Thomas; M. C. Boyce; V. V. Tsukruk, *Adv. Funct. Mater.* **2009**, 19, 1426-1436.
- [21] K. Bertoldi; P. M. Reis; S. Willshaw; T. Mullin, *Advanced Materials* **2010**, 22, 361-366.
- [22] M. Izumi; A. M. Sweeney; D. DeMartini; J. C. Weaver; M. L. Powers; A. Tao; T. V. Silvas; R. M. Kramer; W. J. Crookes-Goodson; L. M. Mathger; R. R. Naik; R. T. Hanlon; D. E. Morse, *J. R. Soc. Interface* **2010**, 7, 549-560.
- [23] Y. Xu; X. Zhu; S. Yang, *ACS nano* **2009**, 3, 3251-3259.
- [24] J. H. Moon; A. J. Kim; J. C. Crocker; S. Yang, *Adv. Mater.* **2007**, 19, 2508-2512.
- [25] T. Xie; I. A. Rousseau, *Polymer* **2009**, 50, 1852-1856.
- [26] K. Bertoldi; M. C. Boyce; S. Deschanel; S. M. Prange; T. Mullin, *J. Mech. Phys. Solids* **2008**, 56, 2642-2668.
- [27] I. Bellin; S. Kelch; R. Langer; A. Lendlein, *Proc. Natl. Acad. Sci. U. S. A.* **2006**, 103, 18043-18047.

Chapter 4

Fabrication of High-Aspect-Ratio One-Dimensional Organic/inorganic Hybrid Nanogratings via Holographic Lithography

4.1 Introduction

One-dimensional (1D) periodic structures in micron- and nano- scale have been of interest for many applications, including diffraction gratings, linear polarizers,^[1-3] plasma etching masks,^[4-5] photonic^[6] and phononic crystals.^[7] There have been extensive studies to fabricate 1D structures using techniques, including photolithography,^[4,8] e-beam lithography,^[9-10] replica molding,^[11] holographic lithography (HL),^[12-13] and nanoimprint lithography^[14] in different materials.^[2, 4-6, 15] 1D structures with high aspect ratio (AR = height/ width) are desired for many applications. For example, as plasma etching masks, high AR structures that offer better etch resistance and structure fidelity are often desired.^[4-5] As grating structures, high AR could lead to new properties, such as blazed transmission gratings via total external reflection on the grating sidewalls for x-rays incident at graze angles.^[2] As 1D photonic crystals, high AR structures could offer higher intensity reflection peak at the photonic stop band.^[6]

However, direct fabrication of high AR structures has been challenging using conventional organic polymer resists, especially in the nanoscale. First, the major limitation is the depth-of-focus (DOF), which defines the maximum photoresist thickness. In photolithography, DOF and the critical dimension (CD, also the minimum feature size) are determined by^[16]

$$CD = k_1 \frac{\lambda}{NA} \quad (4.1)$$

$$DOF = k_2 \frac{\lambda}{NA^2} \quad (4.2)$$

where λ is the wavelength of light, NA is the numerical aperture of the lens, and k_1 and k_2 are processing related constants. Decreasing λ and increasing NA could decrease CD . However, DOF is reduced more rapidly. For 193 nm lithography the AR is typically less than 3.^[17] Therefore, multi-step hard mask etching steps are necessary to create high AR structures for certain inorganic materials, which add complexity and cost to the fabrication. Secondly, high AR structures tend to pattern collapse due to the capillary force during solvent drying.^[18-21] To address this problem, high AR structures are typically dried using supercritical CO₂ dryer to minimize surface tension.

Unlike photolithography, where DOF is closely related to lenses, depth-of-penetration in holographic lithography (HL) is solely dependent on λ of the incident light and the optical density (OD) of photoresist at the given λ . Thus, it is possible to create high AR structures with AR > 3 by carefully choosing photoresist with high transparency.

Here, we fabricated organic/inorganic hybrid high AR (up to 10) 1D nanogratings with variable feature size via HL. Epoxy-functionalized polyhedral oligomeric silsesquoxane (epoxy-POSS) was used as photoresist due to its high thermal and mechanical stability. The periodicity of the nanograting was controlled by the incident beam angle, while the filling fraction could be altered by exposure dosage. We also discussed the surface roughness formation mechanism in the POSS nanogratings, and demonstrated roughness reduction by increasing exposure dosage. Furthermore, we

showed that the epoxy-POSS nanogratings could be directly calcinated to silica-like nanogratings.

4.2 Experimental Methods

4.2.1 Fabrication

The 1D nanogratings were fabricated with controllable periodicity using the set-up and fabrication process shown in Figure 4.1a. Epoxy polyhedral oligomeric silsesquoxane (epoxy-POSS, EP0408 from Hybrid Plastics) (Figure 4.1b), an organosilicate, was used as photoresist, following the HL procedure reported earlier.^[22-26] In brief, the photoresist film was prepared from 50-70 wt% Epoxy-POSS and 0.9 wt% (relative to the mass of Epoxy-POSS) Irgacure 261 (visible photoacid generator (PAG), Ciba Specialty Chemicals) in γ -butyrolactone (GBL, Sigma-Aldrich), which was spun-coated on pre-cleaned cover glasses, followed by soft bake at 50 °C for 40 min and 95 °C for 2 min, respectively. The film was exposed to a diode-pumped Nd:YVO₄ laser ($\lambda = 532$ nm, Verdi-6, Coherent) with overall 1.0 W laser input (before beam splitting) for 2 s to 6 s. The angle between two laser beams could be varied to achieve different feature sizes. After exposure, the film was post-exposure baked (PEB) at 50 °C for 35 s to crosslink the exposed regions, followed by development in propylene glycol monomethyl ether acetate (PGMEA, Sigma-Aldrich) for 30 min. Before drying in CO₂ supercritical point dryer (SAMDRI®-PVT-3D, Tousimis), the wet samples were rinsed in isopropanol (IPA, Sigma-Aldrich) for another 30 min.

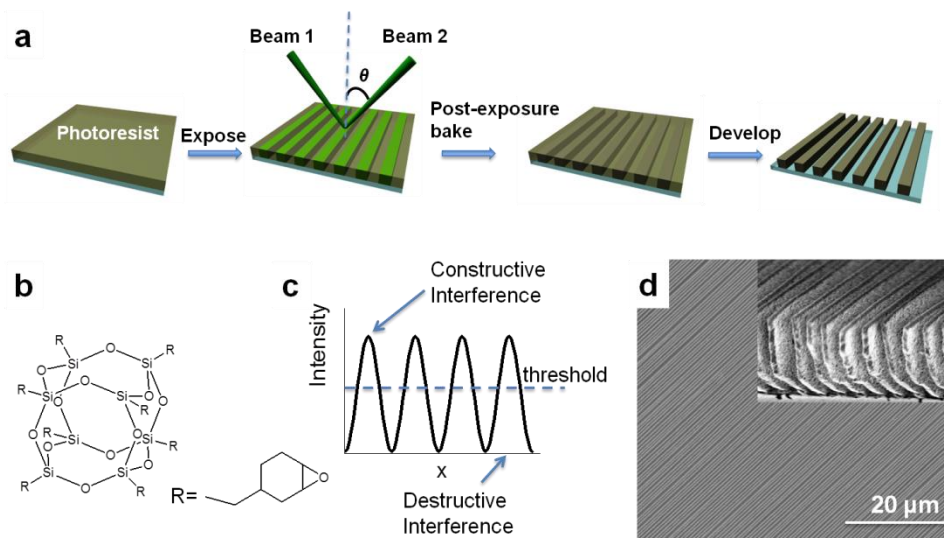


Figure 4.1 Holographic lithography (HL) process to fabricate 1D high AR structures. (a) Schematics of HL fabrication process. (b) Chemical Structure of epoxy polyhedral oligomeric silsesquoxane (epoxy-POSS). (c) Two-beam interference intensity profile. 1D periodic structure is formed in the regions, where the light intensity is higher than the threshold. (d) Top-view and cross-sectional view (inset) SEM images of the 1D grating with 300 nm line width, 600 nm pitch and AR= 10.

4.2.2 Characterization

High resolution SEM images were taken from FEI 600 Quanta FEG Environmental Scanning Electron Microscope (ESEM). The chemical compositions in the 1D structures were determined by energy-dispersive X-ray (EDX) analysis coupled on the same ESEM. The 1D nanogratings with thickness $\sim 2 \mu\text{m}$ were supported on silicon wafers for EDX measurement.

4.3 Results and discussion

The 1D nanograting was fabricated by two-beam interference lithography (see Figure 4.1) with an intensity profile shown in Figure 4.1 c. During exposure, photoacids were generated, which catalyzed the ring-opening reactions during the PEB process. In the regions where the exposure dosage is higher than the threshold value, epoxy-POSS

becomes fully crosslinked. In the regions where the exposure dosage is below the threshold, the epoxy-POSS is not crosslinked or partially crosslinked, therefore, could be removed by an organic solvent during developing, leaving the high AR nanograting (AR=10 in Figure 4.1 d).

Compared to conventional organic photoresist, e.g. SU-8, which is commonly used in ultrathick films to create high AR microstructures, epoxy-POSS offers three advantages: 1) as an organic-inorganic hybrid material, it has thermal and mechanical stability in-between silica and polymers,^[22-23] 2) it can be directly converted to silica-like material by calcinations in O₂, and 3) it can serve as a template to backfill both inorganic and organic materials, where the template can be removed using hydrofluoric (HF) aqueous solution at room temperature.^[24-25] Typically, the organic template has to be removed by calcination above 500 °C, making it impossible to template functional structures from another organic materials.

In HL, periodicity of the 1D structure is determined by

$$2d \cdot \sin\theta = \lambda \quad (4.3)$$

where d is the periodicity of the 1D structure. θ is the half angle between two incident laser beams, and λ is the wavelength of the light, which is 532 nm in our system. At this wavelength, epoxy-POSS was completely transparent. According to Eq. 3, the minimum periodicity in our case is 266 nm, half of λ . The calculated periodicity from different incident angles is summarized in Table 4.1.

Table 4.1 Theoretical periodicity of two-beam interference lithography from variable incident beam half angles.

θ (°)	$\sin(\theta)$	d (nm)
1	0.0175	15,241
15	0.2588	1,028
30	0.5000	532
45	0.7071	376
60	0.8660	307
89	0.9998	266

From Table 4.1 we could see that periodicity as large as 15 μm is feasible with 532 nm HL with $\theta = 1^\circ$. However, when θ is very small, it becomes difficult to accurately control the incident angle. To demonstrate the flexibility of HL, we varied θ to create 1D gratings of different periodicities. As seen in Figure 4.2, both samples had the same height, 2 μm . With $\theta = 7.5^\circ$, sample with pitch of 2 μm (in agreement with calculated value), line width of 500 nm, and the AR of 4 was obtained (Figure 4.2a). With $\theta = 26^\circ$, the sample had pitch of 600 nm, line width of 250 nm, and the AR of 8 (Figure 4.2b). In both cases, high AR 1D gratings were observed with long-range order.

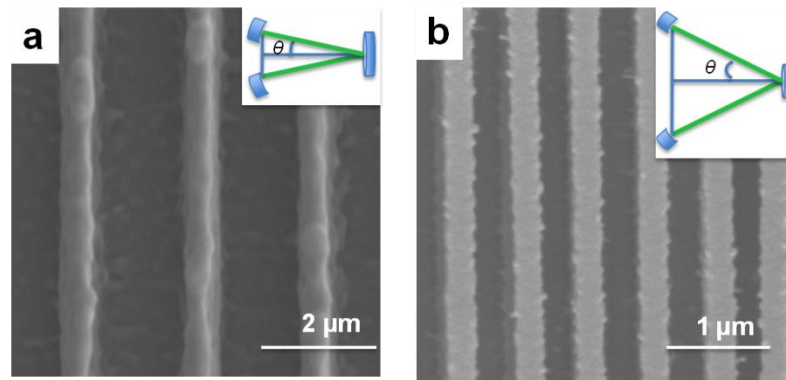


Figure 4.2 Top-view SEM images of 1D structures fabricated with different incident beam half angles, $\theta = 7.5^\circ$ and 26° , respectively. Inset: schematics showing the beam

position. (a) Line width 500 nm, pitch 2 μm , height 2 μm , and AR =4. (b) Line width 250 nm, pitch 600 nm, height 2 μm , and AR=8.

While periodicity is tuned by θ , the line width can be altered by parameters, including exposure dosage, PAG concentration and PEB duration, all of which are closely related to the epoxy-POSS crosslinking density. As illustrated in Figure 4.1c, when the interference intensity is higher than the threshold, epoxy-POSS would be sufficiently crosslinked and not soluble in the developer. Longer exposure time increases the amplitude of entire intensity profile, thus, a larger portion of POSS remains after the development, leading to larger line width. Similarly, higher PAG concentration and longer PEB duration would also result in more crosslinking and larger line width. As seen in Figure 4.3, when increasing the exposure time from 3s, 4s to 5s, while keeping other parameters constant, 600 nm pitch, 2 μm height, [PAG] = 0.9 wt%, exposure power 1.0 W and PEB at 50 $^{\circ}\text{C}$ for 35 s, the line width increased from 200 nm to 230 nm and 260 nm, respectively. Given the same sample height, the smallest line width gave rise to the highest AR. Here, with the 200 nm line width, the AR of sample in Figure 4.3a is 10. In comparison, while AR as high as 100 can be achieved by SU-8 in the micron scale, high AR (up to 10) can only be achieved by X-ray LIGA process for submicron features,^[27] which is not easily accessible for most research groups. 1D nanostructures with AR > 10 will be difficult to achieve since the nanowalls are too thin and highly unstable. They can be easily distorted or collapsed due to solvent swelling by the developer, which decreases the film modulus, or by capillary force during drying.

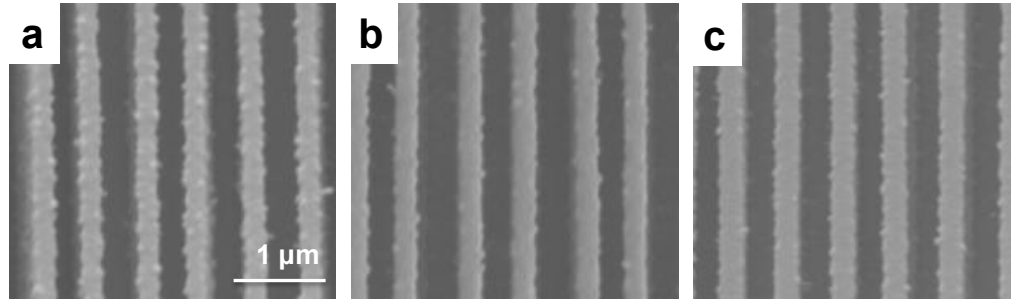


Figure 4.3 Top-view SEM images of 1D structures with exposure duration of 3 s, 4 s and 5 s, respectively. (a) Line width 200 nm, AR=10. (b) Line width 230 nm, AR= 8.7. (c) Line width 260 nm, AR= 7.7.

We found that the epoxy-POSS nanogratings fabricated here show different extent of surface nanoroughness (20-50 nm in diameter), which is not desired for applications such as optical gratings or etch masks. The sidewall roughness in gratings could lead to undesired phase shift, thus influence the overall performance.^[28] As for plasma etching masks, the protrusions of the rough sidewall act as a shadowing mask for the incident ions, which induces the striations at the sidewalls of both the underlayer and the resist.^[29] Thus, it is important to control and minimize such surface roughness.

Previously, we showed that epoxy-POSS is less crosslinked than SU-8 and the nanoroughness could be generated due to microphase separation of the polymer chain segments in a nonsolvent during the rinsing step in HL process.^[26] When immersed in the developer, PGMEA, which is a good solvent, the polymer network swells. In the rinsing solvent, IPA, which is a poor solvent, the loosely crosslinked epoxy POSS network deswells, resulting in microphase separation. The degree of roughness can be tuned by the crosslinking density of the polymer network, which is dependent on the loading of photoacid generators, the exposure dosage, and the choice of developer and rinsing solvent. When the crosslinking density was sufficiently high, the molecular

weight between crosslinks (M_c) or the mesh size, as well as the available chain segments for collapsing out of solvent are dramatically decreased, the surface of the microstructure becomes smooth.

Similarly, we believe the rough surface was also due to low crosslinking density of the epoxy-POSS network. Therefore, surface roughness can be reduced by increasing exposure dosage, which in turn leads to higher crosslinking density. As shown in Figure 4.4, the surface obtained from 3 s exposure time (Figure 4. 4a) was much rougher than the one exposed for 6 s (Figure 4. 4b), while all other fabrication parameters were kept the same.

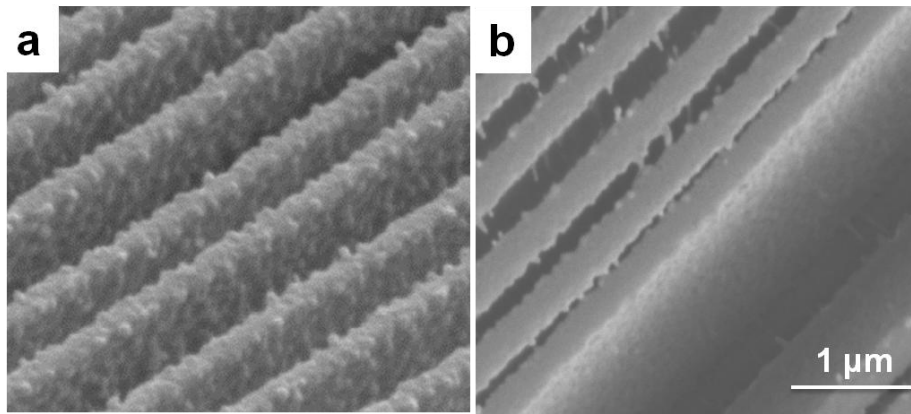


Figure 4.4 Side-view SEM images of the 1D structures fabricated by HL, showing smooth and rough surfaces. (a) Very rough surface fabricated with 3 s exposure duration. (b) Relatively smooth surface fabricated with 6 s exposure duration. Other Fabrication parameters were kept the same.

Previously, we have converted epoxy-POSS 3D structures fabricated by 4-beam HL to silica-like ones by oxygen plasma or calcination in oxygen for backfilling to create 3D polymeric photonic crystals,^[23] and high-temperature (up to 1300 °C), high refractive index silicon carbide (SiC) photonic crystals.^[24] Because the 3D structures are interpenetrated network, thus, providing mechanical support during conversion and

backfilling, the 3D silica structures and their replicas are able to maintain the structure integrity during the multiple processing steps. In comparison, there will be no such support for 1D structures.

According to thermogravimetric analysis (TGA) from literatures,^[22, 30] epoxy-POSS is thermally stable up to 350 °C in air, above which the organic moieties start to decompose. Here we attempted calcinations in O₂ at 500 °C for 2 h, since the organic part of epoxy POSS could be decomposed, leaving mainly Si-O skeleton. For comparison, we calcinated half of the sample and examined the structure using SEM and chemical composition using energy-dispersive X-ray (EDX) spectroscopy. As seen in Figure 4.5, carbon was nearly removed after calcination. The ratios of different elements are summarized in Table 4.2. The measured compositions were SiC_{6.2}O_{2.4} for the original sample and SiC_{0.3}O_{2.5} for the calcinated one, close to SiO₂ assuming carbon was completely removed. The measured chemical composition of the original epoxy-POSS slightly deviated from the ideal cage, SiC₈O_{2.5}, since epoxy-POSS precursor used in our experiments was a cage mixture, (C₈H₁₃O)_n(SiO_{1.5})_n (n= 8, 10 or 12). By increasing the calcination time to 10 h, the tracing amount of carbon could be completely removed. As seen in the inset of Figure 4.5, the high AR 1D silica-like structure remained in a good shape after the conversion.

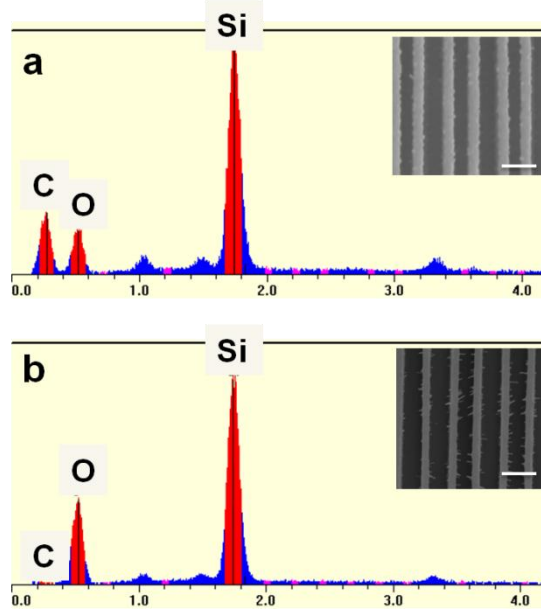


Figure 4.5 Energy-dispersive X-ray spectra and top-view SEM images (inset) for high AR 1D structures before and after calcination. (a) Original POSS structure, showing C, O and Si peaks. (2) After the calcinations at 500 °C in O₂ for 2 h, the carbon peak disappeared. Line width 200 nm, pitch 600 nm, height 2 μm, and AR=10. Scale bar: 1 μm.

Table 4.2 EDX element analysis data of the original and calcinated samples.

	C	O	Si	Ideal composition	Measured composition
Original POSS	65.32	25.18	10.50	SiC ₈ O _{2.5}	SiC _{6.2} O _{2.4}
Calcinated POSS	6.97	66.45	26.57	SiO ₂	SiC _{0.3} O _{2.5}

4.4 Conclusions

In summary, we have fabricated high AR 1D nanogratings with feature size ranging from 200 nm to 500 nm in line width, 600 nm - 2 μm in pitch, AR up to 10 via two-beam HL. The hybrid material, epoxy-POSS, was used as the negative-tone photoresist, which offered high thermal and mechanical stability. The periodicity of nanograting was tuned by incident beam angle, while the filling fraction was altered by several

parameters, including exposure dosage, PAG concentration and PEB duration. The undesired surface roughness could be reduced by increasing POSS crosslinking density with longer exposure time. Furthermore, we showed that the epoxy-POSS nanogratings could be directly converted to silica-like nanogratings upon calcination. We believe the hybrid nanostructures fabricated here would benefit other applications, such as hypersonic (GHz) phononic crystals^[31] by backfilling an elastomeric (e.g. PDMS) or stiff material (e.g. spin on glass) that have very different elastic constants. Compared to 1D lamellar multilayers,^[7] the vertical nanowalls could potentially offer larger bandgaps and Q values. Further, it is possible to convert the high AR 1D structure from epoxy-POSS to other inorganic materials with high refractive index, such as SiC,^[24] for ultrahigh temperature photonic applications.

4.5 Reference

- [1] M. L. Schattenburg; E. H. Anderson; H. I. Smith, *Phys. Scr.* **1990**, *41*, 13-20.
- [2] M. Ahn; R. K. Heilmann; M. L. Schattenburg, *J. Vac. Sci. Technol. B* **2007**, *25*, 2593-2597.
- [3] E. W. Palmer; M. C. Hutley; A. Franks; J. F. Verrill; B. Gale, *Rep. Prog. Phys.* **1975**, *38*, 975-1048.
- [4] Y. C. Tseng; A. U. Mane; J. W. Elam; S. B. Darling, *Adv. Mater.* **2012**, *24*, 2608-2613.
- [5] M. K. Hooda; M. Wadhwa; S. Verma; M. M. Nayak; P. J. George; A. K. Paul, *Vacuum* **2010**, *84*, 1142-1148.
- [6] K. Hosomi; T. Fukamachi; H. Yamada; T. Katsuyama; Y. Arakawa, *Photonics*

Nanostruct. **2006**, *4*, 30-34.

[7] D. Schneider; F. Liaqat; E. H. El Boudouti; Y. El Hassouani; B. Djafari-Rouhani; W. Tremel; H. J. Butt; G. Fytas, *Nano Lett.* **2012**, *12*, 3101-3108.

[8] V. R. Tirumala; R. Divan; D. C. Mancini; G. T. Caneba, *Microsyst. Technol.* **2005**, *11*, 347-352.

[9] S. Pauliac-Vaujour; C. Comboroure; C. Vizioz; S. Barnola; P. Brianceau; V. M. Alvaro; C. Dupre; T. Ernst, *J. Vac. Sci. Technol. B* **2008**, *26*, 2583-2586.

[10] F. Fruleux-Cornu; J. Penaud; E. Dubois; M. Francois, *Microelectron. Eng.* **2006**, *83*, 776-779.

[11] Y. N. Xia; G. M. Whitesides, *Annu. Rev. Mater. Sci.* **1998**, *28*, 153-184.

[12] J. M. Carter; D. B. Olster; M. L. Schattenburg; A. Yen; H. I. Smith, *J. Vac. Sci. Technol. B* **1992**, *10*, 2909-2911.

[13] A. Yen; E. H. Anderson; R. A. Ghanbari; M. L. Schattenburg; H. I. Smith, *Appl. Optics* **1992**, *31*, 4540-4545.

[14] S. Y. Chou; P. R. Krauss; W. Zhang; L. J. Guo; L. Zhuang, *J. Vac. Sci. Technol. B* **1997**, *15*, 2897-2904.

[15] X. M. Yang; R. D. Peters; P. F. Nealey; H. H. Solak; F. Cerrina, *Macromolecules* **2000**, *33*, 9575-9582.

[16] S. Okazaki, *J. Vac. Sci. Technol. B* **1991**, *9*, 2829-2833.

[17] *International Technology Roadmap for Semiconductors.*

[18] T. Tanaka; M. Morigami; N. Atoda, *Jpn. J. Appl. Phys.* **1993**, *32*, 6059-6064.

[19] M. P. Stoykovich; H. B. Cao; K. Yoshimoto; L. E. Ocola; P. F. Nealey, *Adv. Mater.* **2003**, *15*, 1180-+.

- [20] D. Chandra; S. Yang, *Langmuir* **2009**, *25*, 10430-10434.
- [21] D. Chandra; S. Yang, *Acc. Chem. Res.* **2010**, *43*, 1080-1091.
- [22] J. H. Moon; J. S. Seo; Y. G. Xu; S. Yang, *J. Mater. Chem.* **2009**, *19*, 4687-4691.
- [23] Y. A. Xu; X. L. Zhu; S. Yang, *ACS Nano* **2009**, *3*, 3251-3259.
- [24] Y. A. Xu; M. Guron; X. L. Zhu; L. G. Sneddon; S. Yang, *Chem. Mat.* **2010**, *22*, 5957-5963.
- [25] J. Li; J. Shim; J. Deng; J. T. B. Overvelde; X. Zhu; K. Bertoldi; S. Yang, *Soft Matter* **2012**, *8*, 10322-10328.
- [26] J. Li; G. Q. Liang; X. L. Zhu; S. Yang, *Adv. Funct. Mater.* **2012**, *22*, 2980-2986.
- [27] A. del Campo; C. Greiner, *J. Micromech. Microeng.* **2007**, *17*, R81-R95.
- [28] L. Poladian; F. Ladouceur; P. D. Miller, *J. Opt. Soc. Am. B-Opt. Phys.* **1997**, *14*, 1339-1344.
- [29] G. Kokkoris; V. Constantoudis; E. Gogolides, *IEEE Trans. Plasma Sci.* **2009**, *37*, 1705-1714.
- [30] A. Fina; D. Tabuani; F. Carniato; A. Frache; E. Boccaleri; G. Camino, *Thermochim. Acta* **2006**, *440*, 36-42.
- [31] T. Gorishnyy; C. K. Ullal; M. Maldovan; G. Fytas; E. L. Thomas, *Phys. Rev. Lett.* **2005**, *94*, 115501.

Chapter 5

Transforming One-Dimensional Nanowalls to Long-Range Ordered Two-Dimensional Nanowaves – Exploiting Buckling Instability and Nanofibers Effect in Holographic Lithography

5.1 Introduction

Periodically structured materials, whose physical properties are functions of the structural parameters, including shape, geometry, size, orientation and arrangement, are of wide interests for applications, such as controlling the light, sound or heat wave propagation,^[1-2] wetting,^[3-4] adhesion,^[5-6] and cell sensing and proliferation.^[7] In many applications, high aspect ratio (AR = height/width) structures are desired. For example, as plasma etching masks, they offer better etching resistance and structure fidelity.^[8-9] As grating structures, high AR could lead to new properties, such as blazed transmission gratings via total external reflection on the grating sidewalls for x-rays incident at graze angles.^[10] As photonic crystals, high AR structures have higher intensity reflection peak at the photonic stop band.^[11]

However, high AR structures are mechanically unstable. When the film is developed in the lithographic process it tends to collapse due to capillary force^[12-15] or to be buckled due to anisotropically swelling.^[16-17] Specifically, it has been shown that 1D structures can be laterally buckled into irregular two-dimensional (2D) wavy patterns due to compressive residual stress generated in the film confined on a rigid substrate, for example, by deposition of a thin layer of metal or semiconductor,^[18-19] or by swelling.^[16] Because the compressive stresses induced by swelling and heating/cooling are isotropic

laterally, most of the buckling structures reported in literature are random. It will be intriguing to harness such instability for pattern transformation, specifically, to create highly ordered, high AR 2D wavy patterns by lateral buckling of 1D high AR structures, leading to very different physical properties.

Here, we created highly ordered 2D nanowaves from a commonly used negative-tone photoresist SU-8 during two-beam HL by buckling of high AR (up to 6) 1D nanowalls (periodicity of 600 nm). During the development stage, the 1D pattern went through a constrained swelling in the good solvent, leading to the global buckling. The degree of lateral undulation could be controlled by tuning the pattern AR and exposure dosage. Different from literature, the nanowalls in our system were buckled in the same direction with long-range ordering. Between the nanowalls, interconnecting nanofibers (30-50 nm in diameter) were formed between nanowalls when exposed to high dosages. By comparing experimental results with finite-element analysis, we confirmed that nanofibers formed only in the buckled film when the neighboring walls were close enough; they prevented the recovery of the deformed nanowalls to their original state, thus, minimizing random instability after critical point drying. The nanowave structure showed weaker reflecting color under an ambient light and lower transmittance compared to the nanowalls. Using double exposure through a photomask, followed by development, we created patterns consisting of both nanowaves and nanowalls for optical display by harnessing the distinct optical properties in the two regions.

5.2 Experimental Methods

5.2.1 Holographic lithography

The 1D periodic nanowall pattern was fabricated by two-beam holographic

lithography (HL) (see Figure 1a). In brief, the photoresist film was prepared from 40-58 wt% EPON SU-8 (from Shell Chemical) and 2.0 wt% (relative to the mass of SU-8) Irgacure 261 (visible photoacid generator, Ciba Specialty Chemicals) in γ -butyrolactone (GBL, Sigma-Aldrich). The solution was spin coated on a pre-cleaned cover glass, followed by soft bake at 65 °C for 5 min and 95 °C for 15 min, respectively. The film was exposed to a diode-pumped Nd:YVO₄ laser ($\lambda = 532$ nm, Verdi-6, Coherent) with overall 1.0 W laser input (before beam splitting) for 15 to 20 s. The angle between two laser beams could be varied to achieve different feature size. After exposure, the film was post-exposure baked (PEB) at 65 °C and 95 °C for 2 min, respectively to crosslink the exposed regions, followed by development in propylene glycol monomethyl ether acetate (PGMEA, Sigma-Aldrich) for 30 min. Before drying in critical point dryer (CPD, SAMDRI®-PVT-3D, Tousimis), the wet samples were rinsed in isopropanol (IPA, Sigma-Aldrich) for 20 min.

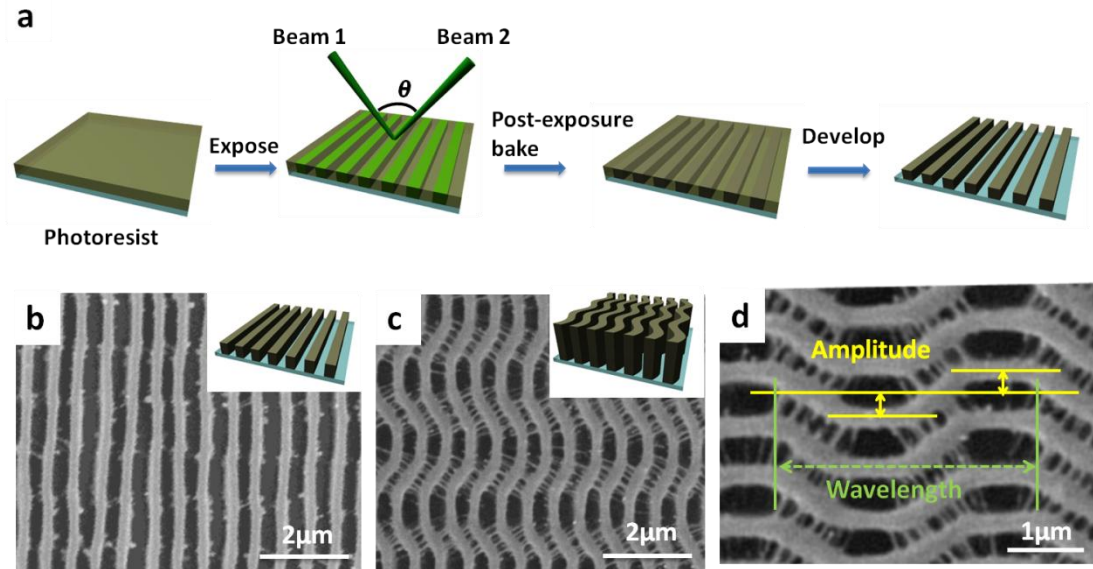


Figure 5.1 Fabrication of 1D nanowalls and 2D nanowaves via two-beam holographic lithography. (a) Schematics of the holographic lithography process. (b-c) Top-view SEM

images and schematics of (b) 1D nanowalls (width 300 nm, pitch 600 nm, AR ~2) and (c) 2D nanowaves (width 300 nm, pitch 600 nm, AR ~6). (d) Higher magnification SEM image of (c) with indication of the amplitude and wavelength of the nanowaves. Amplitude (yellow arrow) is indicated as the distance between center of the original wall to that of the maximum buckled position. Wavelength (green arrow) is the longitudinal periodicity of the nanowaves.

5.2.2 Fiber removal and re-swelling

A buckled sample with many connecting fibers (width 30-50 nm, AR=6) was half covered with aluminum foil and half exposed to oxygen plasma (Harrick Plasma Cleaner PDC-001) for 15 min to remove the nanofibers. Then the aluminum foil was removed and the whole sample was developed in PGMEA for 1 h to re-swell the sample, followed by rinsing in IPA for 30 min, and critical point drying.

5.2.3 Double exposure

The sample was first exposed to interference beam at 532 nm to create 1D nanowall pattern, followed by UV exposure ($\lambda = 365$ nm, 400 mJ/cm², 97435 Oriel Flood Exposure Source, Newport) through a photomask, including a line pattern with 10 μ m width and 20 μ m pitch, and a “N” letter pattern in millimeter. The film was then PEB, developed in PGMEA and CPD dried as described earlier.

5.2.4 Characterization

SEM images were taken from FEI Strata DB235 Focused Ion Beam (FIB) system and the cross-sectional images were taken from samples milled by the Gallium ion beam. The transmission spectra were acquired by UV-Vis spectrometer (Varian Cary 100).

5.2.5 Finite-element analysis

ABAQUS/Standard,^[32] a commercial finite-element analysis software, was used. Young's modulus and Poisson's ratio of SU-8 were chosen to be 1.7 GPa and 0.49

according to the experimental measurement. Nonlinear static analyses were performed for the post-buckling prediction based on the buckling analysis. Three-dimensional continuum element (C3D8) was adopted with 50 nm in characteristic element length. The swelling ratio of SU-8 was assumed to vary from 1.0 to 1.2 throughout the analyses.

5.3 Results and discussion

The 1D nanowalls were fabricated by two-beam interference lithography (see experimental section and Figure 5.1a), including photoresist spin-coating, pre-exposure bake, exposure, post-exposure bake (PEB), development, solvent rinsing and critical-point drying (CPD). By recording the interference pattern into a selective photoresist, HL has been used to fabricate 1D, 2D, and 3D periodic structures over a large area.^[20-21] The periodicity of the 1D structure could be tuned from a hundred of nanometers to several microns using the green laser by varying the angle between two incident laser beams.^[22] Here, we kept the periodicity constant at 600 nm and the line width around 300 nm for the interest of grating color in the visible to infrared wavelength. The AR of 1D structure was varied by the concentration of SU-8 solution and spin-coating speed, which determined the film thickness.

SU-8, a multifunctional epoxy derivative of a bisphenol-A novalac,^[23] was chosen as the model photoresist (Figure 5.2) because of its compatibility with conventional photolithography and HL,^[24] and high solubility in many organic solvents, allowing for preparation of thick films with high AR. When SU-8 films of different thickness were exposed to the same HL conditions, followed by development in propylene glycol monomethyl ether acetate (PGMEA) and CPD, different types of nanostructures were observed depending on AR (see Figure 5.1). For AR=2 samples, 1D pattern of straight

walls (Figure 5.1b) were observed as expected from two-beam interference. However, for AR=6 samples, highly ordered 2D nanowaves were observed (Figure 5.1c) with wavelength of 3 μm and amplitude of 300 nm (see schematic in Figure 5.1d).

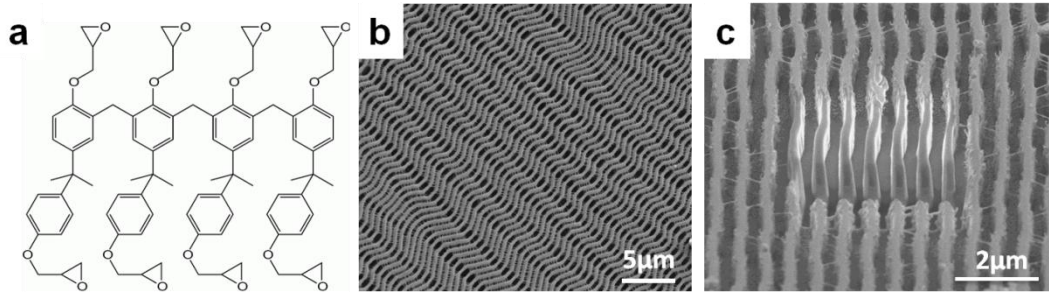


Figure 5.2 (a) Chemical structure of the negative-tone photoresist, SU-8. (b) Top-view SEM image of large area of long-range ordered nanowaves with a few anti-phase boundaries. (c) Cross-sectional SEM image of the nanowaves showing high aspect ratio (AR = 6).

Buckling of 1D lines to 2D wavy patterns has been reported, typically via thermal or solvent swelling induced stress.^[16-19] The 1D lines generally buckle randomly in the xy plane due to isotropic lateral force. In comparison, the nanowaves formed in our system were all bent in the same direction and persisted over a large area (5 mm in diameter). A closer look showed that there were many nanofibers formed between the nanowalls in the AR=6 sample (Figure 5.1d). The role of the fibers will be discussed in detail later.

Swelling-deswelling of SU-8 thin films have been investigated to optimize the processing conditions in photolithography,^[25-26] to study pattern transformation in 2D membranes,^[27-28] and 3D phononic crystals,^[29] and to enhance grafting of polymer brushes on 2D and 3D structures.^[30] Typically in photolithography of 1D structures, pattern collapse of high AR structures is observed due to capillary force during drying. Since we dried the films using CPD, the effect of capillarity should be minimal. We suspect that the buckling occurred in our 1D structures should be attributed to solvent

swelling in the development stage.

Because SU-8 film was confined on the rigid glass substrate, the outer layer would swell more, generating an anisotropic osmotic pressure. Meanwhile, the glassy SU-8 was softened by the developer, thus, lowering the buckling threshold. When the AR is large enough, the compressive force generated at the top of the structure will go beyond the buckling threshold, thus, triggering global buckling of the 1D lines. Supporting this, we observed the buckling of 1D structure under the optical microscope from the developed film immersed in the rinsing solvent, isopropanol (IPA) (Figure 5.3). We did not directly observe the developed film in PGMEA, which was not compatible with the optical microscope. The extent of buckling and morphology could be controlled by material properties, including crosslinking density and modulus, pattern geometry, and polymer-solvent interaction in a nonlinear manner.

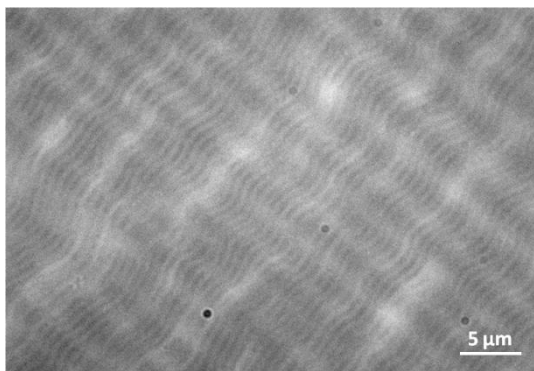


Figure 5.3 Optical image of the developed film immersed in the rinsing solvent, IPA.

The modulus of the as-fabricated SU-8 was measured by AFM nano-indentation, 1.7 GPa, and the swelling ratio in PGMEA was ~ 1.05 -1.1, which agreed well with literature.^[25] If keeping AR constant, but exposing the SU-8 film at a higher dosage, more photoacids will be generated, leading to higher crosslinking density and higher filling

fraction. Thus, we should expect higher film stiffness, which is less prone to buckling. The effect of exposure dosage is shown in Figure 5.4, where samples had the same film thickness (1 μm) but different exposure time (16 s vs. 17 s). Although we did observe increased filling fraction in the film exposed for 17s (Figure 5.4b) compared to that from 16 s (Figure 5.4a), the nanowaves were found formed in the 17 s film, contrary to the prediction. Comparing the straight 1D nanowalls and 2D nanowaves, it was clear that the buckled films all had nanofibers (30-50 nm) (see Figure 5.1 and Figure 5.4); the longer exposure time, the more nanofibers were generated. Nanofiber formation is known to be a byproduct of long exposure during HL.^[31] As shown in Figure 5.4c-d, such effect can be explained by the intensity profiles at different exposure dosage. When the exposure time is increased, interference beam intensity increases. The originally weakly crosslinked regions under shorter exposure time, which would have been removed by developer, now received interference intensity above the critical threshold and become partially crosslinked. Not only the volume-filling fraction is increased but the spacing between neighboring lines becomes smaller due to increase of weakly polymerized regions. It was reported that nanofibers formed and bridged the neighboring nanostructures by networking between the weakly polymerized regions of the nanostructures once the weakly polymerized regions became overlapped within an optimized distance.^[31] Hence, we speculate that the highly dosaged walls had large enough weakly polymerized regions, which was overlapped during global buckling of the 1D walls. Once the distance of the neighboring walls reaching the threshold, the nanofibers began to form from the walls and finally connected the neighboring walls as shown in the Figure 5.2b. We also hypothesize that the formation of nanofibers would

prevent the buckled SU-8 film from returning to the original straight nanowalls as evident by the broken fibers in nearly straight-line patterns (Figure 5.4a), thus, minimizing random lateral buckling of the 1D structure.

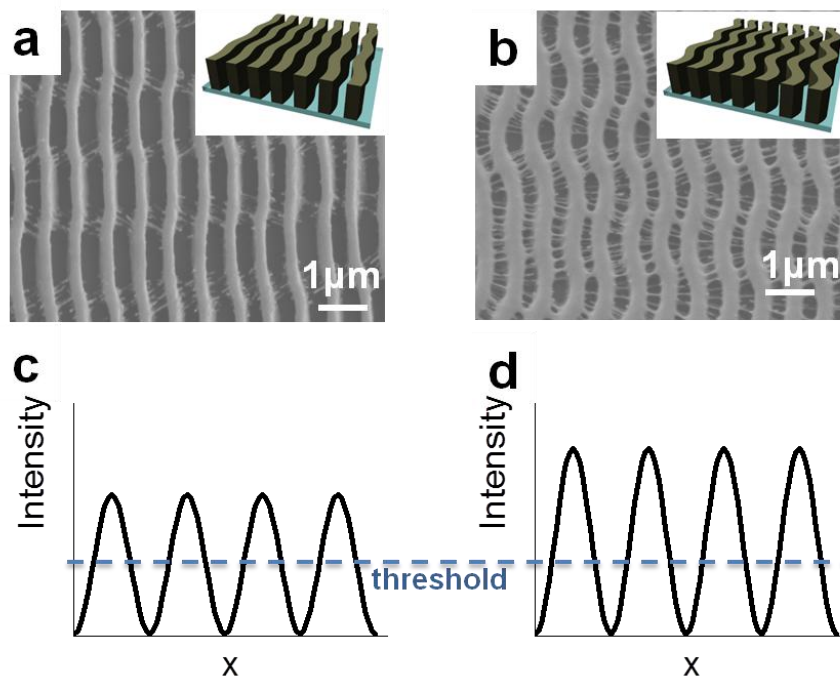


Figure 5.4 Effect of exposure dosage on the degree of buckling of the 1D nanowalls. (a-b) Top-view SEM images and schematics (insets) of nanowaves obtained from HL with exposure time of (a) 16 s and (b) 17 s, resulting in line width of 250 nm and 350 nm, respectively, and different degree of buckling. The later has significant amount of fibers formed between the walls. (c-d) Schematics of two-beam interference intensity profile at different exposure dosages. Regions exposed with intensity higher than the threshold are more crosslinked and remained on the substrate after developing in a good solvent.

To support our hypothesis, we carried out finite-element simulation to better understand the formation of the nanofibers in association with the buckling behavior. We simulated structures with $AR = 2, 4$ and 6 , as a direct comparison to the experimental results shown in Figure 5.1. The simulation results show coinciding relationship between the AR and the buckling magnitude (Figure 5.6a-c). In the plots, the undulation amplitude increases as the swelling ratio increases. It also shows that the amplitude increases faster

when AR is higher. The post-buckling shapes with swelling ratio 1.1 were shown in Figure 5.6d, which also matches the measured amplitudes well.

Finite-element analyses indeed provide more insights on the formation of nanofibers. As seen in Figure 5.1c and Figure 5.4b, the distance between nanowalls, which was initially identical along the wall before buckling, varied as the buckling occurred. There are two causes that make the wall distance to be different in buckled configuration.

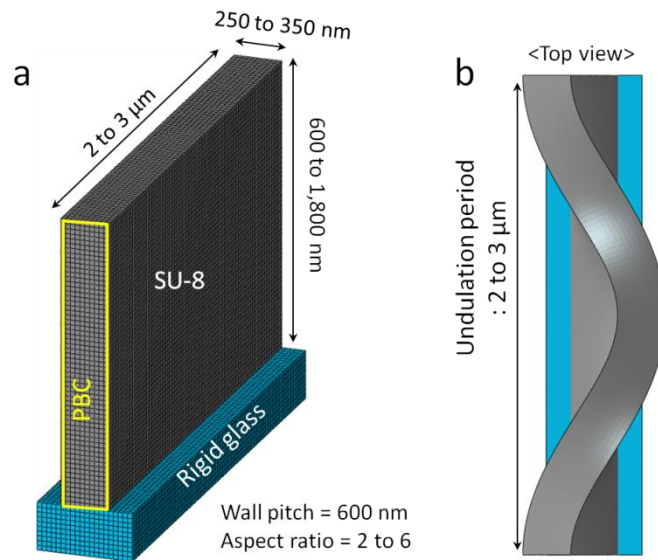


Figure 5.5 Finite element model and buckling prediction, assuming perfect adhesion between the wall and the rigid substrate. (a). Dimension of the wall on the rigid substrate was set according to experiments (pitch 600 nm, width 250-350 nm, height 600-1800 nm, undulation period 2-3 μm). The periodic boundary condition (PBC) was applied on the front (indicated with yellow box in the figure) and rear side of the wall. (b) The predicted buckling mode under swelling. Due to the imposed PBC, the apparent length of the wall (distance between the front and rear side or simply undulation period in the figure) does not change although the actual length of the wall increases during swelling.

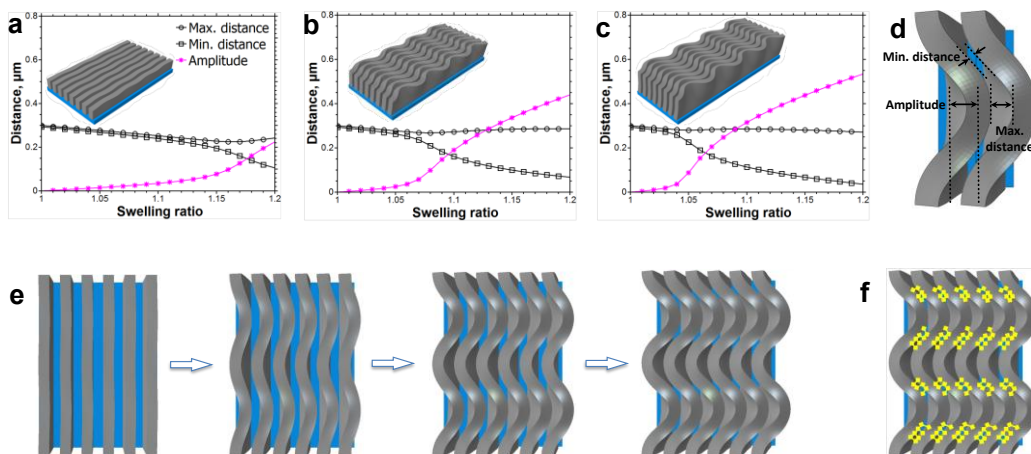


Figure 5.6 Finite-element simulation of the buckling behaviors of 1D nanowalls. (a-c) Changes in the maximum distance (○), minimum distance between walls (□), and the undulation amplitude (★) of the same wall width (300 nm) but different aspect ratios, (a) AR=2. (b) AR= 4. (c) AR=6 as a function of the swelling ratio. (d) The corresponding 3D images of the predicted buckling behaviors of 1D walls of different aspect ratios with swelling ratio of 1.1. (e) Top-view simulated images of the wall distance evolution during buckling. (f) Illustration of nanofibers (yellow) formed mainly in the regions where wall distances are smaller than 200 nm.

Because the bottom of the 1D walls is constrained on the substrate, the 1D walls are not only buckled in the longitudinal direction but also twisted with out-of-plane displacement (See Figure 5.7). Hence, the crest region has the maximum wall distance, and the middle point between two adjacent crest points has the minimum wall distance after buckling (see schematic in Figure 5.6d). The experimental results matched well with the simulations. At the swelling ratio 1.1, the wall distance appears to be larger than 250 nm along the entire structure. This relatively large gap between the walls gave only a few fiber formations as shown in Figure 5.1b. In the case of 300 nm width and AR=6 (Figure 5.6c), however, the minimum wall distance is only about 120 nm at swelling ratio 1.1, while the maximum distance is around 280 nm. In the experiment, the nanofibers were mainly observed in the middle region between two adjacent crest points, of which wall

distance was smaller than 200 nm (Figure 5.1c). A top-view of the wall distance evolution during buckling, as well as the nanofiber distribution can be found in Figure 5.6 e and f. Hence, we clearly demonstrated that the buckling of 1D walls modulated the distance between the neighboring walls and the nanofibers formed only where the distance between the walls was close enough.

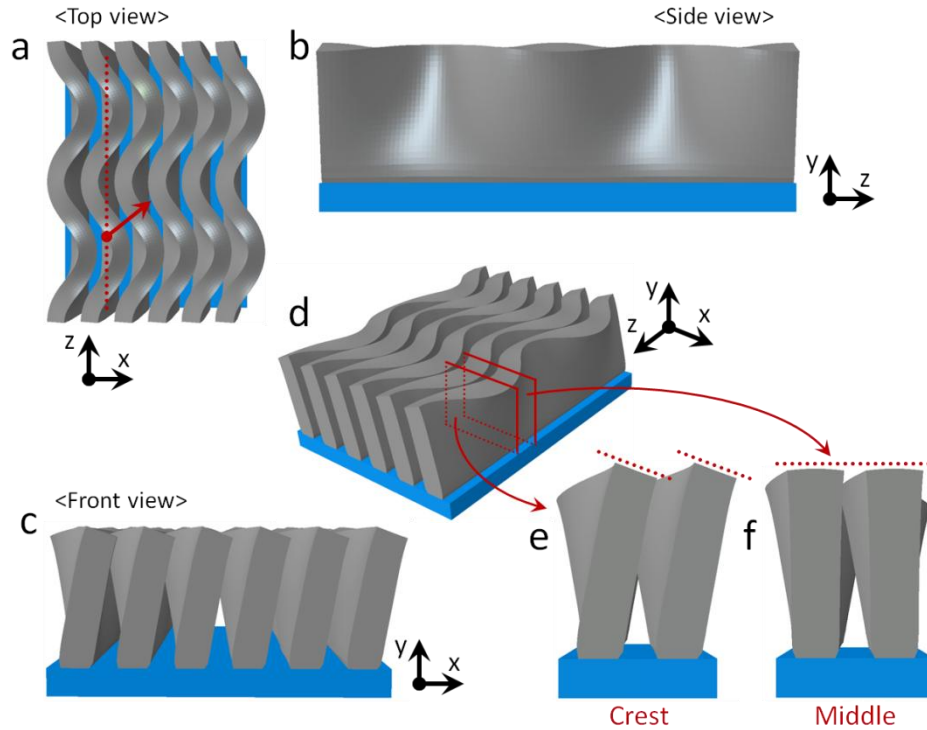


Figure 5.7 The predicted buckled shape. (a) Top, (b) side, (c) front, (d) overall, and (e, f) cross-sectional views of the buckled walls. The cross-sectional view in (e) indicates slight undulations along y-axis (wall height direction) as well as the obvious undulations along x-axis in (a).

As we mentioned earlier, more fibers were generated in the longer exposure sample as a result of decreased gap size because the higher AR should give larger amplitude of buckling. Upon drying, the buckled walls have a tendency to deswell and return to the original straight line geometry, and the distance between neighboring walls increase.

However, with large quantities of fibers connecting the neighboring walls, the walls have to overcome the constraint imposed by the connected fibers to return to their original straight alignment when the walls deswell. Thus, the nanofibers could help to maintain the buckled shape and stabilize the long-range ordered nanowaves. In order to further confirm the effect of fibers, we conducted experiments to remove the fibers, followed by re-swelling in PGMEA. A closer look of these fibers is shown in Figure 5.8a, a cross-sectional SEM image cut by focused ion beam (FIB). The nanofibers appeared throughout the sample from top to bottom. We took a buckled sample with many fibers ($AR=6$), and covered half of it with aluminum foil while leaving the other half exposed to oxygen plasma (OP) treatment. The SEM image after OP is shown in Figure 5.8b, where the nanofibers were nearly completely removed in the exposed region. After removal the aluminum foil, the whole sample was put in the developer, followed by rinsing and drying steps performed before. For the half that still had fibers, the buckled morphology remained the same as before (Figure 5.8c). However, for the other half where fibers were removed, buckling lost the long-range ordering (Figure 5.8d), which unquestionably supported the role of nanofibers in maintaining the long-range ordering of nanowaves. When there were no fibers connecting the neighboring walls, each wall would buckle and compete with the neighboring ones for buckling space. On the other hand, since the space between each wall is very limited in our system comparing to the buckling amplitude, there is not enough space for the walls to deform in a completely random manner.

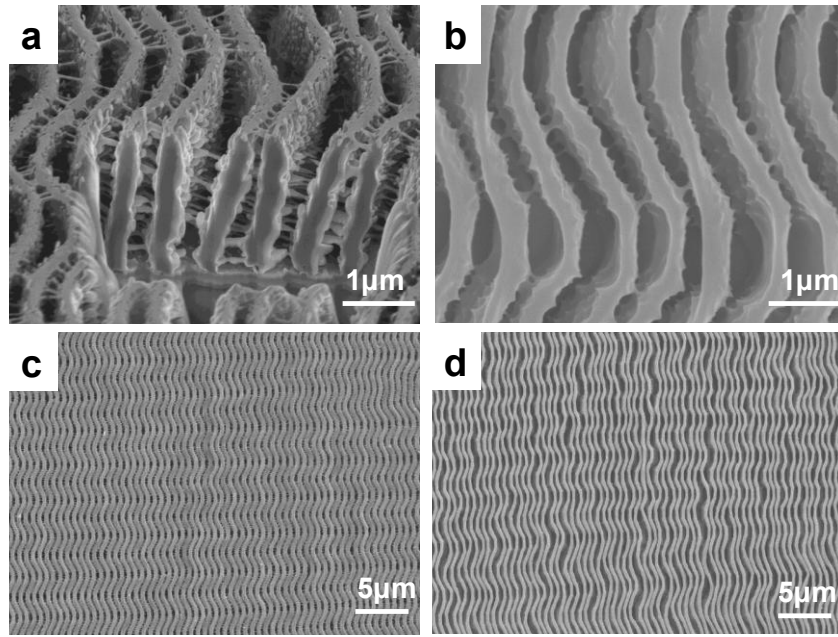


Figure 5.8 Effect of nanofibers in between nanowaves ($AR=6$) to maintain the buckled structure during swelling. (a) Cross-sectional SEM images of nanowaves with a large quantity of interconnecting nanofibers. (b) Top-view SEM image of the nanowaves shown in (a) after 15 min oxygen plasma treatment, showing nearly no nanofibers left. (c-d) Corresponding top-view SEM images of the nanowaves shown in (a) and (b) after re-swelling in PGMEA and drying.

Since both 1D nanowalls and its buckled 2D nanowaves are highly ordered with sub-micron periodicity, they should have distinct optical properties. First, we compared the transmittance of the straight nanowalls, nanowaves, and random deformed line pattern from 350- 800 nm (Figure 5.9a) and their corresponding photos were taken under ambient lighting (Figure 5.9b-d). The 1D nanowalls showed bright, reflected color, which was angle-dependent. Its transmittance spectrum dipped around 500- 600 nm (near its periodic feature size), corresponding to the partial stop band of the 1D photonic structure. The sample with long-range ordered nanowaves also appeared colorful, although the reflectivity was not as strong as the straight nanowalls. Its transmittance was lower than that of the straight nanowall sample, and did not have the characteristic valley. As for the

randomly deformed sample, it appeared white due to the random scattering from the film surface, thus, had the lowest transmittance among the three.

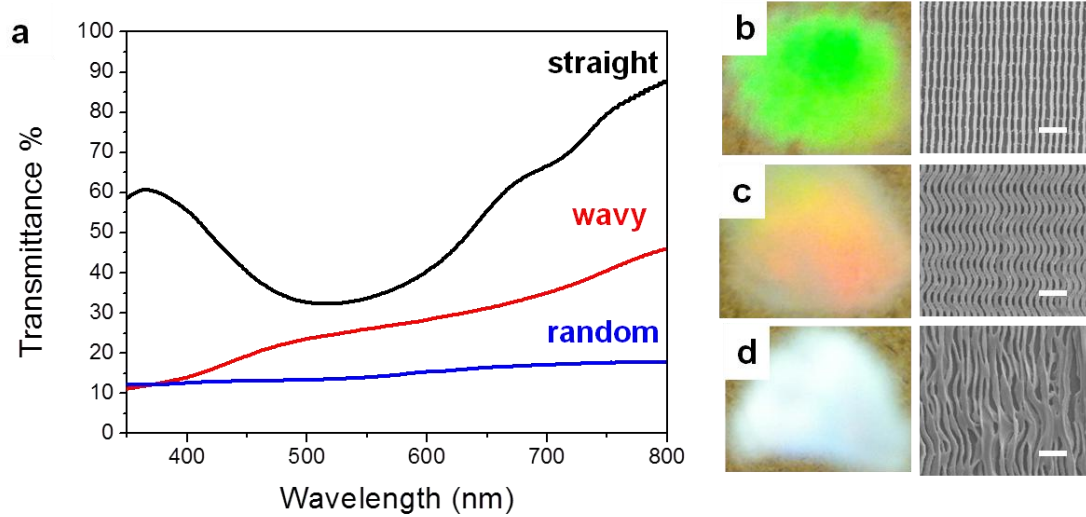


Figure 5.9 Comparison of the optical properties between straight 1D nanowalls, 2D nanowaves with long-range ordering, and randomly collapsed nanowaves. (a) UV-Vis transmittance spectra. (b-d) Photos and corresponding top-view SEM images of various nanostructures. Scale bar: 2 μm .

Lastly, we fabricated complex patterns using double exposure method for optical display. First, the SU-8 film was exposed to interference beams to create the nanostructures, followed by UV exposure through a photomask with micron-sized patterns before PEB (see Figure 5.10a). After the development and CPD, the regions that were not double exposed would go through typical global buckling to form nanowaves, whereas the regions received double exposure would have higher crosslinking density and volume filling fraction, thus, forming straight nanowalls. As a proof-of-concept, we used two types of photomasks: one with 10 μm line width and 20 μm pitch, and the other with a character “N” in millimeter size. The sample double exposed from the 1D photomask showed alternating regions of nanowalls and nanowaves (Figure 5.10b-c) as

expected. To better illustrate the color contrast in the nanowall and nanowave regions, we used a letter “N” photomask as shown in Figure 5.10d. The region within the character was double exposed and appeared more transparent than the surrounding region, which appeared orange. The double exposed regions had higher volume filling fraction of SU-8 and the straight nanowalls were nearly connecting with each other. Therefore, they appeared more like a flat film, which was transparent. The color from the surrounding regions was the reflection color from the nanowaves.

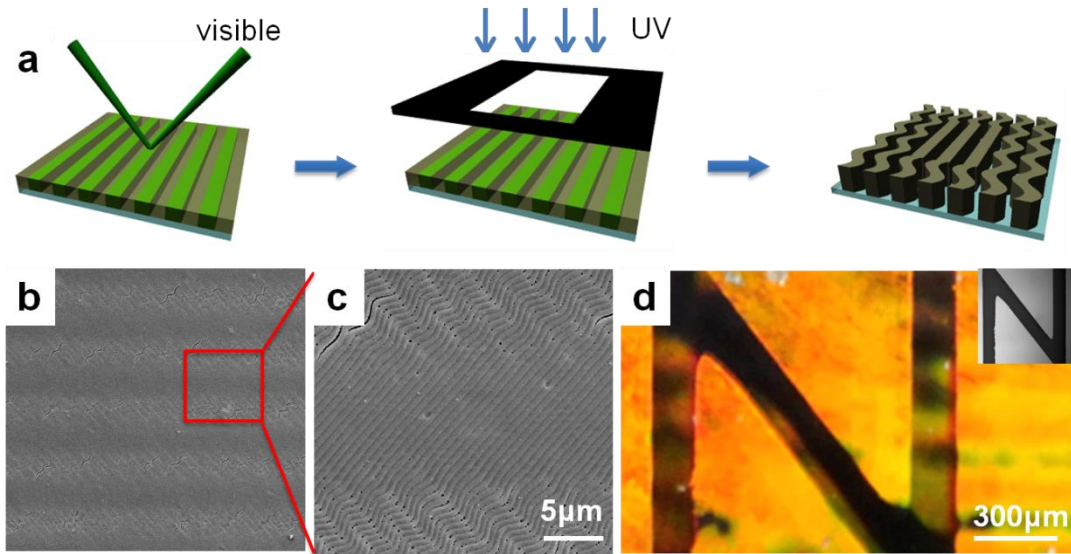


Figure 5.10 Double exposures to pattern nanowaves together with nanowalls. (a) Schematic illustration of the double exposure process, including HL at visible light first, followed by UV exposure through a photomask. (b-c) SEM images of the hierarchical structure, consisting of nanowaves and nanowalls (width 300 nm, pitch 600 nm, AR ~6) in a microscaled 1D grating (width 10 μm , pitch 20 μm). (c) Double exposed regions showing straight lines with higher filling fraction, while the single exposed regions showing typical nanowaves. (d) Photo of a film double exposed with photomask of letter “N”. Inset: optical image of the photomask. The double exposed region appeared more transparent than the surrounding due to higher filling fraction. The latter appeared orange due to reflection from the nanowaves.

5.4 Conclusions

In summary, we have fabricated long-range ordered 1D nanowalls and 2D

nanowaves via holographic lithography and confined buckling. The extent of lateral undulation could be controlled by varying structure geometry and exposure dosage. Nanofibers were generated between the buckled nanowalls due to overlapping of the neighboring weakly crosslinked regions. By comparing experimental results with finite-element analysis, we investigated the buckling mechanism and confirmed that the nanofibers played a significant role that prevented deformed nanowalls from recovering to their original state, resulting in long-range ordered wavy structures. The ordered nanowave structure showed weaker reflecting color under an ambient light and lower transmittance compared to its straight counterpart, nanowalls; whereas the randomly deformed nanowaves appeared white. By combining HL and photolithography through a photomask, we demonstrated micropatterning of nanowaves vs. nanowalls for optical display. We believe that the investigation of buckling mechanism in 1D structures via nanofiber formation will provide new insights to fabricate highly ordered 2D and 3D structures by harnessing instability and pattern transformation. It will also allow us to create a rich library of complex patterns for advance applications, such as displays, waveguides, wire-grid linear polarizers, sensors, and substrates for guiding cell proliferation.

5.5 Reference

- [1] J. D. Joannopoulos; S. G. Johnson; R. D. Meade; J. N. Winn, in *Photonic Crystals*. 2nd ed.; Princeton University Press: **2008**.
- [2] T. Gorishnyy; C. K. Ullal; M. Maldovan; G. Fytas; E. L. Thomas, *Phys. Rev. Lett.* **2005**, *94*, 4.

- [3] T. N. Krupenkin; J. A. Taylor; T. M. Schneider; S. Yang, *Langmuir* **2004**, *20*, 3824-3827.
- [4] M. K. Kwak; H. E. Jeong; T. I. Kim; H. Yoon; K. Y. Suh, *Soft Matter* **2010**, *6*, 1849-1857.
- [5] H. E. Jeong; K. Y. Suh, *Nano Today* **2009**, *4*, 335-346.
- [6] M. K. Kwak; C. Pang; H.-E. Jeong; H.-N. Kim; H. Yoon; H.-S. Jung; K.-Y. Suh, *Adv. Funct. Mater.* **2011**, *21*, 3606-3616.
- [7] C. S. Chen; J. Tan; J. Tien, *Annu. Rev. Biomed. Eng.* **2004**, *6*, 275-302.
- [8] Y. C. Tseng; A. U. Mane; J. W. Elam; S. B. Darling, *Adv. Mater.* **2012**, *24*, 2608-2613.
- [9] M. K. Hooda; M. Wadhwa; S. Verma; M. M. Nayak; P. J. George; A. K. Paul, *Vacuum* **2010**, *84*, 1142-1148.
- [10] M. Ahn; R. K. Heilmann; M. L. Schattenburg, *J. Vac. Sci. Technol. B* **2007**, *25*, 2593-2597.
- [11] K. Hosomi; T. Fukamachi; H. Yamada; T. Katsuyama; Y. Arakawa, *Photonics Nanostruct.* **2006**, *4*, 30-34.
- [12] T. Tanaka; M. Morigami; N. Atoda, *Jpn. J. Appl. Phys.* **1993**, *32*, 6059-6064.
- [13] M. P. Stoykovich; H. B. Cao; K. Yoshimoto; L. E. Ocola; P. F. Nealey, *Adv. Mater.* **2003**, *15*, 1180-1184.
- [14] D. Chandra; S. Yang, *Langmuir* **2009**, *25*, 10430-10434.
- [15] D. Chandra; S. Yang, *Acc. Chem. Res.* **2010**, *43*, 1080-1091.
- [16] S. J. DuPont; R. S. Cates; P. G. Stroot; R. Toomey, *Soft Matter* **2010**, *6*, 3876-3882.

- [17] M. K. Kang; R. Huang, *Int. J. Appl. Mech.* **2011**, *3*, 219-233.
- [18] M. Darnon; T. Chevolleau; O. Joubert; S. Maitrejean; J. C. Barbe; J. Torres, *Appl. Phys. Lett.* **2007**, *91*, 194103.
- [19] H. Yoon; A. Ghosh; J. Y. Han; S. H. Sung; W. B. Lee; K. Char, *Adv. Funct. Mater.* **2012**, *22*, 3723-3728.
- [20] J. H. Moon; J. Ford; S. Yang, *Polym. Adv. Tech.* **2006**, *17*, 83-93.
- [21] J. H. Moon; S. Yang, *Chem. Rev.* **2010**, *110*, 547-574.
- [22] X. Zhu; G. Liang; Y. Xu; S.-C. Cheng; S. Yang, *J. Opt. Soc. Am. B* **2010**, *27*, 2534-2541.
- [23] J. M. Shaw; J. D. Gelorme; N. C. LaBianca; W. E. Conley; S. J. Holmes, *IBM J. Res. Dev.* **1997**, *41*, 81-94.
- [24] M. Campbell; D. N. Sharp; M. T. Harrison; R. G. Denning; A. J. Turberfield, *Nature* **2000**, *404*, 53-56.
- [25] Z. Zhou; Q.-A. Huang; W. Li; W. Lu; Z. Zhu; M. Feng In *The Swelling Effects During the Development Processes of Deep Uv Lithography of Su-8 Photoresists: Theoretical Study, Simulation and Verification*, Sensors, 2007 IEEE, 28-31 Oct. 2007; 2007; pp 325-328.
- [26] K. Wouters; R. Puers, *J. Micromech. Microeng.* **2010**, *20*, 095013.
- [27] S. Singamaneni; K. Bertoldi; S. Chang; J. H. Jang; S. L. Young; E. L. Thomas; M. C. Boyce; V. V. Tsukruk, *Adv. Funct. Mater.* **2009**, *19*, 1426-1436.
- [28] S. Singamaneni; K. Bertoldi; S. Chang; J. H. Jang; E. L. Thomas; M. C. Boyce; V. V. Tsukruk, *ACS Appl. Mater. Interfaces* **2009**, *1*, 42-47.
- [29] J. H. Jang; C. Y. Koh; K. Bertoldi; M. C. Boyce; E. L. Thomas, *Nano Lett.* **2009**,

9, 2113-2119.

[30] H. N. Kim; J. H. Kang; W. M. Jin; J. H. Moon, *Soft Matter* **2011**, 7, 2989-2993.

[31] S. H. Park; T. W. Lim; D. Y. Yang; N. C. Cho; K. S. Lee, *Appl. Phys. Lett.* **2006**, 89, 173133.

[32] H. D. Hibbitt, *Nucl. Eng. Des.* **1984**, 77, 271-297.

Chapter 6

Summary and outlook

6.1 Summary

In this thesis, I use HL to fabricate 1D, 2D and 3D periodic structures with various material choices, including organic negative tone photoresists SU-8, hybrid photoresist POSS, shape memory polymer and inorganic material, e.g. silica. The goal of my thesis is to investigate their intrinsic structure-property relationship, harness and utilize the mechanical instability, and explore novel applications as tunable periodic structures.

While many of the current studies of periodic structures have focused on their unique optical and mechanical properties, we are interested in multi-functionality of these materials. For instance, surface property of periodic structures is also interesting due to the intrinsic topography, which is closely related to wetting, adhesion and adsorption behaviors. To mimic the surface property of butterfly wings while not interfering the optical/mechanical effects of the periodic structures, it is important to control surface roughness. In Chapter 2, I created 3D diamond photonic crystals with controllable nano-roughness by exploiting microphase separation of the swollen, crosslinked polymer chains from a nonsolvent during the rinsing step in the HL process. The degree of roughness can be tuned by varying the crosslinking density of the polymer network and the solvent affinity to the polymer chains. The dual-scale roughness (periodic microstructure and nanopores) offers new opportunities previously unstudied, that is to combine actions on a 3D photonic crystal, including light interference, light absorption and self-cleaning without cross-talk. Further, we demonstrate ~ 6 times of dye adsorption enhancement on rough diamond crystals compared to those with smooth surface. We

believe that 3D photonic structure with controllable nano-roughness will open the door for many other applications, such as DSSCs and QDSCs, fuel cells, catalysis, and protein/drug delivery.

For tunable periodic structures, most of the current approaches to tune the photonic properties are based on changing lattice constant or refractive index, resulting in change of PBG position up to a few hundreds of nanometers. It is attractive to expand this tunable range, for example, from transparency to colorful states. In Chapter 3, we explored the pattern transformation and symmetry change by compressing 2D SMP membrane with pores arranged in a hexagonal array to realize the reconfigurable switching between transparency and colorful states according to thermal-mechanical stimulus. When hot-pressed, the membrane underwent pattern transformation from a *p6mm* hexagonal lattice of circular holes (1 μm diameter) to a *p2gg* pattern of elliptical slits (width varied from a few hundreds of nm to a few nm), and eventually the holes were completely closed. The original film is colorful because of the diffraction from the periodic micro-pattern and can be reversibly switched to a transparent state by mechanical deformation above the material's T_g . Upon reheating, the deformed patterns were able to recover, hence, restoring the diffraction color. The combination of pattern transformation and shape memory effect in a 2D periodic membrane offers several distinctive characteristics. Firstly, it is the first demonstration of instabilities induced by loading in the direction perpendicular to the voids in microstructured SMPs, which is more desirable in practical applications than approaches such as solvent swelling and in-plane compression. Secondly, the temporarily deformed structure and the resulting color can be fixed without the need for continuous input of external trigger; they can also be

programmed continuously by varying the mechanical strain level. Thirdly, the continuum mechanical analyses have faithfully captured the buckling and post-buckling behaviors of the SMP membrane observed experimentally. Importantly, the model suggests that the surface energy plays a negligible role comparing with elastic energy when the void dimension is comparable to the wavelength of light, leading to autonomous and fast shape recovery of the microstructure.

On the other hand, direct fabricating of high AR periodic structures by top-down lithographic approaches, especially in the nano-scale, is still challenging, due to limitations of *DOF* in photolithography, pattern collapse from capillary force and distortion due to solvent swelling. In Chapter 4 and 5, I discussed the fabrication of nano-scale 1D periodic structures via HL from different photoresists, i.e. POSS and SU-8. The 1D structures are of interests for gratings, plasma etching masks and photonic / phononic crystal applications. Using HL and supercritical drying, we could avoid the problems of *DOF* and pattern collapse when fabricating high AR 1D structures. However, solvent swelling induced instability could induce buckling of the 1D structures. In Chapter 4, we fabricated high AR 1D nanogratings with feature size ranging from 200 nm to 500 nm in line width, 600 nm - 2 μm in pitch, AR up to 10 via two-beam HL. The hybrid material, epoxy-POSS, was used as the negative-tone photoresist, which offered high thermal and mechanical stability. The periodicity of nanograting was tuned by incident beam angle, while the filling fraction was altered by several parameters, including exposure dosage, PAG concentration and PEB duration. The undesired surface roughness could be reduced by increasing POSS crosslinking density with longer exposure time. Furthermore, we showed that the epoxy-POSS nanogratings could be directly converted to silica-like

nanogratings upon calcination. We believe the hybrid nanostructures fabricated here would benefit other applications, such as hypersonic (GHz) phononic crystals by backfilling an elastomeric (e.g. PDMS) or stiff material (e.g. spin on glass) that have very different elastic constants. Compared to 1D lamellar multilayers, the vertical nanowalls could potentially offer larger bandgaps and Q values. Further, it is possible to convert the high AR 1D structure from epoxy-POSS to other inorganic materials with high refractive index, such as SiC, for ultrahigh temperature photonic applications.

In Chapter 5, I fabricated long-range ordered 1D nanowalls and 2D nanowaves via holographic lithography and confined buckling. The extent of lateral undulation could be controlled by varying structure geometry and exposure dosage. Nanofibers were generated between the buckled nanowalls due to overlapping of the neighboring weakly crosslinked regions. By comparing experimental results with finite-element analysis, we investigated the buckling mechanism and confirmed that the nanofibers played a significant role that prevented deformed nanowalls from recovering to their original state, resulting in long-range ordered wavy structures. The ordered nanowave structure showed weaker reflecting color under an ambient light and lower transmittance compared to its straight counterpart, nanowalls; whereas the randomly deformed nanowaves appeared white. By combining HL and photolithography through a photomask, we demonstrated micropatterning of nanowaves vs. nanowalls for optical display. We believe that the investigation of buckling mechanism in 1D structures via nanofiber formation will provide new insights to fabricate highly ordered 2D and 3D structures by harnessing instability and pattern transformation. It will also allow us to create a rich library of complex patterns for advance applications, such as displays, waveguides, wire-grid linear

polarizers, sensors, and substrates for guiding cell proliferation.

6.2 Outlook

The study presented in this thesis offers critical insights new opportunities for many fundamental researches and practical applications. Besides the self-cleaning nature, 3D photonic structures with controllable roughness and high surface area are essentially attractive for energy related applications, such as dye sensitized solar cell (DSSC).^[1] DSSC is typically composed of a porous layer of TiO_2 as the electrode and a monolayer of charge-transfer dye coated on TiO_2 for light harvesting. To enhance surface area for charge transport, TiO_2 nanoparticles assembly is used in conventional DSSC. Recently, it has been demonstrated that when the holographically patterned 3D photonic structure is converted to TiO_2 as an electrode for DSSC, enhanced light efficiency was observed compared to inverted colloidal crystalline TiO_2 attributed to the bi-continuous micro-scale structure.^[2-3] Nevertheless, the overall efficiency of the solar cell, $\sim 5\%$ ^[2], still lags behind that of the best DSSC. Now, we can convert the rough 3D POSS template to inverse TiO_2 3D structures with roughness for absorbing more dyes, and they are expected to have higher efficiency as DSSC.

As for the 2D tunable periodic structures, although we only demonstrated the diffraction color change in temperature responsive SMPs, there are actually a broad range of stimuli responsive material systems in the literature, allowing for fine-tuning the transition temperature, switching speed, degree of responsiveness, number of temporary states, and the type of stimulus. For example, light will offer better spatial control of the mechanical deformation and potential reversibility. We can synthesize Au nanorod (AuNR) with SMP composites by taking advantage of the photothermal effect of Au NRs

in the visible and IR region.^[4] The light responsiveness in such system has already been demonstrated by us with a 2D micro-pillar array. We can also incorporate this composite material into different periodic structures, and investigate the property change according to reversible tuning.

For high AR 1D structures, there is strong interest using them as 1D hypersonic (GHz) phononic crystals, which will allow for manipulation of acoustic wave propagation.^[5] We are already collaborating with Prof. Fytas at Max Planck Institute to study hypersonic phononic behaviors from these structures, which already show promising results. Compared to 1D lamellar multilayers they worked before, the 1D vertical walls could potentially offer large bandgaps and Q values. It would be attractive to continue in this direction by varying the structure dimensions and material choices. On the other hand, the 2D nanowave structures could also benefit many fundamental studies, such as liquid crystal anchoring and guiding cell proliferation.

6.3 Reference

- [1] B. O'regan; M. Gr ätzl, *Nature* **1991**, 353, 737-740.
- [2] W.-M. Jin; J.-H. Shin; C.-Y. Cho; J.-H. Kang; J. H. Park; J. H. Moon, *ACS Applied Materials & Interfaces* **2010**, 2, 2970-2973.
- [3] E. S. Kwak; W. Lee; N.-G. Park; J. Kim; H. Lee, *Advanced Functional Materials* **2009**, 19, 1093-1099.
- [4] K. C. Hribar; R. B. Metter; J. L. Ifkovits; T. Troxler; J. A. Burdick, *Small* **2009**, 5, 1830-1834.
- [5] D. Schneider; F. Liaqat; E. H. El Boudouti; Y. El Hassouani; B. Djafari-Rouhani;

W. Tremel; H. J. Butt; G. Fytas, *Nano Lett.* **2012**, *12*, 3101-3108.